TECHNISCHE UNIVERSITÄT DRESDEN

Faculty of Environmental Sciences

Testing and improving the spatial and temporal resolution of satellite, radar and station data for hydrological applications

Untersuchung und Verbesserung der räumlichen und zeitlichen Auflösung von Satelliten-, Radar- und Bodenstationsdaten für hydrologische Anwendungen

Cumulative Dissertation to achieve the academic degree of
Doctor rerum naturalium (Dr. rer. nat.)

submitted by
Dipl.-Geogr. Christina Görner
born on 25 July 1978 in Stollberg/Erzgebirge, Germany

Referees

Prof. Dr. Christian Bernhofer
TU Dresden, Institute of Hydrology und Meteorology

Prof. Dr. Niels Schütze
TU Dresden, Institute of Hydrology und Meteorology

Dr.-Ing. habil. Uwe Müller
Saxon State Office for Environment, Agriculture and Geology (LfULG)

Submitted: Dresden, 20 August 2020
Defended: Dresden, 18 May 2021

Übereinstimmungserklärung

Die Übereinstimmung dieses Exemplars mit dem Original der Dissertation zum Thema „Testing and improving the spatial and temporal resolution of satellite, radar and station data for hydrological applications" wird hiermit bestätigt.

Dresden, den 20.07.2021 Christina Görner

Contents

List of publications

Peer-reviewed publications (Appendix A, B and C)

Görner C, Jatho N, Bernhofer C (2011) Applicability of satellite-based rainfall algorithms to estimate flood related rainfall events in the mid-latitudes. Part I: spatial integration. *J. Flood Risk Manage*, 4(3), 176-188.

Görner C, Kronenberg R, Bernhofer C (2012) Applicability of satellite-based rainfall algorithms to estimate flood related rainfall events in the mid-latitudes. Part II: temporal integration. *J. Flood Risk Manage*, 5(2), 175-186.

Görner C, Franke J, Kronenberg R, Hellmuth O, Bernhofer C (2019) Multivariate non-parametric Euclidean distance model for hourly disaggregation of daily climate data. *Theor Appl Climatol* TAAC-D-17-00762R1 (in revision)

Additional publications (Appendix D and E)

Görner C, Franke J, Hellmuth O, Bernhofer C (2009a) Climate changes in extreme precipitation events in the Elbe catchment of Saxony. In: Samuels et al. (eds.), Flood Risk Management: Research and Practice. Taylor & Francis Group, London, pp 1737-1743.

Görner C, Jatho N, Borga M, Bernhofer C (2009b) Satellite observation of storm rainfall for flash-flood forecasting in small and medium-size basins. In: Samuels et al. (eds.), Flood Risk Management: Research and Practice. Taylor & Francis Group, London, pp 1263-1271.

Abstract

This doctoral thesis is based on three publications (two peer-reviewed, one submitted). Its objective was to test existing methods and to develop innovative methods for generating highly resolved climate data with focus on the spatio-temporal distribution of precipitation as both, the spatial and temporal resolution as well as the length of such data sets are limited. For this purpose, satellite and radar-based remote sensing data, ground-based station data, and modelling methods were applied and combined. The Free State of Saxony (Germany) served as an investigation area as its mountainous regions are prone to heavy precipitation events and related (flash) floods like e.g., in 2002, in 2010, and in 2013.

Two approaches were developed to generate hourly data when there are no station data available or only daily data. The first approach applies four different algorithms to estimate area-wide rain rates by using the satellite data of *Meteosat Second Generation* (*MSG-1*) and compares them to the gauge adjusted radar data product *RADOLAN RW*. The analyses of five spatial und six temporal integration steps by means of four fit scores and statistical relations show a stepwise improvement. That means, the integration leads to increasing *probability of detection* (*POD*) and *critical success index* (*CSI*), decreasing *false alarm ratio* (*FAR*) and *Bias*, and improved statistical relations especially for heavy rain rates. The best results are achieved for the lowest resolution of 120 km × 120 km and 24 h. However, this resolution is too low for applications in (flash) flood risk management for small and medium sized catchments. Such satellite-based estimated rain rates may serve as a data source for unobserved regions or as an indicator for large catchments or longer periods.

A second approach comprises the newly developed *Euclidean distance model* (*EDM*) that generates hourly climate data by means of a temporal disaggregation procedure. The delivered data are point data for the climate variables temperature, precipitation, sunshine duration, relative humidity, and wind speed. They show high correlations and conserve (i) the statistics in comparison to the observed hourly data and (ii) also the consistency over all disaggregated climate elements. The results reveal that the *EDM* performs best for climate elements with a continuous diurnal cycle like temperature, for the winter half-year, and when the basic climate stations are characterised by similar climate conditions. The *EDM* proves to be a very robust, flexible and fast working model.

Hence, the work presented here succeeded in developing two innovative locally-independent approaches that are applicable to the climate data of any region or station without complex model parametrisation. Simultaneously, the method can be applied to future daily climate data allowing the generation of hourly data that are needed for climate impact models.

Zusammenfassung

Diese Dissertation basiert auf drei Publikationen (zwei begutachtet, eine eingereicht). Ziel war es, existierende Methoden zur Generierung hochaufgelöster Klimadaten zu untersuchen und innovative Methoden zu entwickeln mit dem Fokus auf der raumzeitlichen Niederschlagsverteilung, da sowohl die räumliche und zeitliche Auflösung als auch die Länge solcher Datenreihen begrenzt sind. Hierfür wurden satelliten- und radarbasierte Fernerkundungsdaten, Bodenstationsdaten sowie Modellierungsverfahren angewendet und kombiniert. Als Untersuchungsgebiet wurde der Freistaat Sachsen (Deutschland) gewählt, da dessen Gebirgsregionen starkregen- und damit hochwassergefährdet sind, wie bei den Hochwasserereignissen von 2002, 2010 und 2013 sichtbar wurde.

Es wurden zwei Ansätze entwickelt, die die Generierung von Stundendaten ermöglichen, wenn keine Daten oder nur Tagesdaten vorhanden sind. Der erste Ansatz verwendet vier verschiedene Algorithmen zum Abschätzen flächendeckender Niederschlagsintensitäten unter Verwendung der Daten des Satelliten *Meteosat Second Generation* (*MSG-1*) und vergleicht diese mit den an Bodenstationsdaten angeeichten Radardaten des *RADOLAN RW* Produktes. Die Analysen von fünf räumlichen und sechs zeitlichen Integrationsstufen mit Hilfe von vier Fit Scores und statistischer Kennwerte zeigen eine schrittweise Verbesserung der Ergebnisse. Das heißt, dass durch Integration steigende Werte der *probability of detection* (*POD*) und des *critical success index* (*CSI*), sinkende Werte der *false alarm ratio* (*FAR*) und des *Bias* sowie verbesserte statistische Kennwerte erreicht werden. Dies gilt insbesondere für Starkniederschlagsintensitäten. Die besten Ergebnisse werden bei der niedrigsten Auflösung von 120 km × 120 km und 24 h erreicht. Jedoch ist diese Auflösung für Anwendungen des Hochwasserrisikomanagements kleiner und mittlerer Einzugsgebiete zu gering. Solche satellitenbasierten Niederschlagsintensitäten können als Datenquelle für unbeobachtete Regionen oder als Indikator für große Einzugsgebiete oder längere Zeitintervalle dienen.

Ein zweiter Ansatz beinhaltet das neu entwickelte *Euclidean distance model* (*EDM*), das mittels zeitlicher Disaggregierung stündliche Klimadaten generiert. Die erzeugten Daten sind punktbezogene Daten der Klimavariablen Temperatur, Niederschlag, Sonnenscheindauer, relative Feuchte und Windgeschwindigkeit. Sie weisen hohe Korrelationen auf und sie wahren (i) die statistischen Kenngrößen im Vergleich mit den beobachteten Stundendaten und (ii) die Konsistenz über alle Klimaelemente hinweg.

Die Ergebnisse zeigen, dass das *EDM* für Klimaelemente mit einem kontinuierlichen Tagesgang, wie z.B. die Temperatur, für das Winterhalbjahr und bei der Verwendung von

Basisstationen mit ähnlicher klimatischer Charakteristik die besten Ergebnisse liefert. Das *EDM* erweist sich als ein sehr robustes, flexibles und schnell arbeitendes Modell.

Somit ist es mit der hier vorliegenden Arbeit gelungen, zwei innovative Ansätze zu entwickeln, die ohne komplexe Modellparametrisierung auf Daten einer jeden Klimaregion oder Klimastation angewendet werden können.

List of Abbreviations

AMSU-B	Advanced Microwave Sounding Unit - B
CLM	Climate Local Model
COSMO-DE	Consortium for Small Scale Modelling - Deutschland
CSI	critical success index
DWD	Deutscher Wetterdienst, German Weather Service
EC	European Commission
ECST	Enhanced Convective Stratiform Technique
ED	Euclidean distance
EDM	Euclidean distance model
ESA	European Space Agency
EUMETSAT	European Organisation for the Exploitation of Meteorological Satellites
FAR	false alarm ratio
FCI	Flexible Combined Imager
GMS	Geostationary Meteorological Satellite
GMSRA	GOES Multispectral Satellite Radiation Application
GOES	Geostationary Operational Environmental Satellite
GPM	Global Precipitation Measurement
GPCP	Global Precipitation Climatology Project
IPCC	Intergovernmental Panel on Climate Change
IRS	Infrared Sounder
JAXA	Japan Aerospace Exploration Agency
KM	Kurino Method
LI	Lightning Imager
Meteosat	Meteorological satellite
MSG	Meteosat Second Generation
MTG	Meteosat Third Generation
MTG-I	Meteosat Third Generation – Imager
MTG-S	Meteosat Third Generation – Sounder
NASA	National Aeronautics and Space Administration
NASIM	Niederschlag-Abfluss-Simulation
N	North
NE	North-East

OWP	Objective Weather Pattern
POD	probability of detection
RADOLAN RW	Radar-Online-Aneichung
S	South
SEVIRI	Spinning Enhanced Visible and InfraRed Imager
SSM/I	Special Sensor Microwave Imager
SMUL	Sächsisches Staatsministerium für Umwelt und Landwirtschaft
SW	South-West
TMI	TRMM Microwave Imager
TRMM	Tropical Rainfall Measuring Mission
TU Dresden	Technische Universität Dresden
UVN	Ultraviolet Visible Near-infrared
WaSiM-ETH	Water Flow and Balance Simulation Model - Eidgenössische Technische Hochschule
WETTREG	Wetterlagenbasiertes Regionalmodell

1 Introduction

Following the IPCC synthesis report (2014), the observed climate change led to widespread consequences for human and natural systems across all continents and oceans in recent decades. The hydrological systems are changing due to changing precipitation and temperature conditions in many regions with impact on the quantity and quality of water resources. Since about 1950, changes in many extreme weather and climate events are observed, e.g. a decrease in cold temperature extremes, an increase in warm temperature extremes, and an increase in the frequency of heavy precipitation events. And the intensity and frequency of heavy precipitation events and hot spells will very probably continue to increase. The increasing trend of extreme precipitation and related extreme runoff cause higher flood risks in medium sized water catchments.

For urban areas, increasing risks are projected for the people, property values, economies and ecosystems. Such risks are e.g., heat stress, storms, extreme precipitation, floods, droughts, and water shortage. For rural regions, significant consequences are expected for the water availability and water supply (IPCC 2014). These changes affect almost all areas of human life, like freshwater resources, hydrometeorological hazards, soil erosion, changing flora and fauna, and human health.

As precipitation is a key element of the water cycle at all scales from global to small-scale catchments, its spatial and temporal distribution is of high interest and relevance. Important aspects of the intensity and spatial distribution of precipitation are the availability of water and the risks of floods especially due to the increasing influence of climate change. Flooding is one of the most widely distributed natural hazards threatening millions of people and causing damages amounting to billions worldwide. The data of *Munich Re* show an increasing frequency and financial impact of flooding since the last decades (Munich Re 2018). For example, between 2013 and 2018 there have been severe flood events due to heavy precipitation in Germany (East and South Germany, June 2013; South Bavaria, June 2016), Italy (North Italy, Piemont and Liguria, November 2017), Argentina and Bolivia (North-west Argentina, South Bolivia, February 2018), Nigeria (Soth-East Nigeria, August 2017) or China (North China, Hebei province, July 2016).

To forecast and manage such events, to protect the people and their property and to prevent damages and financial losses, data of heavy precipitation occurrence, location, amount, and intensity are required in high spatial and temporal resolution. Moreover, the impact of climate change further increases the requirements. It leads to higher flood risks due to increasing frequencies of heavy precipitation events, higher precipitation intensities and decreased return periods of heavy precipitation events (Görner et al. 2009a, IPCC 2014, SMUL 2015). These changing climate conditions and the related consequences lead to a higher need of improved methods and data basis to predict, observe and mitigate risks and

possible related damages. Hence, precipitation and its distribution play an important role in a large number of models like water balance models (e.g., WaSim-ETH), rainfall-runoff models (e.g., NASIM), flood simulation models (e.g., MIKE FLOOD), and soil erosion models (e.g., EROSION 3D). Future precipitation data are simulated by regional models for weather prediction (e.g., COSMO-DE) and regional climate models (e.g., WETTREG2010, WEREX-V or CLM). All these models need precipitation data in sufficient extent and spatio-temporal resolution, either as a driver (like WaSim-ETH) or for validation (like COSMO-DE). There are three different approaches to achieve these data, (i) they can be measured by ground-based rain gauges that provide point measurements, (ii) they can be estimated by radar and satellite-based remote sensing methods that provide area-wide data, and (iii) they can be modelled by methods that generate, complete or extend time series of precipitation data, e.g. by spatial or temporal downscaling and disaggregation.

2 Objective and background

The Free State of Saxony (Germany) has already been affected by climate change during the last decades and it will be affected even more in the future (SMUL 2008, SMUL 2015). The recorded regional climate data show a high natural climate variability since the 1960s. This variability is increasingly overlaid by a mean trend of increasing temperature. Since about 40 years, each decade has been warmer than the decade before. Between 1961 and 2010 the annual mean temperature has increased by about 1 °C comparing the first and last decade. Following recent climate projections for Saxony, this temperature trend will continue (SMUL 2015). Concerning precipitation, the climate change leads to changes in the spatial and temporal distribution, higher sums during the summer months and deficits during the winter months with consequences for the regional climatic water balances (Kronenberg et al. 2015, SMUL 2015, Görner et al. 2009a).

The climate change leads to the risk of increasing and coincide extremes like dry spells and heavy precipitation events with higher intensities, frequencies and sums as well as reduced return periods especially for the summer months. This causes a higher risk of local (flash) floods in small and medium catchments, a higher risk of erosion and high challenges for the water management, e.g. the management of water reservoirs to ensure the (drinking) water supply as well as the water retention in case of floods. This conflict intensifies by the different duration of these opposite events. While heavy precipitation events and floods occur during hours and a few days, dry spells range from weeks to months or even span years.

Besides the impact of climate change, Saxony is prone to heavy precipitation events because of its orographic and climate conditions. Hence, there is a high (flash) flood risk (SMUL 2005, Görner et al. 2011). There have been severe flash floods caused by extreme precipitation events, e.g. in August 2002, in August and September 2010 and in June 2013.

Therefore, flood forecasting, flood mitigation and flood risk management and the research on these are of high interest as e.g. described in Müller (2010).

These topics were in focus of the project "FLOODsite - Integrated Flood Risk Management and Methodologies". FLOODsite was an "Integrated Project" in the Sixth Framework Programme of the European Commission between 2004 and 2009. The Institute of Hydrology and Meteorology of Technische Universität (TU) Dresden was one of the project partners in Task 15 "Radar and satellite observation of storm rainfall for flash-flood forecasting in small and medium-size basins" and Task 21 "Pilot Study River Elbe Basin". The results summarised in Section 3 and presented in Görner et al. (2011, 2012 & 2019 or Appendices A, B and C) are based on the research within this project including recent research in Saxony.

The aim of Task 15 was the development of a radar and satellite Structured Algorithm System (SAS) for quantitative precipitation estimation (QPE) at the space and timescales of interest for flash-flood analysis and prediction. Thereby, the part of the TU Dresden was to develop a satellite-based SAS for detecting extreme storm rainfall by using highly resolved geostationary satellite data (Meteosat-6, Meteosat-8) and applying several rainfall estimation techniques (Görner et al. 2011, 2012 & 2009b). These techniques were tested for different flash flood prone regions in the mid-latitudes regarding their potential to derive areal and highly resolved rain intensity data.

The aim of the research within Task 21 was to improve the understanding of complex flood risk management in a large transnational river basin and to develop and provide flood risk management tools (www.floodsite.net). The meteorological investigations of TU Dresden within this task focused on heavy rainfall events and pre-event moisture as two important drivers of flood risk under changing climate conditions. This encompassed the analysis of regionalised daily climate scenario data concerning the temperature increase as well as reducing return periods and increasing frequencies of heavy precipitation within Saxony (Görner et al. 2009a). Since the data of the climate projections were only available in a daily temporal resolution, while the rainfall runoff model used hourly data as input, there was a need to develop a tool for disaggregating daily climate data into hourly data (Görner et al. 2019). The disaggregation of further climate elements, e.g. temperature, allows the estimation of possible flood risks considering the pre-event moisture.

Both tasks and the challenge of climate change show that required data are not available in sufficient length or resolution. Therefore, there is a high need of methods for estimating or generating highly resolved data, especially rainfall data. Hence, the objective of this work is to develop innovative methods for the acquisition of data of the spatio-temporal distribution of precipitation and other climate elements by using and combining ground-based observations and projections, ground-based remote sensing methods (radar), satellite-based remote sensing methods, and modelling methods with the aim of closing spatial and temporal

data gaps. Further, it was the aim to develop new methods that can be applied to the data of climate stations of any climate region without complex and time-consuming parameterisation of the procedures or model.

3 State of the art of satellite-based precipitation estimation

The current active Meteosat satellite that provides data for Europe is the fourth satellite of the Meteosat Second Generation series (MSG-4). MSG-4 carries the same Spinning Enhanced Visible and InfraRed Imager (SEVIRI) like MSG-1 (studies in Görner et al. 2011 & 2012). Since 2011 further developments and improvements has been achieved concerning the satellite-based precipitation estimation (Qu et al. 2013, Xu et al. 2014, Li et al. 2016, Massari et al. 2017, Hong et al. 2018). Improvements are achieved mainly by combining the data of different satellites, e.g. geostationary and polar orbiting satellites, and different sensor types like Visible/Infrared Imager, passive/active microwave sensors or radar. Table 1 contains an overview of the existing sensor types, examples of satellites carrying such sensors, the used basics of precipitation retrieval methods and their pros and cons. With these various data, integrated precipitation products are generated, e.g. by means of neural networks or machine learning algorithms (Kühnlein et al. 2014, Meyer et al. 2016). Such integrated products are exemplarily generated by the Tropical Rainfall Measuring Mission (TRMM) (Huffman et al. 2010, Liu et al. 2012), the Global Precipitation Measurement (GPM) mission (Hou et al. 2014, Skofronick-Jackson et al. 2017), and the global monitoring programme Copernicus (Aschbacher 2017).

Table 1: Summary of remote sensing techniques for precipitation estimation (after Xu et al. 2014 and Ferraro and Smith 2013)

Sensors (platform)	**Orbit type**	**Retrieval methods**	**Pros**	**Cons**
visible / infrared (e.g. Meteosat, GOES, GMS)	geo-stationary; polar orbiting	rain rate is estimated based upon the cloud top temperatures	good spatial and temporal resolution	weak physical connection to precipitation; indirect rain rate
spaceborne passive microwave sensors (e.g. SSM/I, TMI, AMSU-B)	polar orbiting	Bayesian approach to match the observed brightness temperatures with those from simulated hydrometeor profiles (Imagers); a combination of brightness temperatures at different frequencies (Sounders)	better physical connection to precipitation	coarse spatial and temporal resolution; indirect rain rate
spaceborne active microwave sensors / radar (e.g. Precipitation Radar on TRMM)	polar orbiting	Radar reflectivity – rain rate and specific attenuation – radar reflectivity relations	direct measurement of the 3-D structure of precipitation	The variability of the drop size distributions strongly affects precipitation estimation.

TRMM was a cooperative satellite mission of the National Space Development Agency (NASDA) of Japan and the National Aeronautics and Space Administration (NASA) of the USA. Between 1997 and 2015, it provided rainfall measurements using a combination of high resolution radar, passive microwave radiometer and visible-infrared radiometer measurements from a polar orbiting satellite. The data covered only the tropic and subtropics between 40°S and 40°N with a spatial and temporal resolution of up to 0.25° x 0.25° and 3 h (Huffman et al. 2010, Liu et al. 2012).

Since 2014, the GPM mission takes care of TRMM. GPM was initiated by NASA and the Japan Aerospace Exploration Agency (JAXA) and is an international network of satellites that provide global observations of rain and snow at a comparatively high temporal (0.5 – 3.0 h) and spatial (5 – 15 km) resolution. GPM enhances precipitation measurements by using a combination of active and passive remote sensing techniques. The measurements are used to calibrate, unify and improve global precipitation measurements by including microwave sensors (Skofronick-Jackson et al. 2017).

Copernicus is the Earth Observation Programme of the European Commission (EC) and the European Space Agency (ESA). It consists of a complex set of satellites and sensors, called Sentinels, collecting data from various sources, including Earth observation satellites and in situ sensors (e.g., ground stations, airborne/seaborne instruments). Among others, it also provides data for monitoring the atmosphere and the climate change. For example, Sentinel-1 carries a C-band radar for high resolution weather monitoring, Sentinel-3 provides infrared radiometric data for high-precision temperature measurements, and Sentinel-4 and -5 will monitor the atmosphere and its composition from geostationary and polar orbits (Aschbacher 2017). Sentinel-4 will be on board of Meteosat Third Generation (MTG) as the Flexible Combined Imager (FCI) (see Section 6).

But despite all these developments and improvements, the basic difficulties and problems of satellite data still persist, either a high spatial or a high temporal resolution. Also radar based precipitation estimation still suffers from uncertainties like attenuation, beam blockage, ground clutter, or variability of the Z-R relation (Villarini and Krajewski 2009; Kronenberg and Bernhofer 2015). And concerning rainfall gauges, the measuring network density is often too low and varies strongly over regions and countries. Furthermore, the precipitation characteristics in the mid-latitudes are very complex due to the co-occurrence of convective and stratiform precipitation. All these basic problems are still unsolved until today and will not be solved in the near future. Hence, precipitation is and will be prone to a large uncertainty, and the recognition of precipitation patterns continues to suffer from an insufficient number of sampling points at the ground.

4 Material and methods

4.1 Study region

The Free State of Saxony (Germany) was used as a case study region for the methods developed and applied within the scope of this work. Saxony is located in the westerly wind zone of the mid-latitudes and it covers an area of about 18 400 km² that encompass low altitude regions as well as low-range mountains (Ore Mountains). Saxony is prone to heavy precipitation events and related (flash) floods especially in the mountainous regions (Görner et al. 2011 & 2012) due to the climatic characteristics, the impact of climate change (SMUL 2005) and the SW-NE oriented Ore Mountains The changing climate leads also to changes in the water balance and related problems regarding water availability, distribution, storage and usage (Görner et al. 2019).

4.2 Data

For the investigations and results presented in Görner et al. (2011 & 2012), satellite, radar and radiosonde data were used. The first satellite of EUMETSAT's *Meteosat Second Generation* satellite series (*MSG-1*) delivered the satellite data. Since 2004, data with a temporal resolution of 15 min and a spatial resolution of 3.4 km × 5.9 km (channels 1-11) for the region of Saxony have been measured (Schmetz et al. 2002). The *RADOLAN RW* data are rain gauge adjusted radar data provided by the German Weather Service (*DWD*). These data have a temporal resolution of 1 h and a spatial resolution of 1 km × 1 km (Bartels 2004). The *DWD* also provided the 6-hourly radiosonde data. For this study, the values of the precipitable water and the mean relative humidity from the *DWD* observatory *Lindenberg* were used.

Data basis for Görner et al. (2019) were hourly and daily climate data of the six climate stations *Chemnitz*, *Dresden-Klotzsche*, *Fichtelberg*, *Görlitz*, *Leipzig/Halle* and *Plauen* of the *DWD*. The data cover the time between September 1995 and August 2014 and encompass the climate elements temperature, precipitation, sunshine duration, relative humidity, and wind speed. Further, the daily objective weather pattern (*OWP*) classification provided by the *DWD* was used. It consists of 40 classes encompassing all atmospheric circulation conditions relevant for Germany.

4.3 Methods

In Görner et al. (2011 & 2012), four satellite-based rainfall algorithms were applied to the highly resolved *MSG-1* satellite data of 9 days with high rainfall amounts between May and August 2006. The following algorithms were chosen:

- the Operational GOES Infrared Rainfall Estimation Technique [or: Auto-Estimator] (Vicente et al. 1998)

- the Enhanced Convective Stratiform Technique (ECST) (Reudenbach 2003)
- the GOES Multispectral Rainfall Algorithm (GMSRA) (Ba and Gruber 2001)
- the Kurino Method (KM) (Kurino 1997a, b)

The estimated satellite-based hourly rain intensities were compared to radar-based rain intensities that represented the reference values for these two studies. The radar and satellite data had to be reduced to a common temporal and spatial resolution of 1 h and 3 km × 6 km to make them comparable. After this adjustment, spatial integration (Görner et al. 2011) and temporal integration (Görner et al. 2012) were possible to examine their effects on the quality of the satellite rain intensities (amounts and locations), the related loss of spatial and temporal information, and possible applications for flood risk management. Five spatial integration steps ranging between 18 km² and 57 600 km² and six temporal integration steps ranging between 1 h and 24 h were used. The performance of the satellite-based rainfall algorithms was examined by a range of statistics of the grid-wise absolute differences and by using measures of goodness of fit to assess the spatial agreement of satellite- and radar-based rain intensities. The four fit scores *probability of detection* (*POD*), *false alarm ratio* (*FAR*), *critical success index* (CSI), and *Bias* (Wilks 2006) were applied.

For the generation of hourly climate data by disaggregating observed daily climate data presented in Görner et al. (2019), a new multivariate non-parametric model, the *Euclidean Distance Model* (*EDM*) was developed. This model uses the *Euclidean Distance* (*ED*) as a measure of the similarity of two individual daily climate data sets with the aim to find the most similar analogous reference day. The model generates hourly data of temperature, precipitation, sunshine duration, relative humidity and wind speed. As an example, the daily climate data of the stations *Dresden* and *Fichtelberg* were disaggregated for the years 1995-2014. The generated hourly climate data were compared to the observed hourly data by statistical analyses and by calculating the mean diurnal cycles based on hourly data and the mean annual cycles based on monthly data.

5 Major findings

The methods presented in Görner et al. (2011, 2012 & 2019) deliver hourly climate data by using two different innovative and location-independent approaches. Both approaches represent a possibility to generate hourly data when there are no station data or data with only daily temporal resolution. The estimation of rain intensities by applying satellite-based rainfall algorithms to highly resolved satellite data (Görner et al. 2011 & 2012) deliver area-wide data. This is an advantage for the observation of areal rainfall sums of catchments and possible related flood risk. Thereby, we receive data also from regions, which are insufficiently observed or not observed at all by radar stations and/or rain gauges. The spatial and temporal integration leads to improved agreement of satellite-based and radar-based rain intensities with increasing *POD* and *CSI*, decreasing *FAR* and *Bias*, and improved statistical

relations especially concerning heavy, possible flood-triggering rainfall events. Therefore, the best results are achieved for the lowest resolution of 120 km × 120 km and 24 h. However, since the integration also causes a loss of spatial and temporal information, these resolutions are not suitable for assessing (flash) flood risks in mid-latitude regions. Higher resolutions would be suitable but the rainfall algorithms perform poorly in reproducing both the rainfall intensities and the spatial extend of the rain fields. The rainfall algorithms smooth the rain field as they tend to underestimate high rain intensities and overestimate low rain intensities. Hence, these satellite-based rainfall algorithms are currently not suitable for applications in flood risk management for small-scale catchments in mountainous regions in the mid-latitudes.

The problems and weakness associated with satellite-based rain intensities result from several sources of error and uncertainties concerning the measurement system, and the algorithms. Due to the scanning angle, the rotation of the satellite, and the projection, the geo-referencing of the satellite data is difficult. The relation between the cloud top temperature, reflectance, and the rainfall reaching the ground is too weak for correct rain intensities estimations. In addition, the algorithms have to be well adapted to the used satellite data as well as to the target region and its climate characteristics. The estimated rain rates were corrected concerning the moisture conditions of the environment and the growing or decaying of the raining clouds but further additional data like wind and orography should be included in the estimation as they have a high influence on the rainfall rate reaching the ground. But despite all these difficulties, satellite-based rain rates represent a good possibility for unobserved regions and may be used as an indicator when the catchment is large or the considered temporal resolution amounts to 12 h or more.

The generation of hourly climate data by disaggregating daily data (Görner et al. 2019) delivers point-related data. With such data, the estimation of areal rainfall sums of catchments and possible related flood risks is more difficult than with the area-wide remote sensing data but ground-based point data are more exact as they are measured and not estimated.

The newly developed *EDM* proved to be a very robust and flexible model that is applicable to any climate station and that works with several climate elements as well as with only one climate element. It delivers hourly climate data that show strong correlations to the observed data for all climate elements, maintaining their statistics, and the generated data set is consistent over the disaggregated climate elements. But the results fit better to climate elements with a continuous diurnal cycle. Hence, the best results are achieved for temperature and the worst for wind speed and sunshine duration. Further, the results fit better when the used basic climate stations have similar climate conditions and when the disaggregated element is involved in the calculation of the *ED*. The analyses of the winter and summer half-year showed, that the *EDM* delivers better results for the winter half-year

than for the summer half-year. This is caused by the fact that the summer month are characterised by more turbulence and unstable weather conditions. Concerning precipitation, the *EDM* tends to overestimate the quantiles of the hourly data, especially for heavy and extreme values, because the pool of such precipitation events from which *EDM* can select the most similar day is smaller. This tendency might be an advantage in the field of hydro engineering.

To improve the selection of the most similar basic day and the results accordingly, the *OWP* were included but it was shown that the *OWP* lead to only small improvements for all climate elements and are hence not necessary to generate accurate hourly data.

Due to the functionality of the *EDM*, the results conserve the daily means or sums of the disaggregated climate elements. Under the precondition that the used basic climate stations have been similar, also the mean diurnal and annual cycle are reproduced correctly. Since the *EDM* is based on a resampling approach, the generated hourly data are more or less a copy of the past. However, the applied offset or boost factors for new 'records' in the target time-series, allows the generation of data which have not yet been observed. Therefore, the model is capable of considering future climate trends.

6 Conclusion and outlook

The acquisition of highly resolved data of the spatio-temporal distribution of precipitation and other climate elements was realised by developing innovative local-independent methods that combine ground-based observation data, radar-based data, and satellite-based data. These methods are applicable for any climate region and climate station, respectively. Two different approaches were developed.

First, several algorithms for estimating rain rates were applied to the highly resolved satellite data of *MSG-1*. Nine days with high rainfall amounts within Saxony (Germany) were selected as case study. The algorithms deliver area-wide precipitation data with that were compared to gauge adjusted radar data for five spatial and six temporal integration steps to investigate the applicability of satellite-based rain rates for flood risk management. Although each integration step leads to improved results, the estimated rain rates and rain fields are currently not suitable for applications in flood risk management for small-scale (flash) flood-prone catchments in the mid-latitudes. This is due to uncertainties and sources of error related to the satellite measuring system, the satellite data, and the functionality of the algorithms. However, the estimated rainfall data may be used as an indicator for rainfall totals over longer periods or for large catchments or when gauge and radar data are missing. To improve the estimated data and their applicability, the algorithms have to be customised to the satellite data and the target region, additional data like wind and orography should be included, and combining data from different systems, such as satellite, radar, and microwave sensors may be helpful. From the end of 2021 on, the first satellite of Meteosat Third

Generating (MTG) will deliver data routinely. As MTG will carry more sensors, these will be distributed on two platforms, an Imaging Satellite (MTG-I) and a Sounding Satellite (MTG-S). The MTG-I satellite carries the Lightning Imager (LI) and the Flexible Combined Imager (FCI) that provides 16 spectral channels of image data, with a repeat cycle of 10 min, and a European regional rapid scan with a repeat cycle of 2.5 min. The MTG-S satellite carries the Infrared Sounder (IRS) and the high resolution Ultraviolet Visible Near-infrared (UVN) spectrometer. The IRS provides hyperspectral sounding data every 30 min over Europe (EUMETSAT 2020). Hence, MTG will deliver data in higher quality and resolution and it will deliver sounding data from a geostationary orbit for the first time. The applicability of the satellite-based rainfall estimation algorithms as examined in Görner et al. (2011 & 2012) has to be investigated by using and adopting them to the new data of the FCI and by expanding the algorithms to include the data provided by the IRS sensor.

A second approach for the acquisition of hourly climate data was developed by means of a temporal disaggregation model, the *EDM*. It delivers point data sets for several climate elements with high correlations and conserved statistics compared to the observed data as well as consistency over the disaggregated climate elements. The *EDM* is a very robust, flexible and fast working model that can be applied to any climate station and any climate data set. However, there are also two restriction: (i) the basic climate data should have similar climate, and (ii) the model requires a sufficient database of observed hourly data. But although the generated data are always a copy of the past due to the resampling approach of the *EDM*, these data are very useful to fill data gaps and to apply models like water balance models, rainfall-runoff models, or ecological models. Further, the applied offsets allow the generation of data, which have not yet been observed. Therefore, the model is capable of taking future climate trends into account and can disaggregate daily data of climate projections. This may allow impact modelling and analyses of future climate extremes.

The two locally independent methods presented here are applicable for the acquisition of highly resolved data of the spatio-temporal distribution of precipitation and other climate elements. Finally, and importantly, both methods have the technical advantages of an efficient computing performance and no need for calibration. So, two helpful tools for the estimation of highly resolved meteorological data (especially precipitation data) are available and can be used for various climatological and hydrological purposes.

Further work is necessary to combine both methods sufficiently. As the *EDM* is suitable to disaggregate any daily climate data, it is also suitable in principle to disaggregate satellite precipitation data, e.g. the Global Precipitation Climatology Project (GPCP) Combined Precipitation Dataset (Huffman et al. 1997) or the GPM d. It has to be examined which data basis is applicable for the disaggregation of pixelwise data, either pixelwise satellite- or radar-based data or rain gauge data. The future of measuring, estimating and generating of temporal and spatial highly resolved precipitation data lies in the combination of different

sensors and methods, while ground truthing remains a crucial task for any remote sensing precipitation product. And as often in remote sensing, the high costs of the satellite platform and of the launching vehicle influence the payload. Which in turn does not support a network of active radar satellites covering the globe sufficiently well for an independent highly resolved dataset from space.

References

Aschbacher J (2017) ESA's Earth Observation Strategy and Copernicus. In: Onoda M, Young O R (eds.), Satellite Earth Observations and Their Impact on Society and Policy. Springer, Singapore, 221 pp.

Ba M B, Gruber A (2001) GOES Multispectral Rainfall Algorithm (GMSRA). *J Appl Meteor*, 40, 1500-1514.

Bartels H (2004) Projekt RADOLAN. Routineverfahren zur Online-Aneichung der Radarniederschlagsdaten mit Hilfe von automatischen Bodenniederschlagsstationen (Ombrometer). Projekt-Abschlußbericht, Available at www.dwd.de/RADOLAN (accessed 4 April 2018).

EUMETSAT (2020) Meteosat Third Generation. Available at: https://www.eumetsat.int/website/home/Satellites/FutureSatellites/MeteosatThirdGeneration/index.html (accessed 23 February 2020).

Ferraro R, Smith T (2013) Global Precipitation Monitoring. In: Qu J et al. (eds.), Satellite-based Applications on Climate Change. Springer, Dordrecht, pp 81-93.

Görner C, Jatho N, Bernhofer C (2011) Applicability of satellite-based rainfall algorithms to estimate flood related rainfall events in the mid-latitudes. Part I: spatial integration. *J. Flood Risk Manage*, 4(3), 176-188.

Görner C, Kronenberg R, Bernhofer C (2012) Applicability of satellite-based rainfall algorithms to estimate flood related rainfall events in the mid-latitudes. Part II: temporal integration. *J. Flood Risk Manage*, 5(2), 175-186.

Görner C, Franke J, Kronenberg R, Hellmuth O, Bernhofer C (2018) Multivariate non-parametric Euclidean distance model for hourly disaggregation of daily climate data. *Theor Appl Climatol* TAAC-D-17-00762R1 (in revision)

Görner C, Franke J, Hellmuth O, Bernhofer C (2009a) Climate changes in extreme precipitation events in the Elbe catchment of Saxony. In: Samuels P et al. (eds.), Flood Risk Management: Research and Practice. Taylor & Francis Group, London, pp 1737-1743.

Görner C, Jatho N, Borga M, Bernhofer C (2009b) Satellite observation of storm rainfall for flash-flood forecasting in small and medium-size basins. In: Samuels P et al. (eds.), Flood Risk Management: Research and Practice. Taylor & Francis Group, London, pp 1263-1271.

Hong Y, Tang G, Ma Y, Huang Q, Han Z, Zeng Z, Yang Y, Wang C, Guo X (2018) Remote Sensing Precipitation: Sensors, Retrievals, Validations, and Applications. In: Li X, Vereecken H (eds.), Observation and Measurement of Ecohydrological Processes. Springer-Verlag, Berlin, Heidelberg, 2019, 509 pp.

Hou A Y, Kakar R K, Neeck S, Azarbarzin A A, Kummerow C D, Kojima M, Oki R, Nakamura K, Iguchi T (2014) The Global Precipitation Measuring Mission. *Bull Amer Meteor So.,* 95(5), 701-722.

Huffman G J, Adler R F, Arkin P, Chang A, Ferraro R, Gruber A, Janowiak J, McNab A, Rudolf B, Schneider U (1997) The Global Precipitation Climatology Project (GPCP) Combined Precipitation Dataset. *B. Am. Meteorol. Soc.*, 78(1), 5-20.

Huffman G J, Adler R F, Bolvin D T, Nelkin E J (2010) The TRMM Multi-Satellite Precipitation Analysis (TMPA). In: Gebremichael M., Hossain F. (eds) Satellite Rainfall Applications for Surface Hydrology. Springer, Dordrecht, 327 pp.

IPCC (2014) Climate Change 2014: Synthesis Report. Contribution of Working Groups I, II and III to the Fifth Assessment Report of the Intergovernmental Panel on Climate Change

[Core Writing Team, R.K. Pachauri and L.A. Meyer (eds.)]. IPCC, Geneva, Switzerland, 151 pp.

Kronenberg R, Franke J, Bernhofer C, Körner P (2015) Detection of potential areas of changing climatic conditions at a regional scale until 2100 for Saxony, Germany. *Meteorol. Hydrol. Water Manage*., 3(2), 17-26.

Kronenberg R, Bernhofer C (2015) A method to adapt radar-derived precipitation fields for climatological applications. *Meteorol Appl*, 22(3), 636–649.

Kurino T (1997a) A rainfall estimation with the GMS-5 infrared split-window and water vapour measurements. Meteorological Satellite Centre, Technical Note, No. 33, 91-101.

Kurino T (1997b) A satellite infrared technique for estimating „deep/shallow“ convective and stratiform precipitation. *Adv Space Res*, 19, 511-514.

Kühnlein M, Appelhans T, Thies B, Nauss T (2014) Improving the accuracy of rainfall rates from optical satellite sensors with machine learning - A random forests-based approach applied to MSG SEVIRI. *Remote Sens. Environ.,* 141, 129–143.

Li Y, Grimaldi S, Walker J P, Pauwels R N V (2016) Application of Remote Sensing Data to Constrain Operational Rainfall-Driven Flood Forecasting: A Review. *Remote Sens*, 8 (6), 456.

Liu Z, Ostrenga D, Teng W, Kempler S (2012) Tropical Rainfall Measuring Mission (TRMM) Precipitation Data and Services for Research and Applications. *Bull Amer Meteor Soc*, 93, 1317-1325.

Massari C, Crow W, Brocca L (2017) An assessment of the performance of global rainfall estimates without ground-based observations. *Hydrol Earth Syst Sci*, 21, 4347–4361.

Meyer H, Kühnlein M, Appelhans T, Nauss T (2016) Comparison of four machine learning algorithms for their applicability in satellite-based optical rainfall retrievals. *Atmos Res*, 169, Part B, 424-433.

Müller U (2019) Hochwasserrisikomanagement - Theorie und Praxis. Vieweg + Teubner Verlag, Springer Fachmedien Wiesbaden GmbH, ISBN 978-3-8348-1247-6, 440 pp.

Munich Re (ed) (2018) TOPICS Geo Naturkatastrophen 2017 – Analysen, Bewertungen, Positionen. Münchener Rückversicherungs-Gesellschaft, 68 pp.

Qu J, Powell A, Sivakumar M.V.K. (eds.) (2013) Satellite-based Applications on Climate Change. Springer, Dordrecht, 384 pp.

Reudenbach C (2003) Konvektive Sommerniederschläge in Mitteleuropa. Bonner Geographische Abhandlungen, Heft 109, Asgard-Verlag Sankt Augustin.

Schmetz J, Pili P, Tjemkes S A, Just D, Kerkmann J, Rota S, Ratier A (2002) An introduction to Meteosat Second Generation (MSG). *Bull Amer Meteor Soc*, 83 (7), 977-992.

Skofronick-Jackson G, Petersen W A, Berg W, Kidd C, Stocker E F, Kirchbaum D B, Kakar R, Braun S A, Huffman G J, Iguchi T, Kirstetter P E, Kummerow C, Meneghini R, Oki R, Olson W S, Takayabu Y N, Furukawa K, Wilheit T (2017) The Global Precipitation Measurement (GPM) Mission for Science and Society. *Bull Amer Meteor So.,* 98(8), 1679-1695.

SMUL (ed) (2005) Klimawandel in Sachsen – Sachstand und Ausblick 2005. Sächsisches Staatsministerium für Umwelt und Landwirtschaft, 109 pp.

SMUL (ed) (2008) Sachsen im Klimawandel – Eine Analyse. Sächsisches Staatsministerium für Umwelt und Landwirtschaft, 211 pp.

SMUL (ed) (2015) Klimawandel in Sachsen – wir passen uns an! Sächsisches Staatsministerium für Umwelt und Landwirtschaft, 138 pp.

Thies B (2008) A novel day/night technique for area-wide precipitation retrieval over Central Europe using MSG SEVIRI data. Dissertation, Fachbereich Geographie,

Philipps-Universität Marburg, 176pp. Available at http://archiv.ub.uni-marburg.de/diss/z2008/0906/ (accessed 4 April 2018).

Vicente G A, Scofield R A, Menzel W P (1998) The operational GOES infrared estimation technique. *Bull Amer Meteor Soc*, 79(9), 1883-1998.

Villarini G, Krajewski W F (2009) Review of the Different Sources of Uncertainty in Single Polarization Radar-Based Estimates of Rainfall. *Surv Geophys,* 31, 107–129.

Wilks D S (2006) Statistical Methods in the Atmospheric Sciences. 2nd edn, International Geophysics Series 91. Amsterdam: Academic Press, Elsevier, 627 pp.

Xu X, Li J, Tolson B A (2014), Progress in integrating remote sensing data and hydrologic modeling, *Prog Phys Geog*, 38 (4), 464–498.

Appendix A

Peer-reviewed publication 1

Journal of
Flood Risk Management

Applicability of satellite-based rainfall algorithms for estimating flood-related rainfall events in the mid-latitudes. Part I: spatial integration

C. Görner, N. Jatho and C. Bernhofer

Institute of Hydrology and Meteorology, Technische Universität Dresden, Tharandt, Germany

Correspondence
Christina Görner, Institute of Hydrology and Meteorology, Technische Universität Dresden, Pienner Str. 23, Tharandt 01737, Germany
Tel: +49 351 463 31346
Fax: +49 352 033 831 302
Email: christina.goerner@tu-dresden.de

DOI:10.1111/j.1753-318X.2011.01102.x

Key words
Flash floods; flood risk; Meteosat Second Generation (MSG); satellite rainfall estimate; spatial integration.

Abstract

This paper presents a study of the applicability of four satellite-based rainfall algorithms using highly resolved data from the first Meteosat Second-Generation satellite to derive hourly rain intensities. Saxony serves as an example of the mid-latitude regions. The focus is on the suitability of these algorithms to detect and to monitor (flash) flood-related rain intensities. For this purpose, 9 days with high rainfall amounts between May and August 2006 were analysed by comparing the satellite rain intensities to gauge adjusted radar data. Five different spatial resolutions were used to examine the effects of spatial integration from small scale (18 km^2) to large scale (57 600 km^2) on (i) the quality of the satellite rain intensities (amounts and locations); (ii) the related loss of spatial information; and (iii) possible applications for flood risk management. The results show that spatial integration leads to improvements of rain intensities and evaluation scores; however, it also leads to decreased applicability for estimating high-intensity rainfall events that affect small- and medium-scale basins.

Introduction

The importance of measuring or estimating rain intensities in time and space as accurately as possible is obvious as rain intensities represent a key parameter of the global water cycle and affect all aspects of human life (Thies, 2008). Rainfall events can trigger floods or even flash floods. Flash floods are mostly caused by short high convective rainfall over small- and medium-sized catchments with rapid hydrological response, and hence water levels reach a peak within 1 h to a few hours (Collier, 2007; Borga *et al.*, 2008). Moreover, flooding is one of the most frequent and widely spread causes of loss from natural hazards (Munich Re Group, 2005). Recently, there have been severe flood events due to heavy rainfall, e.g. in France (Atlantic coast; March 2010), Great Britain (North of England, Scotland, Wales; November 2009), Austria (Lower and Upper Austria; June 2009), and Germany (Saxony; August 2002 and 2010) of which at least some flood events in France, Austria, and Germany can be categorised as flash floods. Hence, there is a need for real-time rainfall estimates for nowcasting and short range forecasting of possible flood risks. These issues are of increasing interest due to the growing evidence of climate change. In some regions of the world, this is associated with an increased frequency of high-intensity rainfall events and reduced return periods (IPCC, 2007). The evidence for these changes is increasing, and these changes are likely to continue to intensify in the future (Munich Re Group, 2005; Franke and Bernhofer, 2009). This trend will lead to higher (flash) flood risks in small- and medium-sized mountainous catchments. For the related issues of flood risk management, information about rainfall distribution in space and time is essential. However, rainfall is characterised by high spatio-temporal variability, and its correct detection and quantification in a sufficiently high spatial and temporal resolution remain a challenging task (New *et al.*, 2001; Thies, 2008). Currently, precipitation is measured by rain gauges or is estimated by weather radar and satellites. Rain gauges represent primary data sources, and they deliver direct measured point data with relatively poor spatial resolution (Scofield and Kuligowski, 2003). They are, therefore, unable to depict the intensity and spatial extent of heavy rainfall events (Smith *et al.*, 1996), especially of small-scale convective cells. However, because gauge data are directly measured, they are used to adjust radar rain estimates. Radar delivers indirect measured areal rain intensities at a high spatio-temporal resolution and is, hence, able to depict even small-scale rain events (Scofield and

Kuligowski, 2003). Because of their high quality and resolution, radar data are often used as areal reference and adjustment data for satellite rainfall estimates (e.g. Vicente *et al.*, 1998; Reudenbach, 2003; Roebeling and Holleman, 2009). Radar data are not available for the entire surface of earth because of certain limitations, such as beam blocking by any obstacle between radar station and the target volume, as buildings, mountains, or even large rain drops; the coverage range of the beam; and high cost. Satellite data have the advantage of being able to cover the whole earth surface, and they are increasingly used to improve radar rainfall estimates (Lakshmanan *et al.*, 2006). Geostationary weather satellites offer a high potential for detecting and monitoring area-wide precipitation with relatively high spatio-temporal resolution (Thies, 2008). Satellite rain intensities also represent indirect rain data because they are derived from measured radiances reflected or emitted by the surface, clouds, or the atmosphere. Since the late 1960s, a plethora of satellite-based rainfall algorithms have emerged (Alemseged and Rientjes, 2007). Petty (1995) and Levizzani *et al.* (2002) reviewed the existing algorithms. Most of these algorithms rely on relationships between cloud top temperatures and/or reflectances measured in the infrared (IR)/visible (VIS) range and rainfall probability and intensity (Thies, 2008), such as the GOES Precipitation Index (Arkin and Meisner, 1987) and the Convective Stratiform Technique (Adler and Negri, 1988). These algorithms are appropriate for convective systems, especially in the tropics. However, they show deficiencies in detecting extra-tropical cyclones and mixtures of convective and stratiform precipitation that are typical for frontal rain bands in the mid-latitudes (Houze, 1993, 1997; Thies *et al.*, 2008; Roebeling and Holleman, 2009). As a result of the technological progress made during the last few decades, space-borne rainfall measurements have been improved (Levizzani *et al.*, 2002; Ebert *et al.*, 2007) and applied to several events (Vicente *et al.*, 1998; Bendix *et al.*, 2001). Further algorithm developments have aimed at resolving shortcomings by including additional physical cloud properties such as effective cloud droplet radius or optical cloud thickness (Ba and Gruber, 2001; Roebeling and Holleman, 2009); additional data like orography or radiosondes (Vicente *et al.*, 1998); outputs of cloud or numerical models (Reudenbach *et al.*, 2007); or combination with other sensors like passive microwave instruments (Heinemann *et al.*, 2002). Today, for example, EUMETSAT is routinely generating satellite-based rainfall products such as the Satellite Application Facility's (SAF) Convective Rainfall Rate (CRR), the Meteorological Products Extraction Facility's (MPEF) High Resolution Precipitation Index, and the Multi-Sensor Precipitation Estimate (MPE).

As satellite-based estimate algorithms have become more complex, they are more computationally and time intensive. With a focus on flood-related rainfall events with short-lead times, four fast-working algorithms (Kurino, 1997a; Vicente *et al.*, 1998; Ba and Gruber, 2001; Reudenbach, 2003) were tested in this study regarding their applicability for deriving rain intensities in the mid-latitudes using Meteosat Second-Generation (MSG) data. Saxony (Germany) was chosen as the study region because it is prone to (flash) flooding due to its orography and climate (SMUL, 2005), which is likely to increase in frequency and severity in the future (SMUL, 2008; Franke and Bernhofer, 2009). The algorithms were applied to 9 days with high rainfall amounts and to five spatial resolutions to examine the measure of improvement by spatial integration, the related loss of spatial information, and their suitability for flood risk management. An examination of the effects and results of temporal integration will be presented in a second part to this paper (Görner *et al.*, 2011).

Case-study region and data

Selected area and selected days with high rainfall amounts

The Free State of Saxony (Germany) was used as a test area, as it is representative of the mid-latitudes. Saxony's area covers approximately 18 400 km^2 between 11.9°–15.0°N and 50.2°–51.7°E, and is characterised by areas of low altitude as well as medium-elevation mountains (Figure 1). The mountainous region is part of the Ore Mountains, which has heights up to 1200 m a.s.l. Because of its location within the moderately cool west wind zone and with the SW–NE-oriented Ore Mountains, Saxony is prone to heavy rainfall events, especially in the mountainous regions with small and medium catchments and short flood response times (SMUL, 2005). Therefore, there is a high flash flood risk in the study region. The rivers within the study region that are most prone to flooding include the *Müglitz* (214 km^2), the *Gottleuba* (252 km^2), the *Weißeritz* (390 km^2), the *Zschopau* (1847 km^2), the *Freiberger Mulde* (1138 km^2), and the *Zwickauer Mulde* (2361 km^2).

The study region is well covered by rain data from the radar station *Dresden-Klotzsche* and 38 radar calibration rain gauges. Data of atmospheric conditions were provided by the radiosonde station *Lindenberg*, which is located north of the study region (Figure 1).

For the case study, 9 days between May and August 2006 (Figure 2) with convective high daily rainfall amounts and with good data coverage were selected with reference to the *Berliner Wetterkarte* (Berliner Wetterkarte, 2006) and the rain gauge data of the German Weather Service (DWD). The stations *Fichtelberg* (1213 m a.s.l.), *Zinnwald* (877 m a.s.l.), *Carlsfeld* (897 m a.s.l.), *Aue* (387 m a.s.l.), and *Marienberg* (639 m a.s.l.) are situated in the Ore Mountains. Figure 2

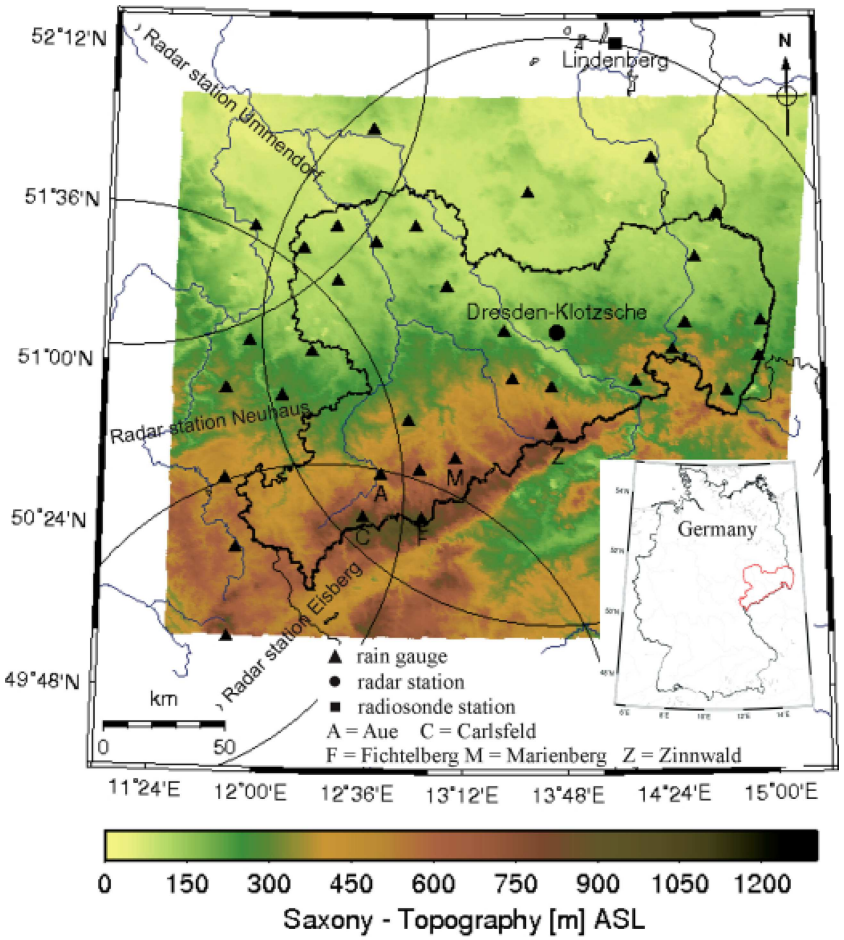

Figure 1 Location and topography of Saxony, including the main radar station *Dresden-Klotzsche* and the three surrounding radar stations with their ranges; the radar calibration rain gauges; the radiosonde station *Lindenberg*.
(Correction added after publication 12 June 2011: Figure 1 has been corrected.)

shows that the highest rainfall amounts occurred mostly in the mountainous region.

Data

Satellite data

The satellite data used were measured by Meteosat-8, the first satellite of EUMETSAT's MSG satellite series. MSG-1 was launched in 2002 and has sent data since January 2004; it had a nominal position of 0° until May 2008. MSG-1 carries the Spinning Enhanced Visible and Infrared Imager (SEVIRI), which is a passive radiometer that observes the full disk of the earth in 12 spectral channels (Table 1) with a repeat cycle of 15 min. In the nadir, channels 1–11 had a spatial resolution of 3 km × 3 km and channel 12 of 1 km × 1 km (Schmetz *et al.*, 2002). Because of a viewing angle of about 58° over Saxony, the spatial resolution was reduced to approximately 3.4 km × 5.9 km and 1.1 km × 2 km for channels 1–11 and 12, respectively.

Weather radar data

The radar data were provided by the DWD, and they represent the reference data for validation. These data are part of the *RADOLAN* product, which covers the entire area of Germany, and they are based on the reflectivities (Z) measured by the 16 German C-band Doppler radar stations, which take a scan every 5 min. The reflectivities are converted into rain intensities (R) by applying a so-called Z–R relation [Eqn (1)], where a and b are empirical parameters that vary in response to current weather and regional characteristics (Bartels, 2004):

$$Z = aR^b \tag{1}$$

The *RADOLAN RW* data used are the result of a correction with rain gauge measurements (Figure 1). These data have a temporal resolution of 1 h and a spatial resolution of 1 km × 1 km (Bartels, 2004). Only few assessments of the quality of *RADOLAN RW* data are available. Jatho *et al.* (2010) found a quality reduction with

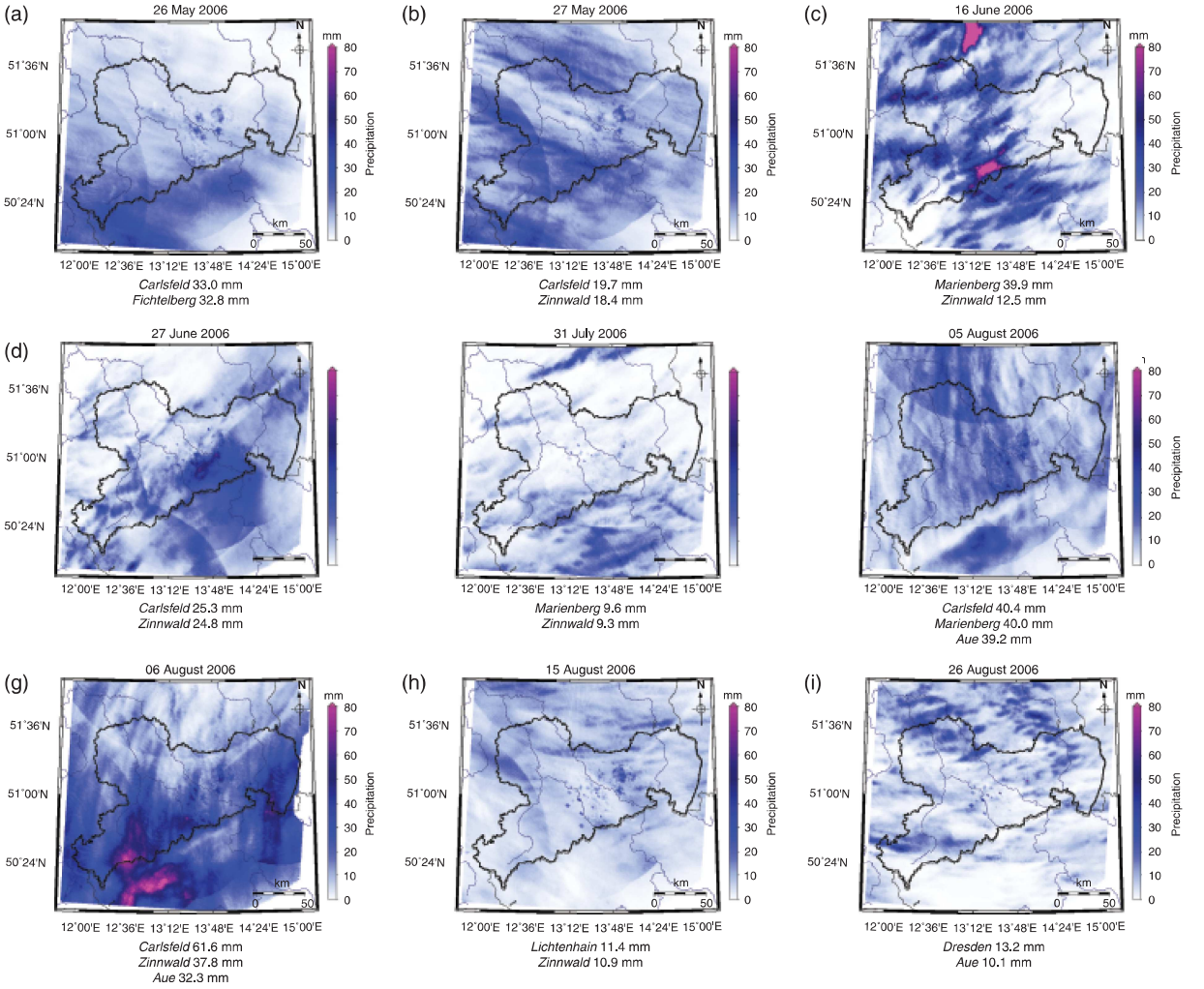

Figure 2 The nine selected days, their daily radar measured rainfall totals (mm), and the rain gauges with the highest daily rainfall totals (mm). (Correction added after publication 12 June 2011: Figure 2 has been corrected.)

Table 1 Spectral channel characteristics of MSG-1 (after Schmetz *et al.*, 2002)

Channel				
Number	Designation	Measurement range (μm)	Spectral range	Main gaseous absorber or atmospheric window
1	VIS 0.6	0.56–0.71	Visible	Atmospheric window
2	VIS 0.8	0.74–0.88	Visible	Atmospheric window
3	NIR 1.6	1.50–1.78	Near infrared	Atmospheric window
4	IR 3.9	3.48–4.36	Infrared	Atmospheric window
5	WV 6.2	5.35–7.15	Infrared	Water vapour
6	WV 7.3	6.85–7.85	Infrared	Water vapour
7	IR 8.7	8.30–9.10	Infrared	Atmospheric window
8	IR 9.7	9.38–9.94	Infrared	Ozone
9	IR 10.8	9.80–11.8	Infrared	Atmospheric window
10	IR 12.0	11.0–13.0	Infrared	Atmospheric window
11	IR 13.4	12.4–14.4	Infrared	Carbon dioxide
12	HRV	0.40–1.10	Visible	Atmospheric window/water vapour

MSG, Meteosat Second Generation.

increasing distance to the radar station. This reduction reaches up to 20% for a maximum distance of 128 km. The differences between the radar-estimated rain intensities and independent rain gauges add up to a mean absolute error of about 1 mm/day for daily rainfall totals. For days with at least 25 mm/day, the mean absolute error is between 6 and 9 mm/day (E. Weigl, personal communication).

Since 2000, the radar station *Dresden-Klotzsche* covers nearly the entire study region (DWD, 2006). For the *RADOLAN RW* data of the study region, 38 rain gauges are utilised for calibration (Figure 1).

Radiosonde data

Radiosonde data were used to obtain information on current atmospheric moisture conditions (precipitable water and mean relative humidity) influencing the rainfall intensity. This information was obtained from 6-hourly radiosonde rises of the DWD station *Lindenberg*, which is located north of the study area (14.1°W, 52.2°N) (Figure 1). The data are available via the website of the Department of Atmospheric Science of the University of Wyoming, USA (http://weather.uwyo.edu).

Methods

The SEVIRI radiometer scans radiation reflected or emitted by the earth's surface, clouds, and atmosphere at different wavelengths (see Table 1). To apply the satellite rainfall algorithms, the measured radiation had to first be converted into radiances. The reflectances (R) and brightness temperatures (T_B), respectively, were then calculable. Both calculation steps were completed by means of the equations presented in Rosenfeld (2005). The reflectances and temperatures represent the input data for the rainfall algorithms, which are outlined below. The methods used to compare the satellite and radar rain intensities follow.

Satellite-based rainfall algorithms

The cloud characteristics that correlate with rainfall and that can be identified at different wavelengths are used to determine rainfall (Sevruk, 2004). There are currently various approaches to estimate satellite-based rainfall (see Levizzani *et al.*, 2002; Reudenbach, 2003). These approaches are based on the determination of a functional relation between ground-based measured rain intensities (rain gauge and radar) and the corresponding spatio-temporal electromagnetic signal in one or several spectral ranges (Menz, 1996). All methods assume that the cloud top brightness temperature is an indicator of rainfall intensity by presuming increasing intensity with higher and hence colder cloud tops (Thies, 2008). The challenge is to distinguish between advective and convective raining clouds (Houze, 1997) and nonraining clouds (e.g. cirrus clouds) (Ba and Gruber, 2001). By a comparison with surface-measured rainfall amounts, regression equations between cloud top temperatures and rain intensities within certain areas are derived and tested to address this challenge.

To examine the applicability of existing satellite rainfall algorithms for estimating rain intensities over Saxony, the following four algorithms were chosen:

- the Operational GOES Infrared Rainfall Estimation Technique [or: Auto-Estimator (AE)] (Vicente *et al.*, 1998);
- the Enhanced Convective Stratiform Technique (ECST) (Reudenbach, 2003);
- the GOES Multispectral Rainfall Algorithm (GMSRA) (Ba and Gruber, 2001);
- the Kurino method (KM) (Kurino, 1997a, b).

Table 2 contains the basic features of the selected algorithms and the MSG channels used. Detailed information on the structure and functionality of the algorithms is given in the related literature.

As none of these algorithms were developed for MSG, each channel used from their respective development satellites had to be replaced. The ECST was developed for Meteosat-7 (Meteosat First Generation). To apply the ECST to MSG, Thies (2008) examined which water vapour (WV) and IR channel of MSG are most suitable for replacement. It was shown that the ECST is applicable to MSG, and the best agreement is achieved when using MSG channels 6 (WV) and 10 (IR) (see Figure 3). As there are no equivalent studies for the other three algorithms, their input channels were replaced by the MSG channels that are most similar in their measurement ranges. For example, Figure 3 shows the four GOES-9 channels (grey lines) used to develop the GMSRA and the proposed MSG replacement channels (black lines). This demonstrates good agreement for the VIS, near infrared, and IR channels. The WV channels show less overlap in their measurement ranges. MSG channel 5 was used in preference to MSG channel 6, as channel 5 has a measurement range from 5.35 to 7.15 μm, and a greater overlap with the GOES-9 WV wavelength than channel 6.

It should be noted that the algorithms were applied to deliver hourly rain intensities (mm/h) for each MSG time step (every 15 min).

Comparing rain intensities from radar and satellite

For the comparisons, the radar estimates represent the reference values. To make the radar and satellite data comparable, they had to be reduced to a common temporal and spatial resolution. As the radar data had a temporal

Table 2 Basic features of the applied algorithms and the MSG channels used

Method	Development satellite/area	Input	Thresholds	Features	MSG channel
AE	GOES/USA	$T_{b,IR}$	$190\,K \leq T_{b,IR} \leq 260\,K$	Moisture and cloud growth correction	9
ECST	Meteosat-7/ Europe (mid-latitudes)	$T_{b,IR}$	$T_{b,IR} < 253\,K$	Discrimination of stratiform and convective rain and redux convection	6
		T_{WV}	$T_{b,WV}-T_{b,IR} > 0\,K$		10
GMSRA	GOES/USA	$T_{b,IR}$	$T_{b,IR} < 250\,K$ (day)	2 parts: day, night	1
		$T_{b,WV}$	$R_{VIS} > 0.4$ (day)	Includes R_{VIS} (day)	4
		R_{VIS}	$T_{b,IR} < 230\,K$ (night)	Moisture and cloud growth correction	5
					9
KM	GMS/Okinawa Islands, Japan	$T_{b,IR}$	$173\,K \leq T_{b,IR} \leq 293\,K$	Working with look-up	5
		$T_{b,WV}$	$T_{b,IR}-T_{b,WV} > 263\,K$	tables containing	9
			$T_{b,IR}-T_{b,WV} < 301\,K$	probability of rain and mean rain intensity	10

T_b, brightness temperature; R, reflectance; AE, Auto-Estimator; ECST, Enhanced Convective Stratiform Technique; GMSRA, GOES Multispectral Rainfall Algorithm; KM, Kurino method; MSG, Meteosat Second Generation; VIS, visible; IR, infrared; WV, water vapour.

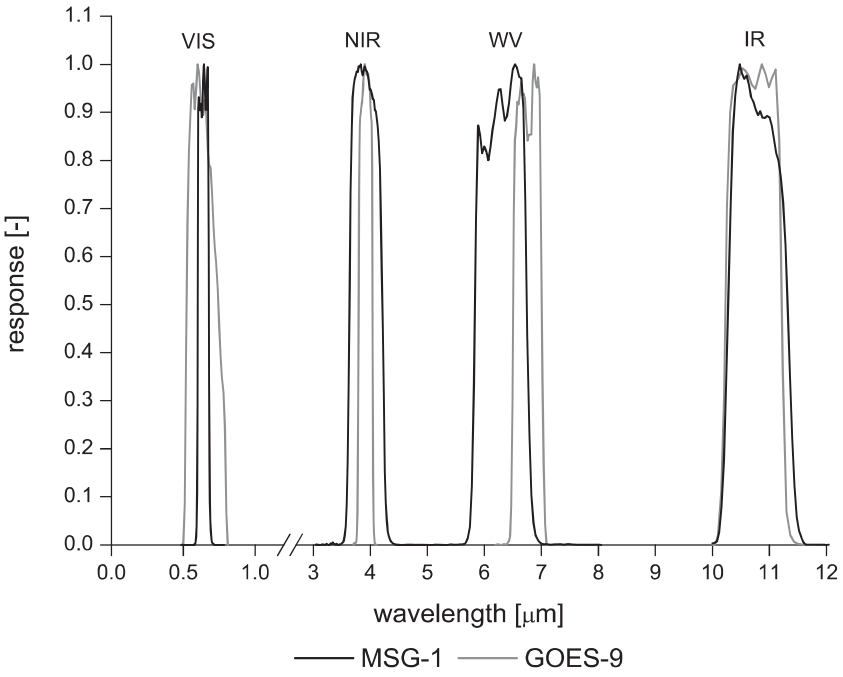

Figure 3 Spectral responses of the four GOES-9 channels of the GOES Multispectral Rainfall Algorithm (GMSRA) and the four Meteosat Second Generation (MSG)-1 replacement channels (data sources: ISCCP, 2006; EUMETSAT, 2007).

resolution of 1 h and MSG of 15 min, the hourly mean MSG rain intensities were calculated by averaging the rainfall intensities from the four radar scans within the hour. For the spatial resolution, the radar data (1 km × 1 km) had to be reduced to the MSG resolution (~3 km × 6 km) by averaging the 18 radar rain intensities covered by one MSG pixel. After calculating this basic resolution, further spatial integration was possible. Reference spatial resolutions used in the papers that present the algorithms and the spatial integration approaches presented in Ba and Gruber (2001) and Porcú *et al.* (1999), resulted in the calculation of four additional resolutions by averaging the rain intensities of the next higher resolution. Hence, the following five resolutions were considered:

- 3 km × 6 km (MSG resolution);
- 6 km × 12 km (close to 6 km × 10 km as used in Reudenbach, 2003);
- 60 km × 60 km (close to 0.5° × 0.5° and 48 km × 48 km as used in Ba and Gruber, 2001 and Vicente *et al.*, 1998, respectively)

Table 3 Contingency table for determination of the evaluation scores (after Wilks, 2006)

	Radar (observation)	
	Yes	No
Satellite (forecast)		
Yes	Hit	False alarm
No	Miss	Correct zero

- 120 km × 120 km (close to 1° × 1° and 100 km × 100 km as used in Kurino, 1997a and Vicente *et al.*, 1998, respectively)
- 240 km × 240 km (entire case-study region).

Adopting the approach of Reudenbach (2003), the performance of the satellite rainfall algorithms can be assessed in terms of their quantity and in terms of their spatial agreement with the radar rainfall using a range of statistics of differences and measures of goodness of fit, respectively.

For the statistical assessment, the data sets from the nine selected days were compared for each spatial resolution by analysing the statistics of the grid-wise absolute differences. For this purpose, the following statistical values were calculated:

- mean ($\bar{x}$);
- median (x_{med});
- mode (x_{mod});
- minimum (x_{min});
- maximum (x_{max});
- standard deviation (σ_x);
- root mean square error (*RMSE*);
- correlation coefficient (r);
- 5% ($x_{5\%}$) and 95% percentile ($x_{95\%}$).

The assessment of spatial agreement can be made using the goodness of fit scores proposed by Wilks (2006) (CAWCR, 2010). To compute these scores, a contingency table containing the grid-wise counted frequencies of hit, false alarm, miss, and correct zero was needed (Table 3). In this study, the radar rain intensities represent the observed data (reference) and the satellite rain intensities are treated as the estimate data. A hit means a correct estimate of a rain intensity > 0.0 mm/h. A false alarm denotes that a satellite rain rate (> 0.0 mm/h) is wrong. If the satellite-based algorithm does not detect a radar rain intensity (> 0.0 mm/h), it is called a miss. If the algorithm estimates an intensity of 0.0 mm/h, where the radar rain intensity is also 0.0 mm/h, it is called correct zero.

On the basis of Table 3, the following evaluation scores are determined (Wilks, 2006):

The probability of detection (*POD*) is the ratio of correct rain estimates to the total number of rain observations and is, hence, a measure of correct estimated satellite rain intensities of > 0.0 mm/h. *POD* ranges from zero (poorest score) to 1.0 (best score). *POD* is computed as

$$POD = \frac{\text{hit}}{\text{hit} + \text{miss}} \tag{2}$$

The false alarm ratio (*FAR*) denotes the proportion of yes estimates that turn out to be wrong. Thus, *FAR* expresses how frequently the satellite-based algorithms estimate misleading rain intensities of > 0.0 mm/h. *FAR*'s value ranges between 0 and 1, where 0 is the best possible value. The *FAR* is equal to

$$FAR = \frac{\text{false alarm}}{\text{hit} + \text{false alarm}} \tag{3}$$

The critical success index (*CSI*) combines *FAR* and *POD* and denotes the number of correct rain estimates divided by the total number of occasions when the rain was estimated and/or observed. The *CSI* focuses on the performance of the algorithm with respect to rain days. The *CSI* can have a value between 0 and 1, where 1 denotes a perfect estimate. The *CSI* is equal to

$$CSI = \frac{\text{hit}}{\text{hit} + \text{false alarm} + \text{miss}} \tag{4}$$

The *Bias* is the ratio of the number of correct rain estimates to the number of rain observations, and its value ranges from 0 to $+\infty$. A score of 1.0 demonstrates no bias in the estimating algorithm, a score > 1.0 indicates overestimation, with a score < 1.0 indicates underestimation (Welle, 2009). The *Bias* is equal to

$$Bias = \frac{\text{hit} + \text{false alarm}}{\text{hit} + \text{miss}} \tag{5}$$

Results and discussion

Rain intensities

The statistical assessment of the performance of each algorithm is presented in Tables 4 and 5. For each of the four tested algorithms, the statistical values contained in these tables reveal that each spatial integration step yields a convergence between satellite and radar rain intensities.

The average correlation coefficients r_{avg} (Table 4) increases over all of the integration steps. They are all statistically significant but indicate only weak correlations for the grid sizes up to 120 km × 120 km. Moreover, even the best values of 0.61 (KM, 240 km × 240 km) and 0.58 (ECST, 240 km × 240 km) show still no satisfying correlation. The correlation coefficients r for the single days cover large ranges, e.g. between -0.34 and 0.91 (GMSRA, 240 km × 240 km). However, these correlation coefficients are statistically significant for at least 5 days for each method and spatial resolution; 8 or

Table 4 Minimum (r_{min}), maximum (r_{max}), average correlation coefficient (r_{avg}), and number of days with a significant r with a probability $P \geq 95\%$ applying a Pearson correlation t-test

Method	Resolution (km^2)	Sample size per day	r_{min} (−)	r_{max} (−)	r_{avg} (−)	Number of days with significant r ($P \geq 95\%$)
AE	3 × 6	76 800	−0.02	0.52	0.16	8
	6 × 12	19 200	−0.02	0.54	0.17	8
	60 × 60	384	−0.02	0.63	0.22	5
	120 × 120	96	−0.05	0.73	0.28	5
	240 × 240	24	−0.29	0.93	0.58	8
ECST	3 × 6	76 800	−0.02	0.32	0.11	9
	6 × 12	19 200	−0.02	0.36	0.13	8
	60 × 60	384	−0.06	0.50	0.17	5
	120 × 120	96	−0.07	0.59	0.20	5
	240 × 240	24	−0.38	0.89	0.45	7
GMSRA	3 × 6	76 800	−0.02	0.37	0.08	8
	6 × 12	19 200	−0.03	0.41	0.10	8
	60 × 60	384	−0.09	0.55	0.16	7
	120 × 120	96	−0.18	0.58	0.20	6
	240 × 240	24	−0.34	0.91	0.42	7
KM	3 × 6	76 800	−0.02	0.39	0.18	9
	6 × 12	19 200	−0.02	0.41	0.19	9
	60 × 60	384	0.01	0.53	0.26	7
	120 × 120	96	0.06	0.64	0.32	5
	240 × 240	24	−0.06	0.93	0.61	8

The correlation coefficients of the 9 days' means are always statistically significant. AE, Auto-Estimator; ECST, Enhanced Convective Stratiform Technique; GMSRA, GOES Multispectral Rainfall Algorithm; KM, Kurino method. (Correction added after publication 12 June 2011: Table 4 has been corrected.)

9 days (almost the complete sample) are significantly correlated in 50% of the investigated cases (Table 4).

Note that the values of mean $\bar{x}$, median x_{med}, and mode x_{mod} are not contained in Table 5. This is because the mean values are independent of spatial integration, the median varied marginally around 0.0 mm/h, while the mode was always 0.0 mm/h for all algorithms. Thus, the mean of the differences has values of −0.2 mm/h (AE), 0.1 mm/h (ECST), −0.3 mm/h (GMSRA), and 0.6 mm/h (KM). For the absolute rain intensities, mean is 0.47 mm/h (radar), 0.3 mm/h (AE), 0.6 mm/h (ECST), 0.16 mm/h (GMSRA), and 1.02 mm/h (KM). Therefore, comparisons across these statistics were considered somewhat redundant.

Table 5 shows that there is a reduction of the largest differences, especially the negative differences for the higher resolutions. However, it must be remembered that the rain intensities are reduced by averaging in the course of spatial integration, which automatically leads to lower differences. High negative differences for the first three integration levels are identical for all four algorithms, as no algorithm was able to detect the highest radar rain intensities, and each estimated a rain intensity of 0.0 mm/h for the corresponding satellite pixel. In contrast, the highest positive differences occurred when high satellite rain intensity coincided with a radar rain intensity of 0.0 mm/h. In comparison with radar, satellite-based algorithms generally estimate more moderate rain intensities due to limits concerning which cloud temperatures are assumed to be rain producing (see Table 2), or because they have a fixed rain intensity as an upper limit. For example, the AE does not permit intensities higher than 72.0 mm/h. For the nine selected days, the maximum intensities were 20.0 mm/h (AE), 30.0 mm/h (ECST), 13.4 mm/h (GMSRA), and 8.0 mm/h (KM); but the intensity was 168.4 mm/h for radar.

For each algorithm and integration level, the improvements are also expressed by the reduction of the standard deviation σ_x and of the *RMSE*, e.g. for the GMSRA ranging from 1.71 to 0.55 mm/h and from 1.54 to 0.56 mm/h, respectively. Furthermore, the interval covered by 90% of the differences gets smaller. The maximum range is between −2.29 and 3.23 mm/h (ECST, 3 km × 6 km). Despite improvements in the magnitude of the inter-ninety-percentile range, the problem of poor performance at the highest rainfall intensities remains. This problem cannot be solved by spatial integration, because the extreme rain intensities are at a small scale, and their data are lost by integration.

By comparing the number of positive and negative differences for each algorithm and resolution, the ECST and the GMSRA always underestimate the radar rain intensities, the KM always overestimate them, whereas the AE overestimates for the first three integration steps and underestimates at the resolutions 120 km × 120 km and 240 km × 240 km.

The satellite rainfall estimates show increasing agreement with the radar intensities through spatial integration. However, at small spatial scales, high differences remain.

Table 5 Statistics of the absolute differences of the satellite and radar rain intensities for the nine selected days

Method	Resolution (km^2)	Sample size per day	x_{min} (mm/h)	x_{max} (mm/h)	σ_x (mm/h)	$x_{5\%}$ (mm/h)	$x_{95\%}$ (mm/h)	*RMSE* (mm/h)
AE	3 × 6	76 800	− 168.4	20.0	1.79	− 2.24	1.00	1.57
	6 × 12	19 200	− 130.8	16.9	1.71	− 2.23	0.98	1.51
	60 × 60	384	− 21.0	11.5	1.22	− 1.78	0.86	1.10
	120 × 120	96	− 9.1	7.8	0.95	− 1.47	0.82	0.87
	240 × 240	24	− 2.5	2.6	0.61	− 1.00	0.99	0.59
ECST	3 × 6	76 800	− 168.4	30.0	3.16	− 2.29	3.23	2.67
	6 × 12	19 200	− 130.8	28.9	3.05	− 2.25	2.33	2.56
	60 × 60	384	− 21.0	24.6	2.52	− 1.83	2.93	2.05
	120 × 120	96	− 5.4	18.4	2.08	− 1.42	3.12	1.66
	240 × 240	24	− 2.2	7.6	1.40	− 1.02	3.39	1.11
GMSRA	3 × 6	76 800	− 168.4	13.4	1.71	− 2.31	0.73	1.54
	6 × 12	19 200	− 130.8	12.1	1.61	− 2.27	0.65	1.45
	60 × 60	384	− 21.0	7.6	1.09	− 1.8	0.50	1.01
	120 × 120	96	− 9.0	4.5	0.82	− 1.42	0.45	0.79
	240 × 240	24	− 2.6	2.0	0.55	− 1.08	0.19	0.56
KM	3 × 6	76 800	− 168.4	8.0	1.89	− 1.44	3.15	1.86
	6 × 12	19 200	− 130.8	7.7	1.81	− 1.44	3.11	1.80
	60 × 60	384	− 21.0	6.1	1.37	− 1.05	2.93	1.41
	120 × 120	96	− 7.6	5.0	1.12	− 0.89	2.58	1.19
	240 × 240	24	− 0.6	2.8	0.76	− 0.30	2.18	0.84

AE, Auto-Estimator; ECST, Enhanced Convective Stratiform Technique; GMSRA, GOES Multispectral Rainfall Algorithm; KM, Kurino method; *RMSE*, root mean square error. (Correction added after publication 12 June 2011: Table 5 has been corrected.)

Therefore, satellite rainfall estimates, based on the algorithms assessed here, are most appropriate for use at lower spatial resolutions, larger catchments, and longer time periods (cp. Görner *et al.*, 2011).

On the basis of the results presented so far, it is not possible to state which is the best performing algorithm of the four assessed. The performance of each algorithm in estimating the spatial extent of rainfall was therefore considered in the assessment.

Evaluation scores

Figure 4 shows the results for the calculated evaluation scores for each algorithm and spatial resolution. As expected, integration leads to improvements in each score. More precisely, integration leads to increasing values of *POD* and *CSI* and decreasing values of *FAR* and *Bias*. The improvements, averaged over the algorithms and related to the optimum score values, have the following amounts: *POD* = +39%, *FAR* = +41%, *CSI* = +46%, and *Bias* = +33%. In parts, the scores nearly reach their optimum values (cp. 'Evaluation scores') at the highest integration level. For example, the *POD* is approximately 1.0 for the KM and 0.9 for the AE. The *FAR* is nearly 0.0 for the ECST and only 0.1 for the AE and the KM. For the *CSI*, the best values result for the KM (∼0.85) and the AE (0.8). The AE also delivers the best value for the *Bias* (∼1.0), followed by the value delivered by the KM (∼1.15). All four algorithms show pronounced improvements between the resolutions 6 km × 12 km and 60 km × 60 km as this is the largest spatial integration step, in terms of percentage increase. Regarding the four scores together, the AE shows the best results for the last integration level and the GMSRA shows the worst values. The ECST shows the highest degree of improvement, but there were no satisfying values for the *POD*, *FAR*, and *CSI*.

These results support the findings presented earlier that satellite estimates are best used at lower spatial resolutions and larger catchments. They show greatest agreement with radar rainfall estimates at coarser spatial integration. Therefore, satellite data may deliver useful information on the spatial extent of rainfall in larger catchments and over longer time periods (cp. Görner *et al.*, 2011) and for regions where alternative data (gauges or radar) are missing.

Effects of spatial integration

The results presented here show that each spatial integration step leads to improved agreement for the analysed statistical differences as well as for the evaluation scores. Therefore, the best results are achieved for the largest resolution tested of 240 km × 240 km. However, this resolution is not suitable for assessing possible flood risks for relatively small catchments in mid-latitude regions (typical size of flash flood-prone basins is well below 1000 km^2 (Samuels *et al.*, 2009), see catchment sizes in 'Case-study region'). For the higher resolutions tested that would be suitable for these catchments, the rainfall algorithms perform poorly in reproducing both rainfall intensities and the spatial extent of rainfall.

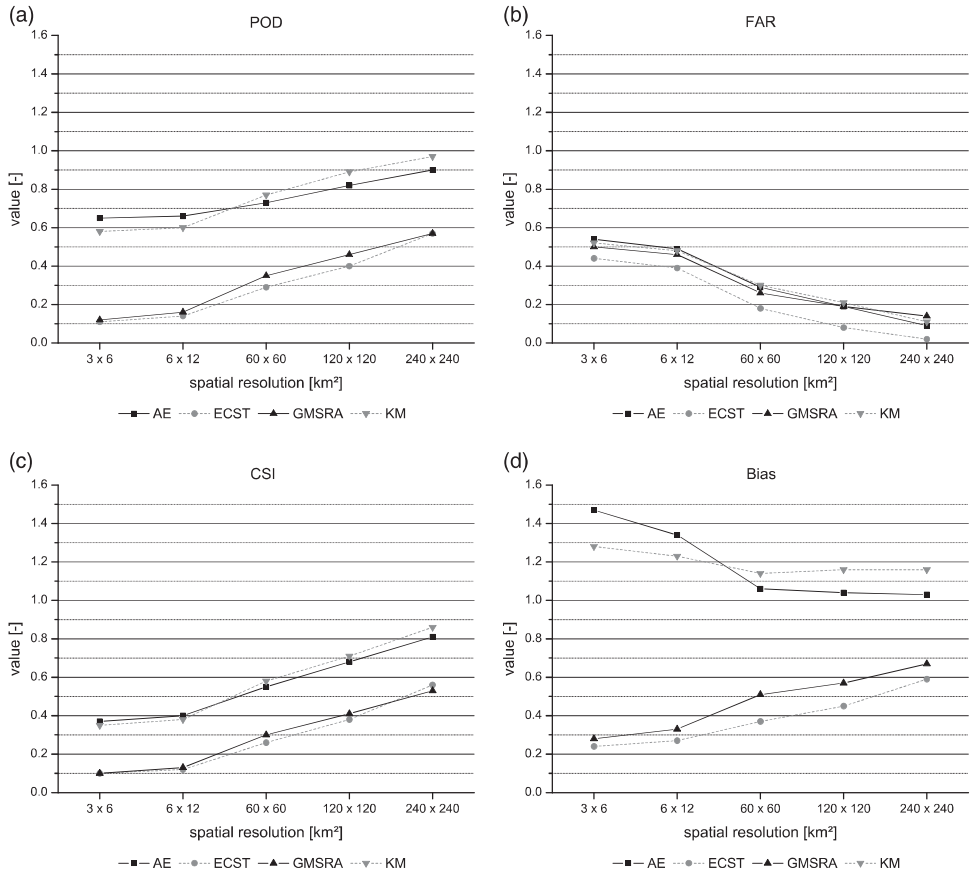

Figure 4 Values of (a) probability of detection (*POD*), (b) false alarm ratio (*FAR*), (c) critical success index (*CSI*), and (d) *Bias* for the five spatial resolutions of the algorithms Auto-Estimator (AE), Enhanced Convective Stratiform Technique (ECST), GOES Multispectral Rainfall Algorithm (GMSRA), and Kurino method (KM).

These results are consistent with those of Porcú *et al.* (1999) and Ba and Gruber (2001). In addition, Negri and Adler (1993), Scofield and Kuligowski (2003), and the results of our present study, satellite estimate algorithms smooth out the rain intensities by a general underestimation of high rain intensities and by a partial overestimation of lower rain intensities.

Although the AE and the KM have their deficiencies in detecting the radar rain intensities in correct amount and location, they deliver the best rain intensities of the four tested algorithms. This provides some support for their use as the basis for the SAF product CRR (Vicente, 2001).

Weakness associated with satellite-based rainfall estimates

The satellite-related problems result from several uncertainties and sources of error concerning the measurement system, the data, and the algorithms used. Satellites operate from the top of atmosphere and with an increasing scanning angle depending on the distance from the nadir. Because of this characteristic and the roll and rotation of the satellite, as well as the projection, correct geo-referencing of the satellite data is difficult. Furthermore, only the radiation of cloud tops is scanned. However, the relation between the temperatures and reflectances of cloud tops and surface-reaching rainfall is quite weak (Alemseged and Rientjes, 2007). This is especially the case in the mid-latitudes, which have a specific rainfall characteristic in that advective and convective events can occur at the same time. In addition, orography, wind, and complex cloud and rain-producing processes are difficult to assess and, thus, to take into account. Furthermore, the four algorithms used were not developed for the MSG data or for the mid-latitudes (except the ECST).

To solve the estimate-related problems, it is necessary to customise the algorithms, especially for the MSG data and the mid-latitudes (Thies, 2008) as proposed by the Advective–Convective Technique (Reudenbach *et al.*, 2007). Furthermore, the algorithms are more complex by including

additional data like wind, orography, and cloud model outputs (Vicente, 2001; Reudenbach *et al.*, 2007). To improve applicability, it is also helpful to combine data from different systems, such as geostationary/polar orbiting satellites, radar, and passive/active microwave sensors. The MPE (Heinemann *et al.*, 2002) and the precipitation estimates based on the Tropical Rainfall Measuring Mission (Huffman *et al.*, 2006) are examples of such combinations. These combinations deliver improved rain estimates, but currently only for the tropics or oceans (MPE) (Samain and Heinemann, 2007). Moreover, the rainfall-related SAF and MPEF products still show deficiencies for mid-latitude regions as they are partially unavailable for mid-latitudes, suffer from low resolution, or deliver only coarse classes of rain intensities (EUMETSAT, 2009; AEMET, 2010).

Summary and conclusions

This study examines the applicability of four satellite-based rainfall estimates to detect and monitor flood-related heavy rainfall events in mid-latitudes by means of highly resolved MSG-1 data. For this case study, a flood-prone region in the low mountain ranges of Saxony (Germany) and 9 days with high rainfall amounts were selected. The analysis compared satellite with radar rain intensities at five spatial resolutions to investigate the applicability of these satellite algorithms and satellite rainfall intensities for flood risk management. The main conclusions from this study are:

1. Spatial integration leads to an improved agreement of satellite-based rain intensity estimates compared with radar rain intensities. However, integration causes a loss of spatial information and, therefore, reduces the suitability of the satellite estimates to assess spatial rainfall distribution and related flood risks, especially in small and medium catchments.
2. A good accordance concerning the intensities is only achieved at low spatial resolutions of at least 120 km × 120 km. This is larger than the typical catchment size of flash flood-prone basins.
3. For high spatial resolutions of 3 km × 6 km or 6 km × 12 km, which are necessary for the nowcasting of flood-related rainfall events, the results are unsatisfactory.
4. Satellite rainfall algorithms smooth the precipitation field, thus underestimating high rain intensities and overestimating lower rain intensities.
5. The satellite-based rainfall algorithms are limited in estimating extreme rain intensities because they use a fixed rain intensity as an upper limit.
6. To improve the applicability of satellite rainfall estimates for flood risk management, the algorithm has to be customised for the satellite used and the target region.
7. It is necessary to include additional data like wind and orography and to combine the algorithms with other measurement systems.
8. Rain intensities and rain areas derived from passively measured satellite data are currently not suitable for applications in flood risk management for small-scale (flash) floods in mid-latitudes. However, these data may be useful as an indicator of large rainfall totals over periods of several hours to days or when gauging and radar data are missing and the size of the catchment is large.

In a second part of this paper (Görner *et al.*, 2011), the effects of temporal integration will be examined.

Acknowledgements

This study was supported by the European Community's Sixth Framework Programme through the Integrated Project FLOOD*site*, Contract GOCE-CT-2004-505420. The authors wish to thank the German Weather Service (DWD) for providing the radar data and the EUMETSAT's Data Centre for providing the raw satellite data.

References

Adler R.F. & Negri A.J. A satellite technique to estimate tropical convective and stratiform rainfall. *J Appl Meteor* 1988, **27**, 30–51.

AEMET. Product user manual for the 'Convective Rainfall Rate' (CRR – PGE05 v3.1). Agencia Estatal de Meteorologia (AEMET), The EUMETSAT Network of Satellite Application Facilities, NWC SAF – Support to Nowcasting and Very Short Range Forecasting, Code: SAF/NWC/CDOP/INM/SCI/PUM/05, 32pp, 2010. Available at https://www.nwcsaf.org/HD/Main.jsp (accessed 3 January 2011).

Alemseged T.H. & Rientjes T.H.M. Spatio-temporal rainfall mapping from space: setbacks and strengths. In: *Proceedings of the 5th International Symposium on Spatial Data Quality ISSDQ*, Modelling qualities in space and time, ITC, Enschede, The Netherlands, 13–15 June 2007.

Arkin P.A. & Meisner B.N. The relationship between large-scale convective rainfall and cold cloud over the western hemisphere during 1982–84. *Mon Weather Rev* 1987, **115**, 51–74.

Ba M.B. & Gruber A. GOES Multispectral Rainfall Algorithm (GMSRA). *J Appl Meteor* 2001, **40**, 1500–1514.

Bartels H. Projekt RADOLAN. Routineverfahren zur Online-Aneichung der Radarniederschlagsdaten mit Hilfe von automatischen Bodenniederschlagsstationen (Ombrometer). Projekt-Abschlußbericht, 2004. Available at http://www.dwd.de/RADOLAN (accessed 30 May 2011).

Bendix J., Reudenbach C., Taschner S., Ludwig R. & Mauser W. Retrieval konvektiver Niederschläge in Mitteleuropa mit Fernerkundungsdaten und Modellen. *DLR Mitteilungen* 2001, **2001–02**, 69–78.

Berliner Wetterkarte. Jg. 55, Nr. 102, 116, 123, 147, 150, 158, 165, Freie Universität Berlin, 2006.

Borga M., Gaume E., Creutin J.D. & Marchi L. Surveying flash floods: gauging the ungauged extremes. *Hydrol Proc* 2008, **22**, (18), 3883–3885.

CAWCR. Forecast verification: issues, methods and FAQ. Centre for Australian Weather and Climate Research, 2010. Available at http://www.cawcr.gov.au/projects/verification (accessed 22 March 2010).

Collier C. Flash flood forecasting: what are the limits of predictability? *Quart J Roy Meteor Soc* 2007, **133**, (622A), 3–23.

DWD. Der Radarverbund des Deutschen Wetterdienstes. Informationsbroschüre, Deutscher Wetterdienst, Offenbach, 2006. Available at http://www.dwd.de (accessed 30 May 2011).

Ebert E., Janowiak J.E. & Kidd C. Comparison of near-real-time precipitation estimates from satellite observations and numerical models. *Bull Am Meteor Soc* 2007, **88**, (1), 47–64.

EUMETSAT. Spectral responses. 2007. Available at http://www.eumetsat.int/Home/Main/What_We_Do/Satellites/Meteosat_Second_Generation/Space_Segment/SP_1138096039033?l=en (accessed 23 March 2009).

EUMETSAT. MSG meteorological products extraction facility algorithm specification document. Doc. No. EUM/MSG/SPE/022, 255pp, 2009. Available at http://www.eumetsat.int/Home/Main/DataProducts/Resources/index.htm (accessed 3 January 2011).

Franke J. & Bernhofer C. A method for deriving a future temporal spectrum of heavy precipitation on the basis of weather patterns in low mountain ranges. *Meteorol Appl* 2009, **16**, 513–522.

Görner C., Jatho N. & Bernhofer C. Applicability of satellite based rainfall algorithms to estimate flood related rainfall events in the mid-latitudes. Part II: temporal integration. 2011, in preparation.

Heinemann T., Lattanzio A. & Roveda F. The EUMETSAT Multi-sensor Precipitation Estimate (MPE). *Proceedings of the second International Precipitation Working Group (IPWG) meeting*, Madrid, Spain, September 2002.

Houze R.A. *Cloud dynamics. Vol. 53 of international geophysics series*. San Diego, CA, USA: Academic Press, 1993, 573pp.

Houze R.A. Stratiform precipitation in regions of convection: a meteorological paradox? *Bull Am Meteor Soc* 1997, **78**, (10), 2179–2196.

Huffman G.J., Adler R.F., Bolvin D.T., Gu G., Nelkin E.J., Bowman K.P., Hong Y., Stocker E.F. & Wolff D.B. The TRMM Multisatellite Precipitation Analysis (TMPA): quasi-global, multiyear, combined-sensor precipitation estimates at fine scales. *J Hydromet* 2006, **8**, (1), 38–55.

IPCC. *Climate change 2007 – The physical science basis: contribution of working group I to the Fourth Assessment Report of the Intergovernmental Panel on Climate Change (IPCC)*. Cambridge, UK: Cambridge University Press, 2007, 996pp.

ISCCP. ISCCP instrument response functions. 2006. Available at http://isccp.giss.nasa.gov/docs/response.html (accessed 23 March 2009).

Jatho N., Pluntke T., Kurbjuhn C. & Bernhofer C. An approach to combine radar and gauge based rainfall data under consideration of their qualities of low mountain ranges of Saxony. *Nat Hazards Earth Syst Sci* 2010, **10**, 429–446.

Kurino T. A rainfall estimation with the GMS-5 infrared split-window and water vapour measurements. Meteorological Satellite Centre, Technical Note, No. 33, 91–101, 1997a.

Kurino T. A satellite infrared technique for estimating "deep/shallow" convective and stratiform precipitation. *Adv Space Res* 1997b, **19**, 511–514.

Lakshmanan V., Fritz A., Smith T., Hondl K. & Stumpf G. An automated technique to quality control radar reflectivity data. *J Appl Meteor* 2006, **46**, 288–305.

Levizzani V., Amorati R. & Meneguzzo F. A review of satellite-based rainfall estimation methods. European Commission Project Music Report (EVK1-CT-2000-00058), 2002.

Menz G. Niederschlag und Biomasse in den wechselfeuchten Tropen Ostafrikas – Neuere Methoden zur quantitativen Erfassung klimaökologischer Raumparameter aus digitalen Satellitendaten. Erdwissenschaftliche Forschung der Akademie der Wissenschaften und der Literatur Mainz, Band XXXIV, Franz Steiner Verlag Stuttgart, 1996.

Munich Re Group. Weather catastrophes and climate change – Is there still hope for us? Münchener Rückversicherung-Gesellschaft, München, Germany, 2005.

Negri A.J. & Adler R.F. An intercomparison of three satellite infrared rainfall techniques over Japan and sourrounding waters. *J Appl Meteor* 1993, **32**, 357–373.

New M., Todd M., Hulme M. & Jones P. Precipitation measurements and trends in the twentieth century. *Int J Clim* 2001, **21**, 1899–1922.

Petty G.W. The status of satellite-based rainfall estimation over land. *Remote Sen Environ* 1995, **51**, 125–137.

Porcú F., Borga M. & Prodi F. Rainfall estimation by combining radar and infrared satellite data for nowcasting purposes. *Meteorol Appl* 1999, **6**, 289–300.

Reudenbach C. Konvektive Sommerniederschläge in Mitteleuropa. Bonner Geographische Abhandlungen, Heft 109, Asgard-Verlag Sankt Augustin, 2003.

Reudenbach C., Nauss T. & Bendix J. Retrieving precipitation with GOES, meteosat, and terra/MSG at the tropics and mid-latitudes. In: V. Levizzan, P. Bauer & F.J. Turk, eds. *Measuring precipitation from space EURAINSAT and the future*. The Netherlands: Springer, 2007, 509–519.

Roebeling R.A. & Holleman I. SEVIRI rainfall retrieval and validation using weather radar observations. *J Geophys Res* 2009, **114**, D21202, doi: 10/1029/2009JD012102.

Rosenfeld D. Applications of Meteosat Second Generation (MSG) – Conversion from counts to radiances and from radiances to brightness temperatures and reflectances. 2005. Available at http://oiswww.eumetsat.org/WEBOPS/msg_interpretation/msg_channels.php (accessed 30 May 2011).

Samain O. & Heinemann T. MPE Quality Indicators. EUMETSAT, Memorandum, 13 November 2007.

Samuels P., Gouldby B., Klijn F., Messner F., van Os A., Sayers P., Schanze J. & Udale-Clarke H. Language of risk – Project definitions (2nd edn). FLOODsite Report T32-04-01, 2009. Available at http://www.floodsite.net (accessed 12 April 2010).

Schmetz J., Pili P., Tjemkes S.A., Just D., Kerkmann J., Rota S. & Ratier A. An Introduction to Meteosat Second Generation (MSG). *Bull Am Meteor Soc* 2002, **83**, (7), 977–992.

Scofield R.A. & Kuligowski R.J. Status and outlook of operational satellite precipitation algorithms for extreme-precipitation events. *Wea Forecasting* 2003, **18**, 1037–1051.

Sevruk B. Niederschlag als Wasserkreislaufelement – Theorie und Praxis der Niederschlagsmessung. Zürich, Nitra, 2004.

Smith J.A., Seo D.-J., Baeck M.L. & Hudlow M.D. An intercomparison study of NEXRAD precipitation estimates. *Water Resour Res* 1996, **32**, 2035–2045.

SMUL. Klimawandel in Sachsen – Sachstand und Ausblick 2005. Sächsisches Staatsministerium für Umwelt und Landwirtschaft. 109pp, 2005.

SMUL. (ed) *Sachsen im Klimawandel – Eine Analyse. Sächsisches Staatsministerium für Umwelt und Landwirtschaft, Eigenverlag.* Dresden: SMUL, 2008, 211pp.

Thies B. A novel day/night technique for area-wide precipitation retrieval over Central Europe using MSG SEVIRI data. Dissertation, Fachbereich Geographie, Philipps-Universität Marburg, 176pp, 2008. Available at http://archiv.ub.uni-marburg.de/diss/z2008/0906/ (accessed 23 March 2009).

Thies B., Nauss T. & Bendix J. Discriminating raining from non-raining cloud areas at mid-latitudes using meteosat second generation SEVIRI night-time data. *Meteorol Appl* 2008, **15**, 219–230.

Vicente G.A. Satellite rainfall estimation for flash flood application – European basic Auto Estimator within the frame of the SAFNWC. Visiting Scientist's Report, Maryland, 30 January 2001. Available at eumetsat.int/groups/pps/documents/document/002102.pdf

Vicente G.A., Scofield R.A. & Menzel W.P. The operational GOES infrared estimation technique. *Bull Am Meteor Soc* 1998, **79**, (9), 1883–1998.

Welle T. Niederschlagsbestimmung aus METEOSAT-Second Generation Zeitreihendaten mit dem Methodenverbund ORFEUSS – Fallbeispiel Namibia. Dissertation, Rheinische Friedrich-Wilhelm-Universität Bonn, 180pp, 2009.

Wilks D.S. *Statistical Methods in the Atmospheric Sciences. 2nd edn, International Geophysics Series 91.* Amsterdam: Academic Press, Elsevier, 2006, 627pp.

Appendix B

Peer-reviewed publication 2

Journal of
Flood Risk Management

Applicability of satellite-based rainfall algorithms for estimating flood-related rainfall events in the mid-latitudes. Part II: temporal integration

C. Görner, R. Kronenberg and C. Bernhofer

Chair of Meteorology, Institute of Hydrology and Meteorology, Technische Universität Dresden, Tharandt, Germany

Correspondence
Christina Görner, Technische Universität Dresden, Institut für Hydrologie und Meteorologie, Professur für Meteorologie, Pienner Str. 23, 01737 Tharandt, Germany
Tel: +49 351 463 31340
Fax: +49 35203 38 31302
Email: christina.goerner@tu-dresden.de

DOI: 10.1111/j.1753-318X.2012.01138.x

Key words
Flash floods; flood risk; Meteosat Second Generation (MSG); satellite rainfall estimate; temporal integration.

Abstract

In a continuation of Part I on spatial integration, this paper presents research on the applicability of four satellite-based rainfall algorithms to derive hourly rain intensities in the mid-latitudes using highly resolved data from the first Meteosat Second Generation (MSG-1) satellite. It focuses on the suitability of these algorithms to detect and monitor (flash) flood-related rain intensities for different temporal resolutions. The temporal integration is examined using six different integration steps ranging from 1 h to 24 h and three different data-filtering methods. The effects of this temporal integration on the quality of satellite-based rain intensities (amounts and locations) are examined with regard to heavy and possible flood-triggering rain intensities. Also, loss of temporal information and possible applications for flood risk management are considered. For this purpose, Saxony (Germany) is used as an example, and 9 high-rainfall days between May and August 2006 were analysed by comparing satellite rain intensities to rain gauge-adjusted radar data. The results show that temporal integration leads to improvements in evaluation scores, especially for heavy rain intensities, by up to +62%. However, this integration leads to a decreased applicability for the detection of high-intensity rainfall events because they tend to be short in duration.

Introduction

Due to the importance of rainfall in the global water cycle and all aspects of human life, measuring or estimating it in time and space as accurately as possible is an obvious necessity (Thies, 2008). Rainfall events can trigger floods, which are one of the most frequent and widespread causes of economic and human loss from natural hazards (Munich Re Group, 2005). For example, severe floods recently occurred in France (Atlantic coast; March 2010), Great Britain (North of England, Scotland, Wales; November 2009), and Germany (Saxony; August 2010). These events illustrate the need for real-time rainfall estimates for nowcasting and short-range forecasting of possible flood risks. There is increasing interest in obtaining these estimates because of the growing evidence of climate change associated with an increased frequency of high-intensity rainfall events and reduced return periods of such events (IPCC, 2007). This trend is likely to continue to intensify in the future, both locally in Germany and globally (Munich Re Group, 2005; Franke and Bernhofer, 2009). As it will result in concomitant higher flash flood risks in small- and medium-sized mountainous catchments, information on rainfall distribution in space and time is essential for the management of flood risks. Flash floods are defined as flooding events predominantly caused by short, convective, rainfall events over small- and medium-sized catchments that induce a rapid hydrological response with water levels peaking in a few hours or less and accordingly short lag times of mostly less than 6 h (Collier, 2007; Borga *et al.*, 2009; Marchi *et al.*, 2010). Flash flood inducing storms are mostly associated with convective cells or mesoscale convective systems with space–time scales of 10–1000 km^2 and <1–30 h (Borga *et al.*, 2008). Studies on spatial and temporal rainfall aggregation showed that aggregation leads to dampened mean intensities, to smoothed variability and to significant rainfall volume errors (Sangati *et al.*, 2009; Anquetin *et al.*, 2010). Precipitation can be measured by rain gauges or estimated by weather radar and satellites. Each of these systems has advantages and disadvantages. Rain gauges provide greater accuracy in the measurement of point rainfall depths, while radar and satellite techniques allow for greater spatial representation of rainfall

events (Görner *et al.*, 2011). In this study, the focus is on satellite-based rainfall estimates that are derived from measured radiances that are reflected or emitted by the surface, the clouds, or the atmosphere; these estimates represent indirect rainfall measurements. A plethora of satellite-based rainfall algorithms has been developed through the years (see Petty, 1995; Levizzani *et al.*, 2002; Görner *et al.*, 2011). Most of these algorithms rely on relationships between cloud-top temperatures and/or reflectances measured in the infrared/visible range and rainfall probability and intensity (Thies, 2008). Despite working well in the tropics, these algorithms still show deficiencies in detecting extratropical cyclones and mixtures of convective and stratiform precipitation that are typical of frontal rain bands in the mid-latitudes (Houze, 1993, 1997; Thies *et al.*, 2008; Roebeling and Holleman, 2009).

Part I (Görner *et al.*, 2011) of the current study addressed the spatial integration of satellite-based extreme rainfall estimates. This study represents a continuation of the work from Part I, and the background and motivation are the same for the two studies; however, where necessary, essential information and basic facts are summarised briefly. As in Part I, four fast-working algorithms (Kurino, 1997a; Vicente *et al.*, 1998; Ba and Gruber, 2001; Reudenbach, 2003) were tested to determine their applicability for deriving rain intensities in the mid-latitudes using Meteosat Second Generation (MSG) data with a focus on flood-related rainfall events with short lead times. Saxony (Germany) serves as the study region again because it is prone to (flash) flooding due to its orography and climate (SMUL, 2005). The algorithms were also applied to the same 9 high-rainfall days selected in Part I. Six different temporal resolutions and three additional types of data filtering were used to quantify the improvement due to temporal integration, the related loss of temporal information, and the suitability of the applied algorithms for flood risk management.

Case study region and data

As in Part I (Görner *et al.*, 2011), the selected case study region is the Free State of Saxony (Germany), which is characterised by areas of low elevation as well as medium-elevation mountains (Ore Mountains). As in Part I, the same 9 days with high convective rainfall events between May and August 2006 (Figure 1) were selected.

This study used three types of data:

- satellite data: measured by the first satellite of MSG (MSG-1) with a temporal resolution of 15 min and a spatial resolution of approximately 3 km × 6 km over Saxony (Schmetz *et al.*, 2002)
- radar data: German Weather Service's (DWD) *RADOLAN RW* product with a temporal resolution of 1 h and a spatial resolution of 1 km × 1 km (Bartels, 2004)
- radiosonde data: measured by the DWD at the *Lindenberg* station every 6 h

See Görner *et al.* (2011) for a more detailed description of the case study region and the data.

Methods

The four satellite-based rainfall algorithms used in this study were chosen to examine the applicability of existing satellite rainfall algorithms for estimating rain intensities over Saxony. The four algorithms used for this purpose are the Operational GOES Infrared Rainfall Estimation Technique [or Auto-Estimator (AE)] (Vicente *et al.*, 1998); the Enhanced Convective Stratiform Technique (ECST; Reudenbach, 2003); the GOES Multispectral Rainfall Algorithm (GMSRA; Ba and Gruber, 2001); and the Kurino (1997a, b) method (KM).

Detailed information on the algorithms and the MSG channels used in this study may be found in the related literature mentioned above and in Görner *et al.* (2011), respectively.

In the next section, the methods used to compare the satellite and radar estimated rain intensities are described.

Comparing rain intensities estimated from radar and satellite

The radar rainfall estimates represent the reference values used to determine the accuracy of the satellite algorithms. For comparability, the radar and satellite data had to be reduced to a common temporal and spatial resolution of 1 h and 3 km × 6 km, respectively (Görner *et al.*, 2011). Based on this common resolution, further temporal integration was possible.

To examine the effects of temporal integration, six rainfall totals of 1 h, 3 h, 6 h, 12 h, 18 h, and 24 h were used. To detect and include the largest individual intensities for each total, running totals with a time lag of 1 h were calculated for all temporally integrated periods except 24 h, as only 24 consecutive hours were addressed for each of the 9 sample days. This method expands the data basis and covers the largest individual intensities of all time integrations.

According to Reudenbach (2003) and Görner *et al.* (2011), the performance of the satellite rainfall algorithms was examined using measures of goodness of fit and a range of statistics of differences. By applying four fit scores, the *probability of detection (POD)*, *false alarm ratio (FAR)*, *critical success index (CSI)*, and *Bias*, proposed by Wilks (2006) and described in Görner *et al.* (2011), the spatial agreement of the satellite- (P_{sat}) and radar-based (P_{rad}) rain intensities was assessed for all temporal resolutions for the entire data set.

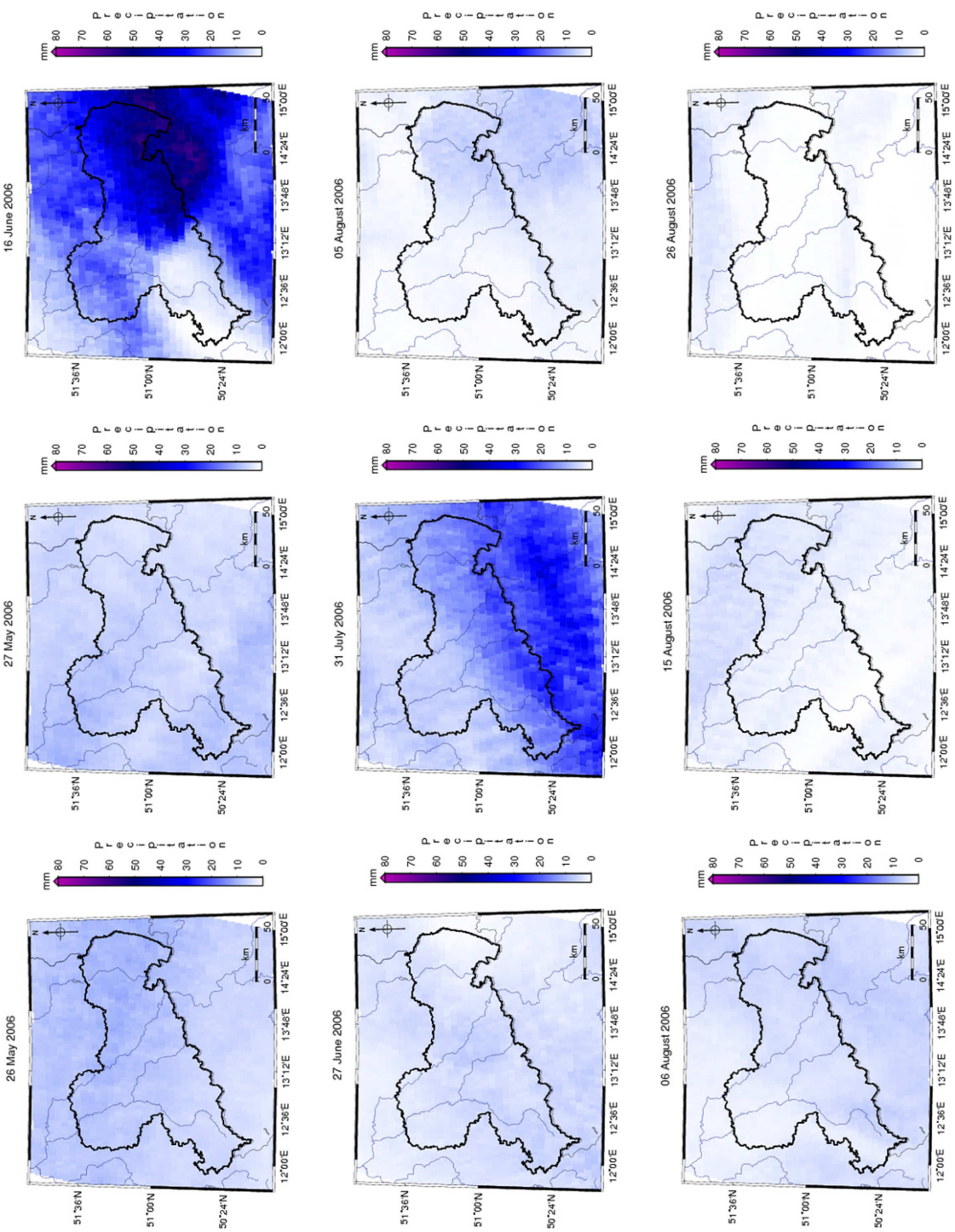

Figure 1 Daily rainfall totals (mm) of the 9 selected days estimated using the Auto-Estimator. For comparability to the radar-estimated daily rainfall totals, the colour scale is in accordance with Figure 2 in Part I (Görner *et al.*, 2011).

For each temporal resolution, the statistical assessment was analysed by comparing the various statistics with the grid-wise absolute differences (P_{diff}) of the rain intensities for the 9 selected days. The differences were compared by calculating rain intensities in mm/h for each rainfall total assuming a block rain model. This model is a rather simple but commonly used model for the description and disaggregation of rain over a certain time period.

In this study, for each temporal resolution, the following statistical values were calculated for the absolute differences of the rain intensities: the mean ($\overline{x}$), median (x_{med}), mode (x_{mod}), minimum (x_{min}), maximum (x_{max}), standard deviation (σ_x), and correlation coefficient (r), 5% ($x_{5\%}$) and 95% ($x_{95\%}$) of the empirical distribution, as described in Part I (Görner *et al.*, 2011). In addition, the following values were calculated:

- 10% ($x_{10\%}$) and 90% ($x_{90\%}$)
- 25% ($x_{25\%}$) and 75% ($x_{75\%}$)
- relative frequencies of the differences

Statistical analyses were performed for four different data sets of differences $Z_{1\ldots4}$ with radar P_{rad}, satellite P_{sat}, and difference P_{diff} pixels in mm/h. The data sets $Z_{1\ldots4}$ are computed as:

1. Without filtering:

$$P_{diff} = P_{sat} - P_{rad}\,(\mathrm{mm/h})\,\{P_{diff} \in Z_1\} \quad (1)$$

2. Filtering for the rainfall area: the pixels with both a radar- and a satellite-estimated rain intensity of 0.0 mm/h were excluded.

$$P_{diff} = P_{sat} - P_{rad}\,(\mathrm{mm/h})\ \text{if}\ \overline{P_{sat} = 0 \cap P_{rad} = 0}\,\{P_{diff} \in Z_2\} \quad (2)$$

3. Filtering for an overlapping rainfall area: only pixels that had both a radar- and satellite-based rain intensity of >0.0 mm/h were used.

$$P_{diff} = P_{sat} - P_{rad}\,(\mathrm{mm/h})\ \text{if}\ P_{sat} > 0 \cap P_{rad} > 0\,\{P_{diff} \in Z_3\} \quad (3)$$

4. Filtering for heavy rainfall: with regard to flood-related issues, only the pixels that had a radar-based rain intensity $\geq P_{Wussow}$ were considered; pixels of this intensity represent the minimum rain intensity that defines heavy rainfall (Wussow, 1922):

$$P_{Wussow}(D) = \sqrt{5D - \left(\frac{D}{24}\right)^2}\ (\mathrm{mm}/D) \quad (4)$$

where D is the duration (min).

$$P_{diff} = P_{sat} - P_{rad}\,(\mathrm{mm/h})\ \text{if}\ P_{rad} \geq P_{Wussow}\,\{P_{diff} \in Z_4\} \quad (5)$$

The minimum rainfall intensities for each temporal resolution are listed in Table 1 both as intensity P_{Wussow} in mm/D and as the corresponding mean hourly intensity P_{mean} in mm/h.

Table 1 Minimum rainfall intensity P_{Wussow} (mm/D) and the corresponding hourly intensity P_{mean} (mm/h)

D (min)	60	180	360	720	1080	1440
P_{Wussow} (mm/D)	17.1	29.0	39.7	52.0	58.1	60.0
$\triangleq P_{mean}$ (mm/h)	17.1	9.7	6.6	4.3	3.2	2.5

Results and discussion

Evaluation scores

The results for the calculated evaluation scores for each algorithm and temporal resolution are shown in Figure 2. As expected, and in agreement with the results for spatial integration (Görner *et al.*, 2011), temporal integration leads to considerable improvements in each score. More precisely, integration leads to increasing values of *POD* and *CSI* and decreasing values of *FAR*. Concerning *Bias*, it leads to decreasing values for AE and KM and increasing values for ECST and GMSRA. Both trends indicate improvement towards the perfect value of *Bias* (1.0). Improvements in these four variables can be seen in the averages over all algorithms related to the optimum score values: *POD* = +39%, *FAR* = +45%, *CSI* = +53%, and *Bias* = +32%. At the highest integration level, some scores tend to their optimum values (Görner et al., 2011). For example, *POD* tends to 1.0 for AE and KM; *FAR* is nearly 0.0 for each algorithm; *CSI* is 0.97 for AE and KM; and *Bias* is approximately 1.0 for AE and KM. For the four scores, AE and KM show the best results at the largest integration level, while ECST shows the poorest results except for the *FAR* score. The highest degree of improvement for *POD* occurs with GMSRA at +48% and for *CSI* with AE at +62%. For *FAR* and *Bias*, the highest improvement is with the KM at +50% each. However, there is almost no further improvement for the 24-h integration level. This tendency is most distinct for the *Bias* with the AE, the GMSRA, and the KM; for the *POD* with the GMSRA and the KM; for the *FAR* with each algorithm; and for the *CSI* with the GMSRA (Figure 2). The reduced improvement for the 24-h level results from the high spatio-temporal variability of short intense rain events and the limit of temporal integration to smooth out the errors of the related satellite-based estimates.

Rain intensities

Certainly, the four algorithms show individual differences in the results, but AE performed slightly better. As the differences were addressed already in Part I of this study (Görner *et al.*, 2011), here, only the results for AE are presented in detail, which are representative for all four algorithms.

The results for the entire data set are shown in Figure 3 and in the Tables 2 and 3. An improvement in the range of the quantiles for each temporal integration step can be seen. The ranges covered by 90% of the differences of the satellite-

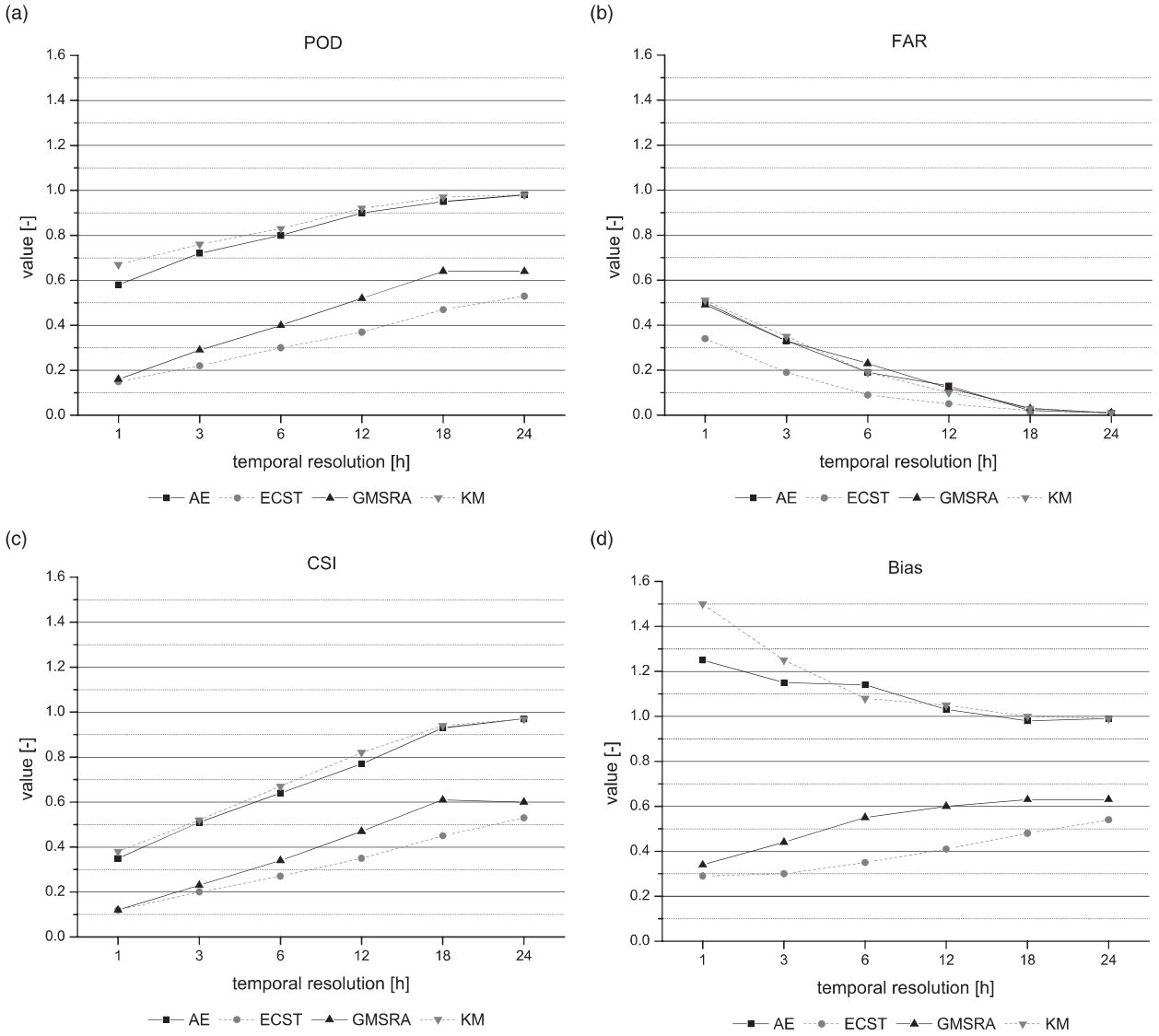

Figure 2 Scores related to the temporal resolution for (a) the probability of detection (*POD*); (b) the false alarm ratio (*FAR*); (c) the critical success index (*CSI*); and (d) the *Bias* for the five temporal resolutions of the algorithms Auto-Estimator (AE), Enhanced Convective Stratiform Technique (ECST), GOES Multispectral Rainfall Algorithm (GMSRA), and Kurino method (KM).

and radar-based rain intensities are 3.2 mm/h for the 1-h resolution and 1.8 mm/h for the 24-h resolution.

On the right side of Figure 3, the related distributions of the relative frequencies of the differences are shown only for the most relevant and central range from −1.5 mm/h to 1.5 mm/h because the frequencies are close to zero outside this range (see the quantiles in Figure 3), and the range covered by all differences is very large (e.g. from −168 mm/h to 20.0 mm/h for 1 h; Table 2). At a difference of 0.0 mm/h, the higher temporal resolutions of 1 h, 3 h, and 6 h show distinct peaks in the relative frequencies of 0.5, 0.4, and 0.25, respectively. For the range of small negative differences (around −0.2 mm/h), an increase of the relative frequencies is observed over each integration step. Figure 3 shows less distinct improvements for the percentile range and the changes in the relative frequency distributions for integration levels >12 h, especially for the step from 18 h to 24 h. As described above for the evaluation scores, this lack of improvement can be attributed to the use of running rainfall totals for the levels ≤ 18 h.

The decreasing peak and the small shift to negative differences as the integration levels increase may indicate that the satellite-based rain intensities perform best for higher temporal resolutions such as 1 h or 3 h. In contrast to the decreasing peak, Table 2 shows that the standard deviation decreases with each integration step (from 1.79 mm/h to

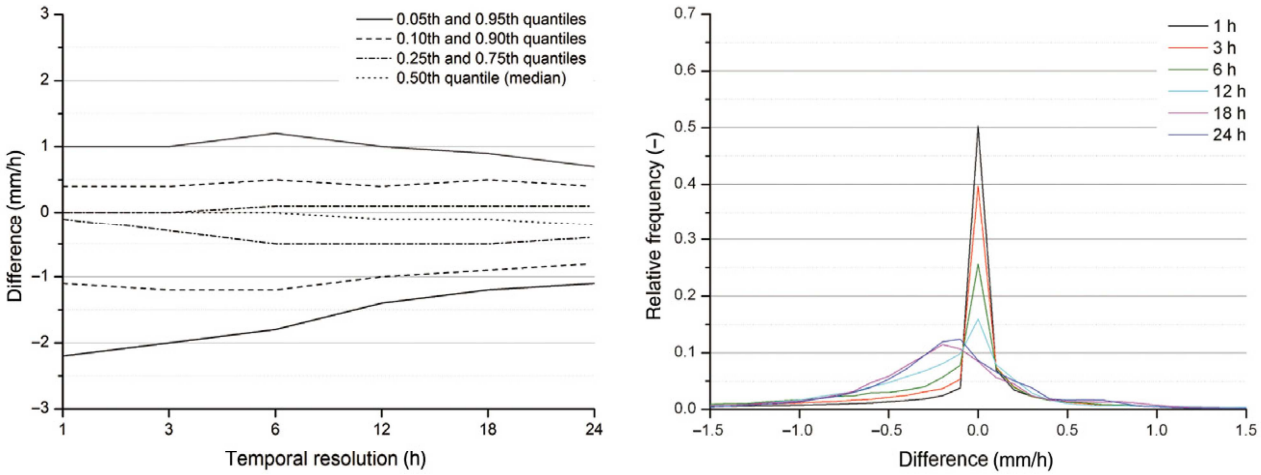

Figure 3 Quantile values (left) and the central range (from –1.5 mm/h to 1.5 mm/h) of the relative frequencies (right) of the differences (mm/h) of the satellite and radar rain intensities for the entire data set of the Auto-Estimator.

Table 2 Statistics of the absolute differences (mm/h) of the satellite and radar rain intensities for the entire data set for Auto-Estimator

Temporal resolution (h)	Number of values (–)	x_{min} (mm/h)	x_{max} (mm/h)	$\bar{x}$ (mm/h)	σ_x (mm/h)	x_{mod} (mm/h)
1	632 071	–168.4	20.0	–0.17	1.79	0.0
3	570 621	–56.4	12.5	–0.18	1.24	0.0
6	367 997	–18.7	8.3	–0.19	1.06	0.0
12	303 544	–14.3	5.0	–0.19	0.76	0.0
18	147 108	–9.2	3.3	–0.20	0.66	–0.2
24	27 586	–7.2	2.6	–0.17	0.58	–0.1

Table 3 Number of values, minimum correlation coefficient (r_{min}), maximum correlation coefficient (r_{max}), average correlation coefficient (r_{avg}), and the number of days with a significant r with a probability $P \geq 95\%$ applying a Pearson correlation t-test for the entire data set for Auto-Estimator

Temporal resolution (h)	Sample size per day (–)	r_{min} (–)	r_{max} (–)	r_{avg} (–)	Number out of 9 days with significant r ($P \geq 95\%$)
1	76 800	0.04	0.49	0.21	9
3	70 400	0.03	0.62	0.29	9
6	60 800	0.02	0.56	0.28	9
12	41 600	–0.13	0.53	0.29	9
18	22 400	–0.14	0.47	0.21	8
24	3 200	–0.65	0.50	0.11	9

Note: The correlation coefficients of the 9 days' means are all statistically significant.

0.58 mm/h) and that the range covered by the differences decreases by a large amount (from 188.4 mm/h to 9.8 mm/h). These decreases can be explained by two factors. First, the block rain assumption leads to a smoothening of relative peaks over the integrated time period and, second, the higher variability of large rain intensities at smaller time scales.

The empirical distributions of the differences do not follow a Gaussian distribution. For this reason, a fitting of generalised normal distributions on the unfiltered data set of differences is recommended for further analysis.

Additionally, the correlation coefficient r between P_{rad} and P_{sat} (mm/h) was examined for the entire data set Z_1 for each of the 9 selected days. The results in Table 3 show no consistent characteristics over the integration steps. The minimum correlation coefficient r_{min} decreases with the temporal integration, but the r_{max} has no clear trend, varying across the integration steps and has its highest value (0.62) at the 3-h resolution. The correlation coefficients for the single days cover large ranges, e.g. 24-h period ranges from –0.65 to 0.50. However, the correlation coefficients are statistically

significant for all 9 days and for each temporal resolution except for 18 h where only 8 days are significantly correlated. The average correlation coefficients r_{avg} are also all statistically significant but indicate weak correlations for all resolutions. The average correlation coefficient is highest for 3 h and 6 h with a value of 0.29 and lowest for 24 h with a value of 0.11.

The results for the different time integrations do not stratify according to their lengths because there is no trend in the correlation coefficients (Table 3) or the distribution of the relative frequencies (Figure 3).

To focus on performance under heavy precipitation and possible flash flood-causing rain intensities, the data set, as outlined earlier, was filtered in three steps. The results from the analysis of the application at each filter step are presented here following the same approach for the entire data set. First, the data were filtered by excluding all pixels where the radar- and satellite-estimated rain intensity was 0.0 mm/h, which means the area the satellite algorithm correctly labelled as receiving no rain. The quantiles of the remaining differences are shown on the left side of Figure 4. An improvement in the range of the quantiles for each temporal integration step can be seen. For the 1-h resolution, the 5% and 95% quantiles span a wider range of 5.5 mm/h than for the unfiltered data of 3.2 mm/h because there are more excluded rainless pixels for higher temporal resolutions (a direct result of small-scale convective rain events). In contrast, there are almost no rainless pixels at lower resolutions, e.g. at 24 h (see Figure 1 and Görner *et al.*, 2011) because of widespread and moving convection events or fronts over longer time spans. Therefore, the range covered by 90% of the differences for the 24-h resolution is the same as for the unfiltered data (1.8 mm/h). The right side of Figure 4 shows the most relevant range (from −1.5 mm/h to 1.5 mm/h) of the related empirical distributions of the relative frequencies of the differences. The peaks at the 0.0 mm/h difference in Figure 4 are omitted by this filter because these peaks were mainly caused by the detection of rainless areas by each algorithm. This result is more distinct for the high temporal resolutions (1 h, 3 h, and 6 h) due to the aforementioned fact that fewer rainless pixels occur at lower temporal resolutions. A bimodal of distribution remains for each resolution, with peaks both at low negative differences (near −0.2 mm/h) and at low positive differences (near 0.2 mm/h). The relative frequencies increase for the negative peak and decrease for the positive peak over the temporal integration. These trends mean that the satellite-based algorithms tend to overestimate the actual rain intensity at 1 h and underestimate it at 24-h resolution. The overestimation is due to the overestimated spatial extent of the rain fields at higher temporal resolutions. This decreases with the temporal integration. However, there is a slight tendency of underestimation for each resolution. This can be seen in the 50% quantile (median), which is at −0.1 mm/h for 1 h and 3 h and −0.2 mm/h for the remainder of the integrations.

The associated statistics for this filtered data set can be found in Table 4. The improved agreement of the satellite-based rain intensity estimates by temporal integration is indicated by a decreasing mean ($\overline{x}$), standard deviation (σ_x), and range ($x_{max} - x_{min}$) of the differences.

In the second step, the data set was filtered to retain only pixels for which the radar- and satellite-based rain intensities were >0.0 mm/h. Hence, only the areas where both systems estimated rain are examined. In Figure 5, the associated quantiles (left) and the relative frequencies (right) of the remaining differences are shown. For the 1-h, 3-h, and 6-h

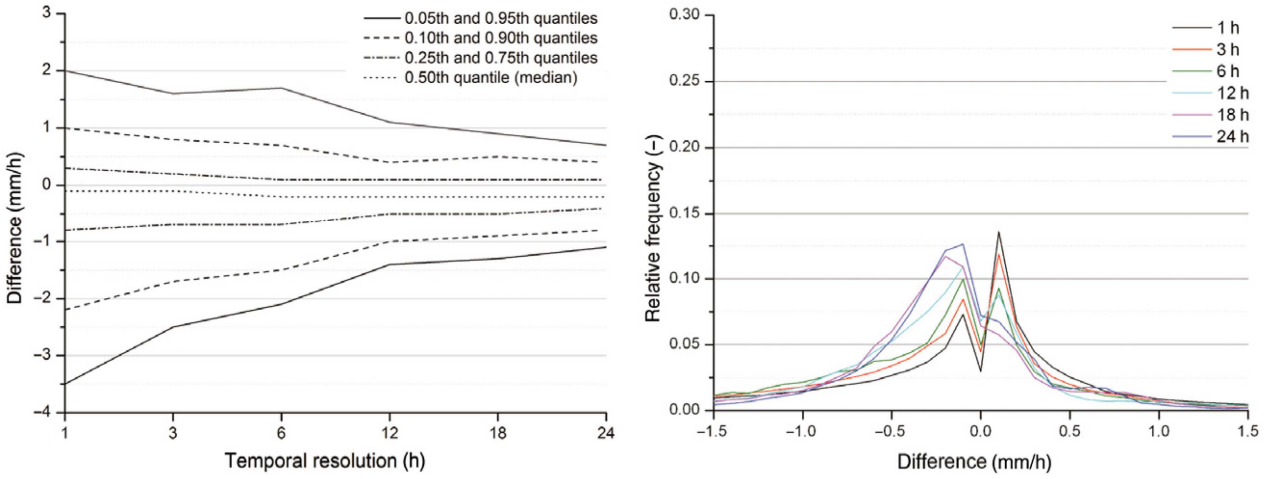

Figure 4 Quantile values (left) and the central range (from –1.5 mm/h to 1.5 mm/h) of the relative frequencies (right) of the differences (mm/h) of the satellite and radar rain intensities for the Auto-Estimator data filtered to remove the pixels with both radar- and satellite-estimated rain intensities of 0.0 mm/h.

Table 4 Statistics of the absolute differences (mm/h) of the satellite and radar rain intensities for the Auto-Estimator data filtered to remove the pixels with both radar- and satellite-estimated rain intensities of 0.0 mm/h

Temporal resolution (h)	Number of values (–)	x_{min} (mm/h)	x_{max} (mm/h)	$\bar{x}$ (mm/h)	σ_x (mm/h)	x_{mod} (mm/h)
1	325 001	−168.4	20.0	−0.33	2.44	0.1
3	360 067	−56.4	12.5	−0.29	1.55	0.1
6	288 003	−18.7	8.3	−0.25	1.19	−0.1
12	273 703	−14.3	5.0	−0.21	0.80	−0.1
18	143 866	−9.2	3.3	−0.20	0.67	−0.2
24	27 166	−7.2	2.6	−0.17	0.59	−0.1

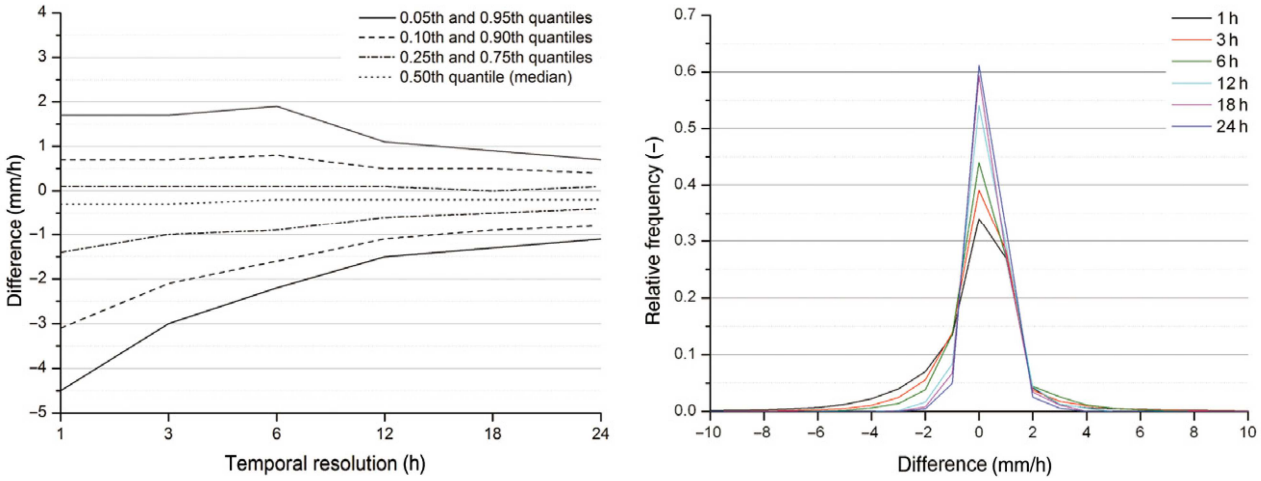

Figure 5 Quantile values (left) and the central range (from −10 mm/h to 10 mm/h) of the relative frequencies (right) of the differences (mm/h) of the satellite and radar rain intensities for the Auto-Estimator data filtered to analyse only the pixels with both radar- and satellite-based rain intensities >0.0 mm/h.

resolutions, the 5% and 95% quantiles span a wider range of 6.2 mm/h, 4.7 mm/h and 4.1 mm/h, compared with the first filter, respectively. For the lower resolutions, the range becomes close to that of the unfiltered data and the data filtered using the first method. This result is caused by the fact that with decreasing temporal resolution, an increasing number of pixels show rainfall (see above). The range is also more negative (up to −4.5 mm/h), which indicates that the satellite-based rain intensities have a larger underestimation than overestimation. This supports the finding that satellite-based rainfall algorithms smooth precipitation fields and tend to overestimate low or zero radar rain intensities and underestimate the high and extreme radar rain intensities. The relative frequencies (Figure 5, right) also show improved agreement with temporal integration for this filtering method. The highest relative frequency is at 0.0 mm/h for each temporal resolution, which increases from 0.34 (1 h) to 0.61 (24 h). Furthermore, over the integration, there is a decrease in the relative frequencies of the negative differences from −6.0 mm/h to −1.0 mm/h. These results are confirmed by the associated statistics in Table 5 that show the same characteristics as described above for Table 4.

Finally, the data were filtered using a third method designed to examine heavy rain intensities with the potential to cause flash floods. For this purpose, only the pixels with a radar-based rain intensity $\geq P_{Wussow}$ (Table 1) were used. For the remaining differences (mm/h), Figure 6 shows the quantiles (left) and the distributions of the relative frequencies (right). Both parts of Figure 6 reveal that heavy rain intensities are underestimated by the satellite-based algorithm for each temporal resolution. The underestimation is very large for the two highest temporal resolutions. This underestimation is indicated by the peaks of the relative frequencies of the differences at −17 mm/h (1 h) and −9 mm/h (3 h) and by the range covered by 90% of the differences of 39.7 mm/h (1 h) and 29 mm/h (3 h).

The range between the $x_{5\%}$ and the $x_{95\%}$ percentiles decreases with each integration step, and it spans only 3.8 mm/h at the lowest time resolution (24 h). The greatest improvement in the quantiles is observed for the temporal integration step from 3 h to 6 h. However, the greatest improvement for the peaks of the relative frequencies is observed for the integration from 1 h to 3 h. This discrepancy is caused by the fact that for the integration from 1 h to

Table 5 Statistics of the absolute differences (mm/h) of the satellite and radar rain intensities for the Auto-Estimator data filtered to analyse only the pixels with both radar- and satellite-based rain intensities > 0.0 mm/h

Temporal resolution (h)	Number of values (–)	x_{min} (mm/h)	x_{max} (mm/h)	$\bar{x}$ (mm/h)	σ_x (mm/h)	x_{mod} (mm/h)
1	125 358	–166.7	20.0	–0.80	3.03	0.0
3	211 047	–56.4	12.5	–0.47	1.79	0.0
6	207 584	–18.7	8.3	–0.31	1.29	0.0
12	235 597	–14.3	5.0	–0.23	0.83	0.0
18	136 725	–9.2	3.3	–0.21	0.68	–0.2
24	26 652	–7.2	2.6	–0.17	0.59	–0.1

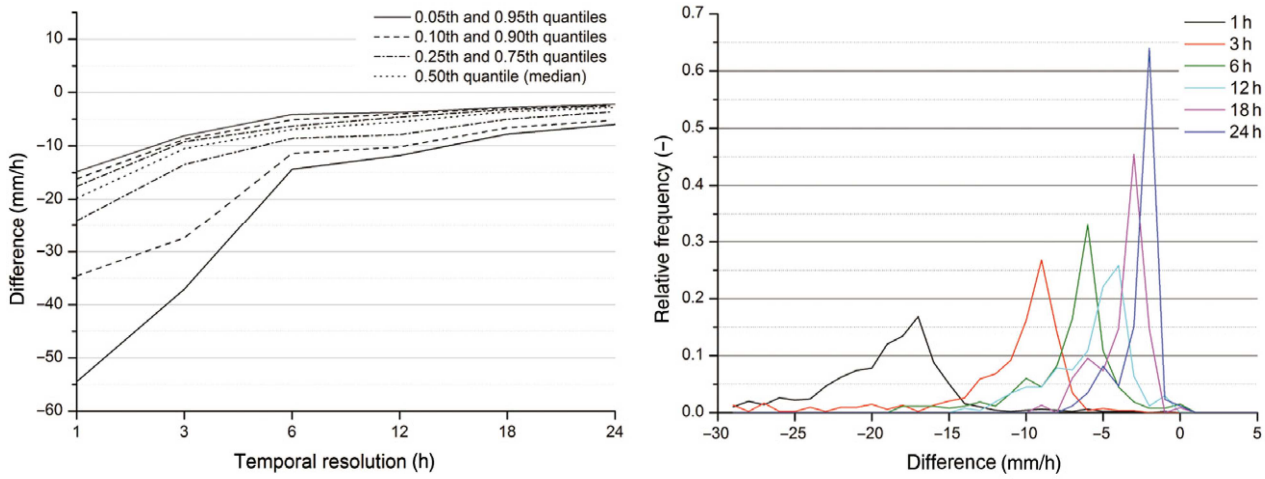

Figure 6 Quantile values (left) and the central range (from –30 mm/h to 5 mm/h) of the relative frequencies (right) of the differences (mm/h) of the satellite and radar rain intensities for the AE with only the pixels containing a radar rain intensity $\geq P_{Wussow}$.

Table 6 Statistics of the absolute differences (mm/h) of the satellite and radar rain intensities for the Auto-Estimator with only the pixels containing a radar rain intensity $\geq P_{Wussow}$

Temporal resolution (h)	Number of values (–)	x_{min} (mm/h)	x_{max} (mm/h)	$\bar{x}$ (mm/h)	σ_x (mm/h)	x_{mod} (mm/h)
1	588	–168.4	–1.1	–24.94	18.58	17.6
3	590	–56.4	–3.5	–13.93	8.99	–9.2
6	267	–18.7	–0.3	–7.7	3.05	–6.8
12	267	–14.3	–1.1	–6.35	2.53	–5.2
18	231	–9.2	–0.8	–4.27	1.58	–3.1
24	86	–7.2	–0.7	–3.20	1.17	–2.6

3 h, the underestimation decreases strongly (see relative frequency peaks), but extreme rain intensities of up to 57.1 mm/h (≙171.3 mm/3 h) are strongly underestimated by the satellite-based algorithm, which reports rain intensities only up to 7 mm/h (≙21 mm/3 h).

The large underestimation arises partly because the AE has a fixed upper limit intensity of 72.0 mm/h for the 1-h resolution, and for the integration from 3 h to 6 h, the total number of values decreases from 590 to 267 (Table 6). Additionally, at the 6-h level, the largest intensities reach a maximum of 18.8 mm/h (≙112.8 mm/6 h), while the satellite-based algorithm delivers rain intensities of up to 6.6 mm/h (≙39.6 mm/6 h) because of the overall lower differences with increasing temporal integration. There are two causes of this result. First, assuming a block rain as mentioned in section 'Methods', the mean minimum rain intensity per hour P_{mean} (mm/h) that defines heavy rainfall is decreasing for increasing rain event durations D (see Table 1). Second, the large hourly underestimation of the radar intensities by the satellite can be compensated for during the course of 1 day and by the summing up of hourly intensities. Therefore, the distributions of the relative frequencies show an increased (from 0.17 to 0.64) and narrowed peak shifting from approximately –17.0 mm/h (1 h)

to approximately −2.0 mm/h (24 h). This behaviour and the explanation for it are also confirmed by the statistics in Table 6 that show a strongly decreasing span, mean, and standard deviation of the remaining differences.

The smaller improvements in the percentile range, the distribution of the relative frequencies, and the statistics for the integration levels > 12 h, especially for the step from 18 h to 24 h, can again be traced back to the use of running rainfall totals for the temporal resolutions from 3 h to 18 h. Thus, the sample size per day is greatly reduced from the 18-h resolution (22 400) to the 24-h resolution (3200). These smaller improvements and the reduction in sample size can be seen in each filtered and unfiltered data set.

Consistent with the results from Part I, the AE and the KM delivered the best results of the four tested algorithms. However, these two algorithms still have deficiencies in correctly detecting the amount and location of radar rain intensities. Despite these limitations, this work provides some support for the use of these algorithms as the basis for the Satellite Application Facility's Convective Rainfall Rate product (Vicente, 2001; AEMET, 2011).

Effects of temporal integration

The results presented here show that each temporal integration step leads to increased agreement in the evaluation scores as well as for the analysed statistical differences. This is most distinct for heavy rain intensities. Therefore, the best results are achieved for the lowest resolution tested (24 h). However, this resolution is not suitable for assessing flood risks for convective rainfall events in mid-latitude regions because of their short time scales and high intensities. Higher resolutions (1 h and 3 h) would be suitable for such rain events, but the rainfall algorithms performed poorly in reproducing both the rainfall intensities and the spatial extent of the rainfall. This is highlighted by the fact that in the mid-latitudes satellite-based rain intensities are mostly used for climatological purposes such as daily or monthly rainfall totals and means (e.g. the data sets provided by the Geostationary Satellite Precipitation Data Center of the Global Precipitation Climatology Project).

In addition, the present study shows that satellite-based rainfall algorithms smooth out the rain intensities by a general underestimation of high-rain intensities and a partial overestimation of lower rain intensities. Other studies have also reported this finding (Negri and Adler, 1993; Scofield and Kuligowski, 2003; Görner *et al.*, 2011).

Summary and conclusions

Some aspects of the general weakness associated with satellite-based rainfall estimates for flash flood-relevant rain intensities have already been described in Part I (Görner *et al.*, 2011).

This includes the difficulties in correct geo-referencing of the satellite data, the weak relation between temperatures and reflectances of cloud tops and rainfall reaching the surface, the specific rainfall characteristics in mid-latitude regions, and the fact that the applied algorithms were not developed for MSG or the mid-latitudes (except the ECST). In Part I, specific measures for reducing these uncertainties were also described. These measures contain the combination of data from different systems, inclusion of additional data such as wind and orography, and the customisation of the algorithms for specific target regions and satellite data sets.

This study examined the ability of four satellite-based rainfall estimates to detect and monitor flood-related heavy rainfall events in the mid-latitudes by means of highly resolved MSG-1 data. Nine high-rainfall days over a flood prone region in the low mountain ranges of Saxony (Germany) were investigated. The analysis compared satellite with radar rain intensities for six temporal resolutions and three different types of data filtering to investigate the applicability of these satellite algorithms and satellite-derived rainfall intensities for flood risk management.

The main conclusions of this work are summarised below:

1. Temporal integration leads to improved agreement between satellite-based rain intensity estimates and radar-based rain intensities, especially concerning heavy, possible flood-triggering events. However, integration causes a loss of temporal information and reduces the ability of the satellite estimates to assess spatio-temporal rainfall distributions and related flood risks, especially for short-time scale rain events.
2. Satellite-based rainfall estimates are best used at lower temporal resolutions, as they show the best agreement with radar estimates at higher temporal integration.
3. Good agreement among the evaluation scores is only achieved at low temporal resolutions of at least 12 h. This is longer than the typical short-duration convective rain events in the mid-latitudes that are associated with flash flooding risk.
4. For higher temporal resolutions of 1 h or 3 h, which are necessary for the nowcasting of heavy convective and flash-flood-related rainfall events, the results demonstrate that the use of satellite-based precipitation estimates is inappropriate.
5. Current satellite rainfall algorithms smooth the precipitation field by underestimating high-rain intensities and by overestimating low-rain intensities (Görner *et al.*, 2011). The algorithms also suffer because fixed rain intensities are used for upper limits.
6. The AE and the KM delivered the best results for both rain intensities and spatial distributions over all temporal integration steps.

Rain intensities and rain areas derived from passively measured satellite data are currently not suitable for applications in flood risk management for small-scale (flash) flood-prone, low-range mountains in the mid-latitudes. However, these data may be useful as an indicator of large rainfall totals over periods of 12 h to several days or when rain gauge and radar data are missing and the size of the catchment is large (Görner *et al.*, 2011).

There are at least two options to improve the suitability of satellite-based rainfall estimates. On the one hand, resulting from the findings of this study, it appears possible to derive statistically sound correction factors for extreme rainfall intensities. These factors would consider the degree of satellite underestimation of intensive rainfall and its related probability so that the corrected satellite rain intensities would agree with the radar-estimated rain intensities. On the other hand, it seems necessary to revisit the algorithms and to start with first principles to develop algorithms suitable to the specific rainfall characteristics in mid-latitude regions. However, the challenge is large due to the complexity of mid-latitude rainfalls, as advective and convective rain events can occur simultaneously. Also, additional effects of orography and wind are difficult to assess.

Such further work is recommended for satellite data application to (extreme) rainfall climatology regardless of its use for flood risk management. Such studies become increasingly feasible as the sample size of extreme events covered by satellite and radar is continuously increasing.

Acknowledgements

This study was supported by the European Community's Sixth Framework Programme through the Integrated Project FLOOD*site*, Contract GOCE-CT-2004–505420. The authors wish to thank the German Weather Service (DWD) for providing the radar data and the European Organisation for the Exploitation of Meteorological Satellites Data Centre for providing the raw satellite data.

References

AEMET. Algorithm theoretical basis document for 'Convective Rainfall Rate' (CRR-PGE05 v3.1). Agencia Estatal de Meteorologia (AEMET), The Eumetsat Network of Satellite Application Facilities, NWC SAF – Support to Nowcasting and Very Short Range Forcasting, Code: SAF/NWC/CDOP/INM/SCI/ATBD/05, 37 pp, 2011. Available at http://www.nwcsaf.org/indexScientificDocumentation.html (accessed 19 August 2011).

Anquetin S., Braud I., Vannier O., Viallet P., Boudevillain B., Creutin J.-D. & Manus C. Sensitivity of the hydrological response to the variability of rainfall fields and soils for the Gard 2002 flash-flood event. *J Hydrol* 2010, **394**, (1–2), 134–147.

Ba M.B. & Gruber A. Goes multispectral rainfall algorithm (GMRA). *J Appl Meteorol* 2001, **40**, 1500–1514.

Bartels H. Projekt RADOLAN. Routineverfahren zur Online-Aneichung der Radarniederschlagsdaten mit Hilfe von automatischen Bodenniederschlagsstationen (Ombrometer). Projekt-Abschlußbericht, 2004. Available at http://www.dwd.de/RADOLAN (accessed 30 May 2011).

Borga M., Creutin J.-D., Gaume E., Martina M., Todini E. & Thielen J. Flash flood risk management: advances in hydrological forecasting and warning. In: P. Samuels, S. Huntington, W. Allsop & J. Harrop, eds. *Flood risk management – research and practice*. London: Taylor & Francis Group, 2009, 1305–1314.

Borga M., Gaume E., Creutin J.-D. & Marchi L. Surveying flash floods: gauging the ungauged extremes. *Hydrol Process* 2008, **22**, (18), 3883–3885.

Collier C. Flash flood forecasting: what are the limits of predictability? *Q J R Meteorol Soc* 2007, **133**, (622A), 3–23.

Franke J. & Bernhofer C. A method for deriving a future temporal spectrum of heavy precipitation on the basis of weather patterns in low mountain ranges. *Meteorol Appl* 2009, **16**, 513–522.

Görner C., Jatho N. & Bernhofer C. Applicability of satellite-based rainfall algorithms to estimate flood related rainfall events in the mid-latitudes – part I: spatial integration. *J Flood Risk Manage* 2011, **4**, (3), 176–188.

Houze R.A. *Cloud dynamics*. Vol. 53 of International Geophysics Series, San Diego, CA: Academic Press, 1993, 573 pp.

Houze R.A. Stratiform precipitation in regions of convection: a meteorological paradox? *Bull Am Meteorol Soc* 1997, **78**, (10), 2179–2196.

IPCC. *Climate change 2007 – the physical science basis: contribution of working group I to the Fourth Assessment Report of the Intergovernmental Panel on Climate Change (IPCC)*. Cambridge, UK: Cambridge University Press, 2007, 996 pp.

Kurino T. A rainfall estimation with the GMS-5 infrared split-window and water vapour measurements. Meteorological Satellite Centre, Technical Note, No. 33, 1997a, 91–101.

Kurino T. A satellite infrared technique for estimating 'deep/shallow' convective and stratiform precipitation. *Adv Space Res* 1997b, **19**, 511–514.

Levizzani V., Amorati R. & Meneguzzo F. A review of satellite-based rainfall estimation methods. European Commission Project MUSIC Report (EVK1-CT-2000-00058), 2002.

Marchi L., Borga M., Preciso E. & Gaume E. Characterisation of selected extreme flash floods in Europe and implications for flood risk management. *J Hydrol* 2010, **394**, (1–2), 118–133.

Munich Re Group. *Weather catastrophes and climate change – is there still hope for us?* München, Germany: Münchener Rückversicherung-Gesellschaft, 2005.

Negri A.J. & Adler R.F. An intercomparison of three satellite infrared rainfall techniques over Japan and surrounding waters. *J Appl Meteorol* 1993, **32**, 357–373.

Petty G.W. The status of satellite-based rainfall estimation over land. *Remote Sens Environ* 1995, **51**, 125–137.

Reudenbach C. Konvektive Sommerniederschläge in Mitteleuropa. Bonner Geographische Abhandlungen, Heft 109, Asgard-Verlag Sankt Augustin, 2003.

Roebeling R.A. & Holleman I. SEVIRI rainfall retrieval and validation using weather radar observations. *J Geophys Res* 2009, **114**, D12102. DOI:10/1029/2009JD012102

Sangati M., Borga M., Rabuffetti D. & Bechini R. Influence of rainfall and soil properties spatial aggregation on extreme flash flood response modelling: an evaluation based on the Sesia river basin, North Western Italy. *Adv Water Resour* 2009, **32**, (7), 1090–1106.

Schmetz J., Pili P., Tjemkes S.A., Just D., Kerkmann J., Rota S. & Ratier A. An introduction to Meteosat Second Generation (MSG). *Bull Am Meteorol Soc* 2002, **83**, (7), 977–992.

Scofield R.A. & Kuligowski R.J. Status and outlook of operational satellite precipitation algorithms for extreme-precipitation events. *Wea Forecast* 2003, **18**, 1037–1051.

SMUL. Klimawandel in Sachsen – Sachstand und Ausblick 2005. Sächsisches Staatsministerium für Umwelt und Landwirtschaft, 2005, 109 pp.

Thies B. A novel day/night technique for area-wide precipitation retrieval over Central Europe using MSG SEVIRI data. Dissertation, Fachbereich Geographie, Philipps-Universität Marburg, 176pp, 2008. Available at http://archiv.ub.uni-marburg.de/diss/z2008/0906/ (accessed 24 August 2011).

Thies B., Nauss T. & Bendix J. Discriminating raining from non-raining cloud areas at mid-latitudes using Meteosat Second Generation SEVIRI night-time data. *Meteorol Appl* 2008, **15**, 219–230.

Vicente G.A. Satellite rainfall estimation for flash flood application – European basic auto estimator within the frame of the SAFNWC. Visiting Scientist's Report, Maryland, 30 January 2001. Available at http://nwcsaf.inm.es./VSA/Vicente.pdf

Vicente G.A., Scofield R.A. & Menzel W.P. The operational GOES infrared estimation technique. *Bull Am Meteorol Soc* 1998, **79**, (9), 1883–1898.

Wilks D.S. *Statistical methods in the atmospheric sciences*, 2nd edn. International Geophysics Series 91. Amsterdam: Academic Press, Elsevier, 2006, 627 pp.

Wussow G. Untere Grenzwerte dichter Regenfälle. *Meteorol Z* 1922, **39**, 173–178.

Appendix C

Peer-reviewed publication 3

Multivariate non-parametric Euclidean distance model for hourly disaggregation of daily climate data

Christina Görner, Johannes Franke, Rico Kronenberg, Olaf Hellmuth & Christian Bernhofer

Theoretical and Applied Climatology

ISSN 0177-798X
Volume 143
Combined 1-2

Theor Appl Climatol (2021) 143:241-265
DOI 10.1007/s00704-020-03426-7

Springer

Theoretical and Applied Climatology (2021) 143:241–265
https://doi.org/10.1007/s00704-020-03426-7

ORIGINAL PAPER

Multivariate non-parametric Euclidean distance model for hourly disaggregation of daily climate data

Christina Görner[1] · Johannes Franke[2] · Rico Kronenberg[1] · Olaf Hellmuth[3] · Christian Bernhofer[1]

Received: 17 November 2017 / Accepted: 4 October 2020 / Published online: 15 October 2020

Abstract
The algorithm for and results of a newly developed multivariate non-parametric model, the Euclidean distance model (EDM), for the hourly disaggregation of daily climate data are presented here. The EDM is a resampling method based on the assumption that the day to be disaggregated has already occurred once in the past. The Euclidean distance (ED) serves as a measure of similarity to select the most similar day from historical records. EDM is designed to disaggregate daily means/sums of several climate elements at once, here temperature (*T*), precipitation (*P*), sunshine duration (*SD*), relative humidity (*rH*), and wind speed (*WS*), while conserving physical consistency over all disaggregated elements. Since weather conditions and hence the diurnal cycles of climate elements depend on the weather pattern, a selection approach including objective weather patterns (OWP) was developed. The OWP serve as an additional criterion to filter the most similar day. For a case study, EDM was applied to the daily climate data of the stations Dresden and Fichtelberg (Saxony, Germany). The EDM results agree well with the observed data, maintaining their statistics. Hourly results fit better for climate elements with homogenous diurnal cycles, e.g., *T* with very high correlations of up to 0.99. In contrast, the hourly results of the *SD* and the *WS* provide correlations up to 0.79. EDM tends to overestimate heavy precipitation rates, e.g., by up to 15% for Dresden and 26% for Fichtelberg, potentially due to, e.g., the smaller data pool for such events, and the equal-weighted impact of *P* in the *ED* calculation. The OWPs lead to somewhat improved results for all climate elements in terms of similar climate conditions of the basic stations. Finally, the performance of EDM is compared with the disaggregation tool *MELODIST* (Förster et al. 2015). Both tools deliver comparable and well corresponding results. All analyses of the generated hourly data show that EDM is a very robust and flexible model that can be applied to any climate station. Since EDM can disaggregate daily data of climate projections, future research should address whether the model is capable to respect and (re)produce future climate trends. Further, possible improvements by including the flow direction and future *OWP*s should be investigated, also with regard to reduce the overestimation of heavy rainfall rates.

1 Introduction

Climate data with high temporal resolution are needed in a multitude of hydrological models (e.g., *WaSim-ETH*, *MIKE FLOOD*) or ecological models (e.g., *SWAT-CN*, *GASFLUX*) and for climate research and analysis. Additionally, the investigation of climate-related extremes and the changes in climate statistics are an important and relevant topic of research.

A common problem is that often only daily observations are available with sufficient spatial resolutions and sufficiently long time series since hourly measurements are more difficult, expensive, and high-maintenance. Hence, hourly time series are often not available and do not have appropriate lengths or contain gaps due to failures of the measuring equipment. To adapt to this lack of data, there are several methods to generate, complete, or extend the hourly time series of different climate elements. However, most of them are designed for the disaggregation of only one or two climate elements focusing on the disaggregation of precipitation as in e.g., Glasbey et al. (1995), Güntner et al. (2001), Lisniak et al. (2013), Lee and Jeong (2014), and Lu et al. (2015). Only a few models have been developed for the disaggregation of more than one climate element, such as in Debele et al. (2007), Mezghani and Hingray (2009), or Kim et al. (2016). These disaggregate daily

✉ Christina Görner
christina.goerner@tu-dresden.de

[1] Institute of Hydrology and Meteorology, Technische Universität Dresden, Tharandt, Germany

[2] Department of Climate, Air, Noise and Radiation, Saxon State Office for Environment, Agriculture and Geology, Dresden, Germany

[3] TROPOS Leibniz Institute for Tropospheric Research, Leipzig, Germany

temperature data among others. Temperature is the second most disaggregated climate element.

All disaggregation approaches are based either on parametric or non-parametric methods. For example, the method of Lisniak et al. (2013) is a parametric one for the temporal disaggregation of daily data based on multiplicative random cascades (MRC) as described by Olsson (1998) and Güntner et al. (2001). The method of Kim et al. (2016) is also a parametric one for statistical downscaling based on generalized linear modeling (GLM), as described in McCullagh and Nelder (1989). Beck and Bárdossy (2013) developed an indirect downscaling method based on a fuzzy logical classification and Bárdossy (1998) used simulated annealing for the simulation of precipitation time series. Examples of nonparametric approaches include the methods of Mezghani and Hingray (2009), Sharif et al. (2013), Lee and Jeong (2014), and Lu et al. (2015). These three stochastic approaches are based on K-nearest neighbor resampling (*KNR*).

The Euclidean distance model (EDM) presented here is also based on a non-parametric resampling method. It is able to disaggregate daily mean/sum values of temperature, precipitation, sunshine duration, relative humidity, and wind speed, filling the need for a model that generates hourly data for a combination of climate elements and with a physical consistency over all disaggregated climate elements.

The EDM differs from the KNR mainly in the kind of a priori information considered in the classification of the object of interest into preexisting classes. The KNR is based on (i) a suitable distance metrics (e.g., Euclidean distance, Manhattan distance, Mahalanobis distance) and on (ii) the consideration of the total number of objects that have been divided into classes. Hence, besides the distance measure in the feature space, also, the a priori probability with which an object can be expected in one of the preassigned classes is considered. This is quite similar to a maximum likelihood approach. However, for classes with only a small number of objects, the signal-to-noise ratio and with it the goodness of classification can decrease. This may happen, especially, when the underlying data are not equally distributed or the sample size of the data is too small. Similar to KNR, also, the EDM considers a priori information in the disaggregation process, but here in a kind of memorization of historically similar events, known as the method of analogous cases.

The EDM is based on the assumption that the day to be disaggregated (hereafter called disaggregation day) has occurred at least once in the past with more or less the same weather conditions. In the EDM approach, the minimum distance serves as the pointer to the most similar day in the historical data set. As disaggregation is an under-determined task, observations, physical model assumptions, and arguments of plausibility are required for its solution. The choice of the distance metrics is arbitrary to some degree. Due to a lack of sufficient a priori information required for the determination of more sophisticated metrics (e.g., employing covariance matrices), the Euclidean distance is used as a sufficiently simple and robust distance measure for the present purposes. The consideration of the method of analogous cases has the important advantage of reducing the degrees of freedom in the disaggregation procedure by including direct observations.

Since the EDM works without any calibration or preassigned classifications, it disaggregates each single day independently and flexible, and potential changes in the classifications and climate variations are no limitation for the EDM. Further, it is a location-independent model that can be applied to any other region or station. Only observed hourly and corresponding daily data are required. And also, daily values outside the observed range of cases can therefore be disaggregated since only a diurnal cycle of the past is transferred and due to applied quotients, the daily values are conserved. But if there are not yet observed characteristics of diurnal cycles, e.g., caused by climate change, the EDM is unable to generate this as it always provides more or less a copy of the past.

The structure and functionality of EDM are explained here. And its performance is examined by means of the data sets recorded at the two climate stations Dresden and Fichtelberg over the period 1995–2014. Both stations are located in the Free State of Saxony (Germany). Dresden is a lowland station, and Fichtelberg is a mountain station with a more extreme climate. Finally, the EDM is compared to the functionality and performance of the disaggregation tool MELODIST of Förster et al. (2016).

2 Material

2.1 Case-study region

The Free State of Saxony serves as the case-study region for this work. Saxony is a federal state within Germany, covering approximately 18,400 km^2 between 11.9°–15.0° E and 50.2°–51.7° N. Its topography is flat in the North and West, with low-range mountains in the South. The Ore Mountains (Erzgebirge) peak at the Fichtelberg, with heights of up to 1200 m a.s.l. Figure 1 shows the geographical locations as well as the topography of Saxony.

Saxony lies in the westerly wind zone of the mid-latitudes and within the transition region between the maritime climate of Western Europe and the continental climate of Eastern Europe. Its climate is dominated by the North Atlantic and the orientation of the low-range mountains due to the governing weather patterns (SMUL 2008).

Due to its climatic characteristics, the SW-NE-oriented Ore Mountains and the effects of climate change, Saxony is prone to heavy rainfall events, especially in mountainous regions with many small and medium catchments and short flood response times (SMUL 2005). The climate change also leads to water

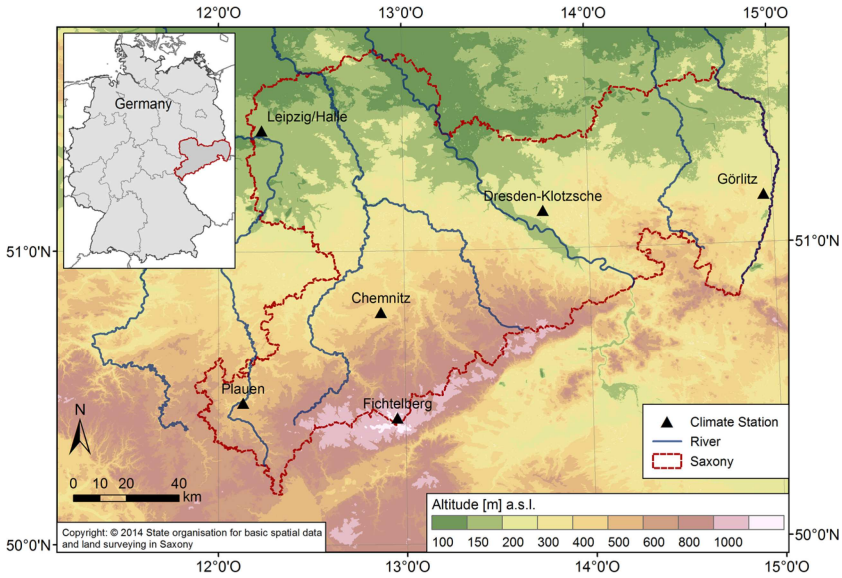

Fig. 1 Geographic location and topography of the Free State of Saxony, including the geographical location of the six selected DWD climate stations

balance changes and related problems concerning water availability, distribution, storage, and usage. Therefore, water balance, flood modeling, and risk management are important fields of research in Saxony. Various models, like rainfall-runoff-models, water balance models, or flood forecasting models, exist for the river catchments in Saxony. The model WAVOS (Burek and Rademacher 2007) is used for the water level forecasting of the River Elbe. To simulate the water balance of the Mulde River catchment, the model ArcEGMO (Pfützner et al. 2007; Schumann 2009) was calibrated. The model WaSiM-ETH (Schulla and Jasper 2007) is used to estimate the water balance of the Weißer Schöps River catchment. In addition, for the rainfall-runoff-modeling of the Große Röder River catchment, the model HBV (Bergström 1992) was adapted. All these models need highly resolved input data of temperature and precipitation. The models *ArcEGMO* and *WaSiM-ETH* need data of global radiation or sunshine duration, wind speed, and vapor pressure or relative humidity.

2.2 Data

2.2.1 Observed climate data

For this study, the six climate stations Chemnitz, Dresden-Klotzsche, Fichtelberg, Görlitz, Leipzig/Halle, and Plauen of the German Weather Service (DWD) were selected as they belong to the same macro-climatic transition zone between the maritime influenced climate in Western Europe and the continental climate in Eastern Europe. Further, they also belong to the same meso-climatic zone as they are close to each other (within a radius of 125 km; Fig. 1) and within one federal state. Due to meso-climatic variations, Kronenberg et al. (2015) classified four regions of similar climates for Saxony. The climate stations used for this study spread over all these four regions. It is recommended to pool only stations of the same climate region, but this would reduce the available climate data significantly, especially concerning hourly recorded data. The consequences of pooling stations of different climate regions are discussed in Section 4.

For the comparison of the EDM with the disaggregation tool *MELODIST* of Förster et al. (2016), the data of the climate station *De Bilt* are used. This station is located in the Utrecht province, Netherlands, about 650 km to the west of Dresden. De Bilt belongs to the maritime influenced macro-climatic zone of Western Europe.

The coordinates and altitudes of all climate stations are listed in Table 1. Figure 1 shows the geographic locations of the Saxon stations. The observed hourly and corresponding daily data of the Saxon climate stations were provided by the DWD and cover the time period between September 1995 and August 2014. The datasets include the mean temperature T_{mean} [°C], precipitation P [mm], sunshine duration SD [min], relative humidity rH [%], and wind speed WS [m/s] at 10 m height. Additionally, the daily data also include the minimum and maximum temperature T_{min} [°C] and T_{max} [°C]. All of the daily data besides the precipitation data refer to 00:00 CET and 23:59 CET, where CET ≙ UTC + 1. The reference time of the daily precipitation data spans between 06:51 CET and 06:50 CET.

The hourly and daily recorded data of De Bilt were provided by the KNMI and cover the period between January 1981 and December 2014. The datasets include the same climate elements as the datasets of the Saxon stations.

A basic requirement of the model performance is the physical consistency between the hourly and the corresponding daily mean/sum data, i.e., the re-aggregation of hourly data should not result in deviations from the observed mean/sum data. To ensure this, the data were corrected for missing values in an initial step. If hourly values were missing in the data records, the corresponding gap in the model input data were

Table 1 Name, geographical location, altitude, mean annual temperature [°C], mean annual precipitation [mm/a], and mean annual sunshine duration [h/a] (1961–1990) of the seven used climate stations

Climate station	Code	Latitude [° N]	Longitude [° E]	Altitude [m a.s.l.]	*T* [°C]	*P* [mm/a]	*SD* [h/a]
Chemnitz	853 (DWD)	50.79	12.87	418	8.6	690	1533
Dresden-Klotzsche	1048 (DWD)	51.13	13.75	222	8.7	735	1659
Fichtelberg	1358 (DWD)	50.43	12.95	1213	2.9	1231	1517
Görlitz	1684 (DWD)	51.16	14.95	238	8.2	722	1718
Leipzig/Halle	2932 (DWD)	51.43	12.24	131	9.1	635	1683
Plauen	3946 (DWD)	50.48	12.13	386	7.5	634	1471
De Bilt	260 (KNMI)	52.10	5.18	2	10.1	887	1602

encoded as −999.0 and the related daily data were hence not used for disaggregation.

2.2.2 Objective weather pattern data

As an additional characteristic, the daily objective weather pattern (OWP) classification of the DWD is used in the present study. It consists of 40 pattern classes encompassing all atmospheric conditions. Each of these classes represents a certain combination of the general flow direction (5 mean flow directions, e.g., northwest), the synoptic flow pattern at two tropospheric pressure levels (four categories: cyclonic/anticyclonic in 950 hPa/500 hPa), as well as the humidity of the atmosphere (two categories: humid/dry), resulting in altogether $5 \times 4 \times 2 = 40$ different OWP classes. For the case study, only the synoptic flow patterns at the two atmospheric pressure levels and the humidity of the atmosphere are used. The mean flow direction was not taken into account, due to very high effort and the lack of a semi-automated procedure to recognize the mean flow direction from weather charts.

The weather pattern is derived once a day at 12:00 CET, covers the territory of Germany and its adjacent regions, and is available since the 1st July 1979. The derivation of this classification is described in detail in Bissolli and Dittmann (2003). The OWP data are freely available online at the website of the *DWD*.

3 Methods

The Euclidean distance (ED) is used as a robust measure of similarity between two individual sets of daily climate data. The aim is to find the most similar analogous reference day, called "basic day" (D_B) from records of historical weather events and to transfer its diurnal cycle to the "disaggregation day" (D_D). The assignment of an actual event to a historical analog is the essence of the method of "analogous case".

First, the structure of the ED model (EDM) is presented schematically in Fig. 2 and outlined below; afterwards, the methods to compare the disaggregated and observed hourly data are described.

3.1 Model structure

3.1.1 Setup of the data base

In the first step, the daily datasets of the basic climate stations and all daily data that have to be disaggregated are imported into EDM. Additionally, for each station, an accompanying dataset containing the time of the sunrise and sunset and the resulting length of the day (*LOD*) for each Julian day of a year is imported as a look-up table.

During the import, each basic day is assigned to each of the three incremental refining weather pattern groups WPG-1, WPG-2, and WPG-3:

- WPG-1: subdivision with different flow patterns in the 950 hPa level (cyclonic/anticyclonic) providing two classes
- WPG-2: subdivision with different flow patterns in the 950 hPa level (WPG-1) and additional humidity of the atmosphere (humid/dry), providing four classes
- WPG-3: subdivision with different flow patterns in the 950 hPa level (WPG-1), humidity of the atmosphere (WPG-2) and additional with different flow patterns in the 500 hPa level (cyclonic/anticyclonic) providing eight classes

To eliminate the units of the climate elements and to achieve a dataset with an arithmetic mean of 0.0 and an empiric standard deviation of 1.0, a Studentization is done for the daily data of each element and over all stations by

$$z_E = \frac{x_E - \bar{x}_E}{\sigma_{x_E}} \quad (1)$$

where z_E is the Studentized daily value of a climate element E, x_E is the daily value to be standardized, $\bar{x}_E$ is the arithmetic mean of the climate element over all basic stations including the station to be disaggregated, and σ_{x_E} is the standard deviation of the element over all basic stations including the station to be disaggregated.

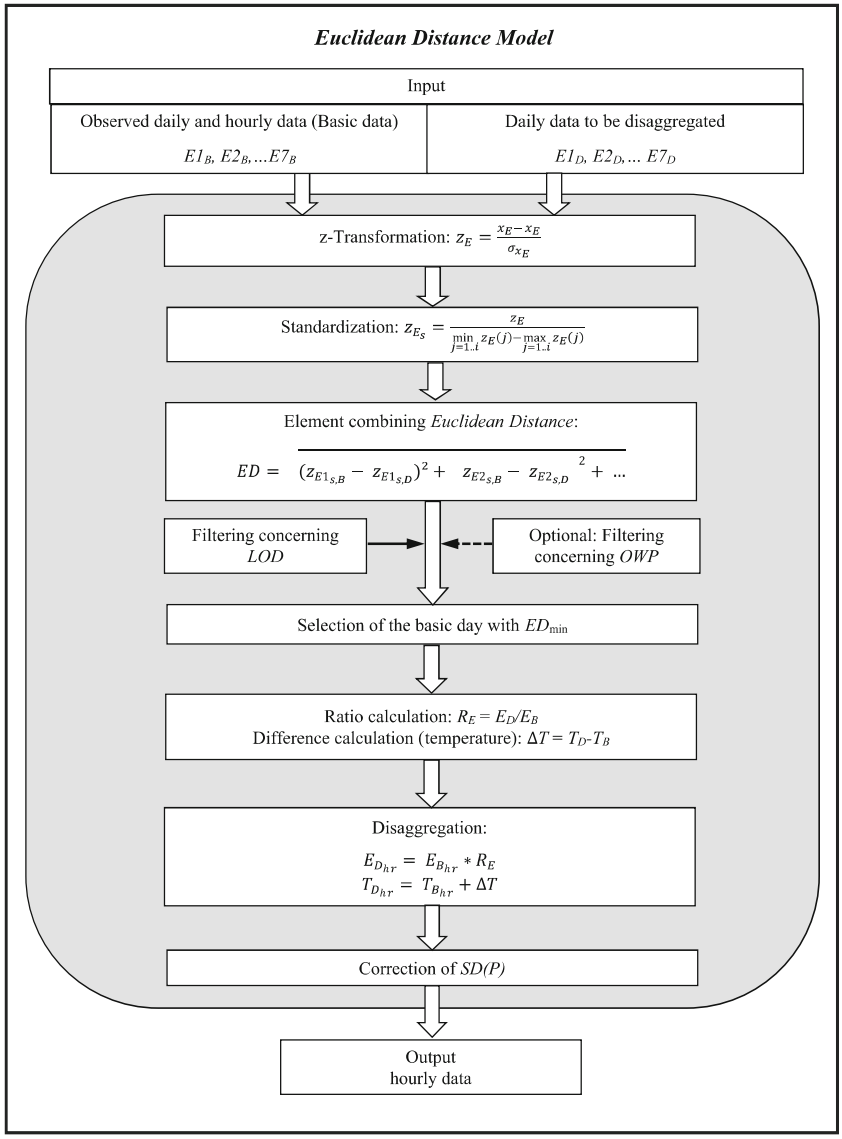

Fig. 2 Flowchart of the Euclidean distance model

The recorded hourly datasets of some climate elements, e.g., precipitation and relative humidity, are not normally distributed and it is not assumed to obtain normality by this Studentization.

Afterwards, to make the climate elements comparable among each other, all Studentized data are standardized by dividing each Studentized daily value, z_E , by the range of all the data:

$$z_{E_s} = \frac{z_E}{\min\limits_{j=1..i} z_E(j) - \max\limits_{j=1..i} z_E(j)} \tag{2}$$

where z_{E_s} is the standardized-Studentized daily value of a climate element E, z_E is the Studentized daily value, and $\min\limits_{j=1..i} z_E(j)$ and $\max\limits_{j=1..i} z_E(j)$ are the minimum and maximum values determined over all climate elements, all stations and all days.

The following steps are carried out separately for each disaggregation day D_D.

3.1.2 Selection of an analogous day

If the data of the station to be disaggregated are within the pool of basic days *DB* (i.e., for validation as shown in Section 4.3), the specific day *DD* is excluded to avoid a disaggregation of a day with its own data. The performance appeared better when the three preceding and the three subsequent days next to *DD* are excluded.

In the first selection step, all basic days D_B in the pool are filtered according to two constraints. If the D_D is a precipitation day with $P > 0.0$ mm, the most similar D_B has to be a precipitation day, too, and if D_D has a sunshine duration > 0.0 h, the most similar D_B has to have a sunshine duration of > 0.0 h, too.

Afterwards, the standardized-Studentized daily data of the selected analogous D_B are used to calculate the similarity metrics *ED* as follows:

$$ED = \sqrt{\left(z_{E1_{s,B}} - z_{E1_{s,D}}\right)^2 + \left(z_{E2_{s,B}} - z_{E2_{s,D}}\right)^2 + \ldots + \left(z_{Ei_{s,B}} - z_{Ei_{s,D}}\right)^2} \quad (3)$$

where z_s is the standardized and Studentized daily value, subscript *E* denotes the climate element, index *i* is the identifier of the climate element (here e.g., *E1* means the maximum temperature), subscript *B* refers to the basic daily data, and subscript *D* to the daily data to be disaggregated.

The *ED* is calculated only for all those filtered D_B that contain no missing values in the data of the climate elements that are used for the *ED* calculation or that have to be disaggregated.

The subsequent selection of the most similar D_B is based on the minimization of *ED* values.

The model performs two different stepwise selection approaches to filter out the most similar day, both comprising five steps.

The first selection approach is stepwise filtering the D_B applying a successively refined *LOD* interval (Selection 1, *S1*):

1. *LOD* ± 2 h of the D_D
2. *LOD* ± 1 h of the D_D
3. *LOD* ± 30 min of the D_D
4. *LOD* ± 15 min of the D_D
5. Same *LOD* of the D_D

If more than one D_B is left after a selection step, the next step is performed. Otherwise, if only 1 day is left, this day is adopted the most similar day and hence, is used as D_B for the disaggregation (D_{BD}). In addition, if no D_B is left after a selection step, the most similar day is selected from all the D_B that were remaining after the prior step. Then, the most similar D_B will be used as D_{BD} and has a minimum distance ($ED_{\min}$).

The second (alternative) selection approach is stepwise filtering the *DB* by applying the successively refined *LOD* (cf. *S1*) and a successively extending *OWP* criteria (Selection 2, *S2*):

1. *LOD* ± 2 h of the D_D and:
   - 1.1. Exact same *WP*
   - 1.2. *WPG-3*
   - 1.3. *WPG-2*
   - 1.4. *WPG-1*
2. *LOD* ± 1 h of the D_D and:
   - 2.1. Exact same *WP*
   - 2.2. *WPG-3*
   - 2.3. *WPG-2*
   - 2.4. *WPG-1*
3. *LOD* ± 30 min of the D_D and:
   - 3.1. Exact same *WP*
   - 3.2. *WPG-3*
   - 3.3. *WPG-2*
4. *LOD* ± 15 min of the D_D and:
   - 4.1. Exact same *WP*
   - 4.2. *WPG-3*
5. Same *LOD* of the D_D and:
   - 5.1. Exact same *WP*
   - 5.2. *WPG-3*

If no D_B is left after a selection step, the next step is performed. If only 1 day is left, this is adopted the most similar day and hence is used as D_B for the disaggregation (D_{BD}). In addition, if more than one D_B is left, the most similar D_B will be used as D_{BD} and has a minimum distance $ED_{\min}$ as written in Eq. 3.

It is possible that there is more than one D_B with $ED_{\min}$, especially when only a few or even only one element is used for the *ED* calculation. In this case, the D_{BD} is selected by means of a uniformly distributed random factor.

3.1.3 Adaptation of the selected hourly meteorological conditions

To ensure self-consistency between aggregated and disaggregated data, an intermediate adjustment step is necessary. Prior to application to D_D, the diurnal cycle of the most similar D_B is rescaled. The rescaling procedure starts with the calculation of the ratios of the daily values of each climate element besides temperature; for temperature, the difference is calculated. These two factors are equal to

$$R_E = \frac{E_D}{E_B} \quad (4)$$

$$\Delta T = T_D - T_B \quad (5)$$

where R_E is the ratio of the climate element *E*, E_D is the daily value of the climate element *E* that has to be disaggregated, E_B is the basic daily value of the climate element *E* of the most similar day (D_{BD}), and ΔT is the difference between the daily mean temperatures of the disaggregation day (T_D) and the most similar basic day (T_B).

With these two metrics, the hitherto unknown hourly values of the disaggregation day are generated by applying them to the known hourly values of the identified analogous D_{BD} as follows:

$$E_{D_{hr}} = E_{B_{hr}} * R_E \quad (6)$$

$$T_{D_{hr}} = T_{B_{hr}} + \Delta T \quad (7)$$

where E_{Dhr} is the generated hourly value of the climate element, E_{Bhr} is the hourly value of the climate element of the D_{BD}, T_{Dhr} is the generated hourly mean temperature, and T_{Bhr} is the hourly mean temperature of the D_{BD}.

Due to multiplication with the scaling R_E, it is formally possible that non-physical hourly sunshine durations of > 60.0 min and relative humidities of > 100.0% are generated. In this case, the sunshine duration is set to 60.0 min and the relative humidity is set to 100.0%.

Daily precipitation and sunshine duration values of 0.0 mm and 0.0 min are not disaggregated. Instead, the related 24 hourly values are set equal to 0.0 mm and 0.0 min, respectively.

If the D_D contains a missing value of a climate element that is not included in the *ED* calculation, the missing value is replaced with 24 hourly missing values for this climate element. However, if this climate element is included in the *ED* calculation, it leads to missing hourly values for all the climate elements.

3.1.4 Treatment of hours with precipitations > 0 mm and 60 min of sunshine

Disaggregation might result in simultaneous co-occurrence of rain events and clear-sky conditions in the hourly data. Of course, rain and sunshine might be observed simultaneously at characteristic time scales shorter than 1 h, e.g., during convective rainfall events in postfrontal cold airmasses with partial cloud coverage and sunny episodes, particularly in summer (frequently associated with the appearance of rainbows). Unfortunately, the retrieval of such short-term variability from the hourly data the historical records are based on requires the solution of a closure problem, which is even trickier than the disaggregation of hourly data from daily values (as in the present study). While consideration of subscale cloud variability would be a promising task for model refinement, its realization was far beyond the scope of the present analysis. Focusing on the characteristic conditions revealed in records of hourly values, here we make use of the ad hoc assumption that coinciding rain-sunshine events should be excluded, i.e., there is either precipitation or sunshine. The disaggregated hourly data of the sunshine duration are corrected for the related hourly precipitation amounts to avoid a sunshine duration of 60.0 min coinciding with a precipitation value of > 0.0 mm. The applied rescaling algorithm is realized via the following nine steps:

1. Since the reference time intervals of the daily precipitation sum and sunshine duration differ, the recorded data are projected into the same time interval. Auxiliary daily precipitation sums (P_{aux}) are calculated for the time spans from 00:00 CET to 23:59 CET for both the D_{BD} (P_{auxB}) as well as for the D_D (P_{auxD}).

2. The theoretical possible precipitation hours are calculated for D_{BD} and D_D as follows:

$$PPH_B = 24.0\ h\text{–}SD_B \tag{8}$$

$$PPH_D = 24.0\ h\text{–}SD_D \tag{9}$$

with PPH_B as the possible precipitation hours of the basic day, SD_B as the daily sunshine value of the basic day, and PPH_D as the possible precipitation time of D_D and SD_D as the daily sunshine value of D_D.

3. For the D_{BD} and the D_D, averaged daily precipitation intensities are calculated by

$$PI_B = P_{aux_B}/PPH_B \tag{10}$$

$$PI_D = P_{aux_D}/PPH_D \tag{11}$$

with PI_B and PI_D denoting the mean precipitation intensities of the most similar basic and disaggregation day, respectively.

4. Then, a precipitation intensity ratio *PIF* is calculated by dividing the two precipitation intensities:

$$PIF = PI_D/PI_B \tag{12}$$

5. The possible numbers of minutes with precipitation for the hour to be corrected are calculated according to:

$$PPM_B = 60.0\ min\text{–}SD_{B_{hr}} \tag{13}$$

where PPM_B is the possible number of precipitation minutes of the basic hour, and SD_{Bhr} is the sunshine duration of the basic hour.

6. The averaged precipitation intensity of the basic hour PI_{Bhr} is calculated by dividing the precipitation value of the basic hour PI_{Bhr} by PPM_B:

$$PI_{B_{hr}} = P_{B_{hr}}/PPM_B \tag{14}$$

7. The averaged precipitation intensity for the generated hourly precipitation value is obtained by multiplying PI_{Bhr} with the ratio *PIF*:

$$PI_{D_{hr}} = PI_{B_{hr}} * PIF \tag{15}$$

8. Knowing $PI_{D_{hr}}$, the number of precipitation minutes for the generated hourly precipitation value is calculated as follows:

$$PM_D = P_{D_{hr}}/PI_{D_{hr}} \tag{16}$$

where PM_D is the number of precipitation minutes of the generated hour and P_{Dhr} is the generated hourly precipitation amount.

9. Finally, the number of sunshine minutes SM_D for the hour to be corrected results from the difference of 60.0 min and the PM_D as follows:

$$SM_D = 60.0\ \text{min} - PM_D \quad (17)$$

The corrected hourly value of sunshine duration is only accepted if it is smaller than the value calculated by using the ratio (Eq. 6).

After this final data adjustment, the process restarts with the next disaggregation day. When the disaggregation of all days is finished, the model creates an output file containing the disaggregated hourly values for all days and climate elements.

3.2 Comparison of disaggregated and observed hourly data

The disaggregated and observed hourly data are compared by using Taylor diagrams, quantile-quantile plots (Q-Q plot), additional statistical values, and the mean diurnal and annual variations. Since the days without precipitation ($P = 0.0$ mm/d) or measurable sunshine duration ($SD = 0.0$ min) were not disaggregated, they were not included in the comparison.

Taylor diagrams (Taylor 2001) were plotted for the elements T_{mean}, SD, rH, and WS as they allow good simultaneous visual comparison of three statistical measures. Here, the measures of the Pearson correlation coefficient (r), normalized root mean square difference ($RMSD_n$), and normalized standard deviation (σ_n) were used.

For the comparison of the disaggregated and observed hourly precipitation data, Q-Q plots of two variables were chosen. Additionally, the lines for the quantiles of 50%, 75%, 90%, 95% (heavy precipitation), and 99% (extreme precipitation) were added to the plots.

In addition to the values used for the Taylor diagrams and Q-Q plots, the statistical values minimum (x_{min}), maximum (x_{max}), mean ($\tilde{x}$), median (x_{med}), and 95% quantile ($x_{95\%}$) were calculated.

To analyze whether the disaggregated data reproduce the general basic characteristics of the observed data, the mean diurnal and annual variations are compared in three ways. The diurnal variations of the four climate elements T [°C], SD [min], rH [%], and WS [m/s] are compared by calculating the diurnal cycles based on the observed and disaggregated hourly data. In addition, the annual variations of each climate element were compared by means of annual cycles calculated from the aggregated observed and generated monthly data.

To compare the results delivered by the EDM with those of the tool *MELODIST*, the root mean square error (RMSE) was calculated. Further, five major characteristics of hourly precipitation features of the observed and generated data for the stations De Bilt and Dresden were calculated: mean duration of events [h], mean precipitation sum of events [mm], mean duration of dry spells [h], number of events per year, and number of hours with $P > 0.0$ mm per day.

4 Results and discussion

The disaggregated climate data are analyzed for the two climate stations, Dresden and Fichtelberg. Both stations belong to different regions of similar climate after Kronenberg et al. (2015). Dresden is a lowland station and was selected because it has the best data base. Fichtelberg was selected because it is a mountain station with a more extreme climate and it serves hence as a kind of test for the performance of the EDM. The consequences of pooling stations of different climate regions are discussed in this section.

The results for both stations are analyzed for various aspects. The differences concerning whole years, summer and winter half-years, the influence of the stations used as base stations, the effects of the climate elements used, and the mean diurnal and annual variations of the generated data are considered.

4.1 Generated datasets based on five stations

At first, the data for the whole period September 1995–August 2014 are analyzed. These data were generated by using the observed data of five basic stations. In order to prevent a skill overestimation, the data of the station which is subject of disaggregation were not considered in the evaluation of the pool of basis data. This means that the data for the climate station Dresden and Fichtelberg, presented here, are generated without Dresden and Fichtelberg, respectively.

4.1.1 Climate station Dresden

Figure 3 shows the Taylor diagram and the Q-Q plot for climate station Dresden for both selection approaches *S1* and *S2*, respectively. The corresponding statistical values are shown in Table 2. It can be seen that the results of all climate elements show normalized standard deviations close to 1.0 for *S1* as well as for *S2*.

The temperature values of both selections show the best performance with the very high correlations of 0.98 and 0.99 and very low $RMSD_n$ values of 0.19 and 0.15. This results from the homogenous, sinusoidal character of the diurnal cycle of the temperature, which is properly reproduced by EDM. In contrast to temperature, the wind speed has a more stochastic character with larger and irregular diurnal variations. Hence, worse results are provided for the wind speeds with correlations of 0.73 and 0.79 and $RMSD_n$ values of 0.76 and 0.67. The results of the generated sunshine duration are very similar to those of the wind speed. The sunshine duration is strongly correlated with the highly fluctuating cloud cover, i.e., it is also characterized by possible high variations during

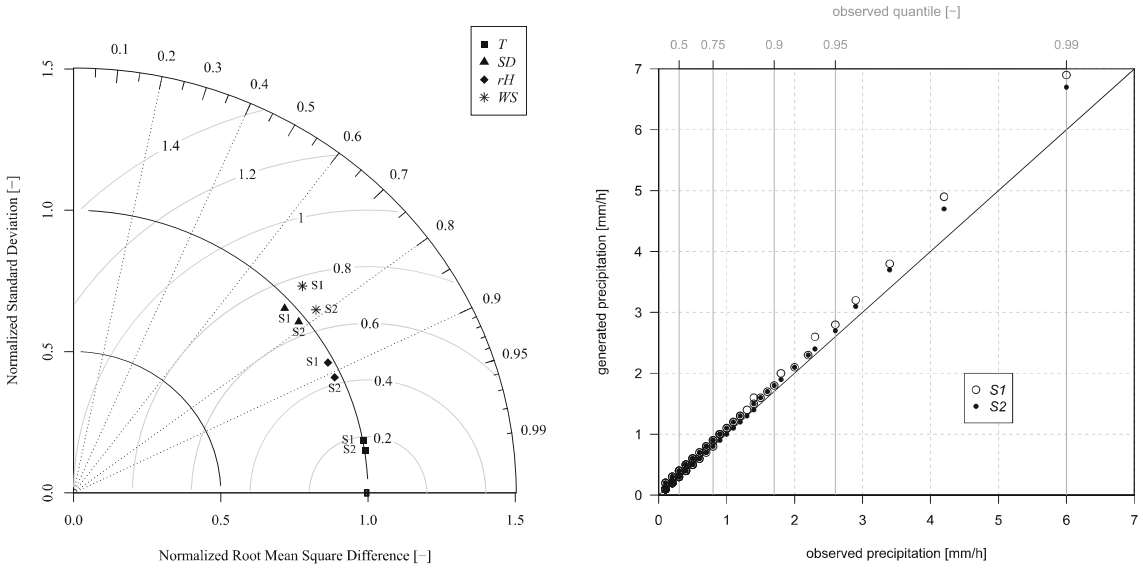

Fig. 3 (left) Normalized root mean square difference [-], normalized standard deviation [-] and correlation [-] of the generated data of *T*, *SD*, *rH*, and *WS* for Selection 1 (*S1*) and Selection 2 (*S2*); (right) the quantiles of the observed and generated precipitation [mm/h] for the climate station Dresden based on five stations

the day. Such variations lead to more frequent and greater differences between the observed and generated hourly values. Since the relative humidity is characterized by a more homogenous diurnal cycle (essentially affected by the course of the temperature), these results reveal higher correlations of 0.88 and 0.91 and lower $RMSD_n$ values of 0.48 and 0.42.

The application of the rescaling procedure according to Section 3.1.3 to hourly *rH* values results in a cut-off of respective 3780 (*S1*) and 2844 (S2) generated hourly values to the maximum possible value of $rH = 100\%$, corresponding to correction rates of 2.3% (*S1*) and 1.6% (*S2*), respectively. Correction of hourly data applies to 783 (11.6%) and 620 (9.2%) disaggregated days, respectively.

Analogously for *SD*, 8917 (*S1*) and 8564 (*S2*) generated hourly values were constrained to the maximum value of 60.0 min, corresponding to correction rates of 11.1% (*S1*) and 10.7% (*S2*). The corrected values affect 1970 (29.2%) and 1856 (27.5%) disaggregated days, respectively.

The correction to exclude co-occurrence of rain events and clear-sky conditions according to Section 3.1.4 applies to 601

Table 2 Statistics of the observed and generated data of the Dresden station based on five stations

Climate element	Sample size	Dataset	x_{min}	x_{max}	$\tilde{x}$	x_{med}	$x_{95\%}$	σ	σ_n	r	$RMSD_n$
T [°C]	162,192	Observed	−20.7	36.7	9.44	9.5	27.8	8.42	-	-	-
		S1	−22.7	37.7	9.44	9.5	28.0	8.44	1.00	0.98	0.19
		S2	−20.6	36.9	9.44	9.5	27.9	8.43	1.00	0.99	0.15
SD [min] *	80,227	Observed	0.0	60.0	23.99	13.0	60.0	25.12	-	-	-
		S1	0.0	60.0	22.99	12.1	60.0	24.37	0.97	0.74	0.71
		S2	0.0	60.0	23.23	12.5	60.0	24.52	0.97	0.78	0.65
rH [%]	162,192	Observed	5.0	100.0	76.17	80.0	100.0	17.19	-	-	-
		S1	2.8	100.0	76.11	79.5	100.0	16.83	0.98	0.88	0.48
		S2	14.3	100.0	76.13	79.6	100.0	16.79	0.98	0.91	0.42
WS [m/s]	162,192	Observed	0.0	20.4	4.18	3.8	10.6	2.15	-	-	-
		S1	0.0	20.5	4.18	3.8	11.1	2.30	1.07	0.73	0.76
		S2	0.0	21.3	4.18	3.8	11.0	2.26	1.07	0.79	0.67
P [mm] **	16,292	Observed	0.1	36.6	0.75	0.3	2.6	1.37	-	-	-
	14,493	*S1*	0.1	48.6	0.83	0.4	2.8	1.58	1.15	-	-
	15,091	*S2*	0.1	48.6	0.80	0.4	2.7	1.41	1.03	-	-

* Excluding night time values and days with $SD = 0.0$ min

** Based on hourly values > 0.0 mm

(*S1*) and 526 (*S2*) generated hourly *SD* values, respectively. These corrections affect 418 (6.2%) and 366 (5.4%) days, respectively. As a result of these two corrections, the calculated daily sums differ from the observed daily values. The maximum differences amount to −4.5 h (*S1*) and −3.4 h (*S2*), but 89.8% (*S1*) and 94.2% (*S2*) of the affected days show only small differences in the range of $-1\ \mathrm{h} < SD \leq 0.0$ h, i.e., of less than 1 h.

In the right panel of Fig. 3, the quantiles of the generated precipitation data are shown. Up to the 96% quantile, the quantiles differ only between 0.1 and 0.3 mm/h. For the quantiles ≥ 96%, representing heavy and extreme precipitation, the differences increase to 0.9 mm/h (*S1*) and 0.7 mm/h (*S2*), and the overestimation amounts to 15% (*S1*) and 12% (*S2*). There are various potential reasons for the overestimation. Both generated datasets contain less hourly values of > 0.0 mm/h (Table 2) which indicates that the EDM tends to generate shorter and less precipitation events (cf. Section 4.7). This results from rounding very small intensities to 0.0 mm/h and from a potential tendency of the EDM to select a day with a shorter precipitation event as the most similar day. The rounding of the disaggregated hourly intensities itself might be a reason for the differences of the observed and disaggregated intensities. Further, in this analysis, precipitation is one of seven equal-weighted climate elements included in the calculation of ED, i.e., precipitation has an impact of 1/7 of the selection of the most similar day. If the impact would be higher, the results are expected to improve for the quantiles. This is examined in Section 4.4. Last but not least, there are supposed to be unintended influences of other variables used in the EDM resampling.

To quantify the magnitude of the overestimation of the quantiles, it was examined whether the overestimation lays within the confidence interval of an extreme value statistics as used for engineering design and flood simulation. For example, the precipitation intensity of 7.0 mm/h corresponds to a return period of 0.2 a, which means such intensities are likely to be observed 5 times per year at the station Dresden. A confidence interval of [5.04 mm/h, 9.15 mm/h] was estimated through fitting of a Gumbel distribution to the hourly data and assuming a critical value of t95.2 = 2.95 from the Student's *t* distribution. The observed difference [0.9 mm/h] of the 0.99-quantile lays therefore within the confidence interval of the fitted extreme value distribution for design rainfall (Fig. 4).

For all elements, Fig. 3 and Table 2 show that the results of *S2* fit better than those of *S1*, but the differences are very small. Hence, including the OWP for the selection of the most similar basic day leads to only weak improvements.

The statistical values contained in Table 2 but not shown in Fig. 3 exhibit high correspondence for all elements besides the minimum of *rH* of *S1* (14.3%) and the maximum *P* of both selections (48.6 mm/h).

4.1.2 Climate station Fichtelberg

The statistics for climate station Fichtelberg (Fig. 5, Table 3) show similar results to those of the climate station Dresden, with normalized standard deviations close to 1.0 for all elements and both selections. The best results, with a correlation of 0.97 and $RMSD_n$ of 0.25, are again obtained for the generated temperature data. The worst results are obtained again for the sunshine duration and the wind speeds with correlations

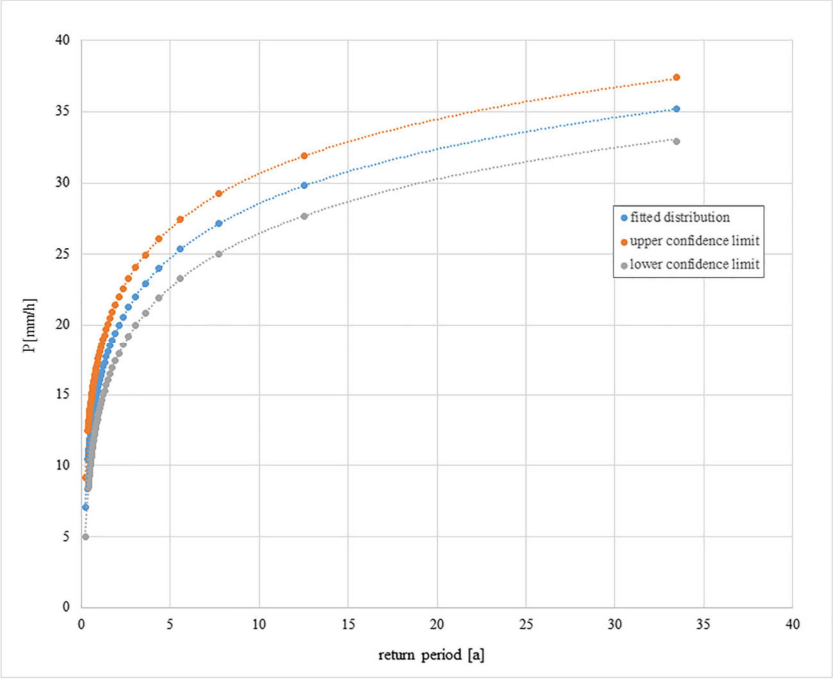

Fig. 4 Confidence interval for the observed precipitation intensities [mm/h] of station Dresden

Table 3 Statistics of the observed and generated data of station Fichtelberg based on five stations

Climate element	Sample size	Dataset	x_{min}	x_{max}	$\tilde{x}$	x_{med}	$x_{95\%}$	σ	σ_n	r	$RMSD_n$
T [°C]	98,969	Observed	−21.9	28.6	4.93	5.4	20.7	7.62	-	-	-
		S1	−23.7	30.0	4.93	5.3	21.7	7.78	1.02	0.97	0.25
		S2	−25.4	30.0	4.93	5.3	22.0	7.83	1.02	0.97	0.25
SD [min] *	50,808	Observed	0.0	60.0	24.44	15.0	60.0	25.04	-	-	-
		S1	0.0	60.0	21.93	8.5	60.0	24.60	0.98	0.68	0.81
		S2	0.0	60.0	22.58	10.0	60.0	24.74	0.98	0.72	0.74
rH [%]	98,969	Observed	5.0	100.0	84.61	93.0	100.0	18.51	-	-	-
		S1	6.9	100.0	83.97	90.2	100.0	18.34	0.99	0.82	0.59
		S2	6.1	100.0	83.74	90.2	100.0	18.41	0.99	0.84	0.57
WS [m/s]	98,969	Observed	0.0	30.1	8.32	7.7	20.5	4.34	-	-	-
		S1	0.0	59.0	8.31	7.5	22.2	4.67	1.08	0.70	0.81
		S2	0.0	45.7	8.32	7.5	22.0	4.69	1.08	0.74	0.76
P [mm] **	11,340	Observed	0.1	32.9	0.79	0.4	2.7	1.39	-	-	-
	10,134	*S1*	0.1	33.1	0.86	0.4	3.0	1.45	1.04	-	-
	9326	*S2*	0.1	26.6	0.93	0.4	3.3	1.58	1.17	-	-

* Excluding night time values and days with $SD = 0.0$ min

** Based on hourly values > 0.0 mm

between 0.68 and 0.74 and $RMSD_n$ between 0.74 and 0.81. The median of the observed *SD* (15.0 min) is highly underestimated by *S1* (8.5 min) and *S2* (10.0 min) (Table 3). The observed maximum wind speed (30.1 m/s) is highly overestimated, with 59.0 m/s and 45.7 m/s. In comparison to the Dresden station, the generated relative humidity data show slightly worse results. These findings point to the influence of meso-climatic variations in the study region, that were not included in the present analysis.

The application of the rescaling procedure according to Section 3.1.2 to hourly *rH* values results in a cut-off of respective 21,916 (*S1*) and 22,528 (S2) generated hourly values to the maximum possible value of $rH = 100\%$, corresponding to correction rates of 22.1% (*S1*) and 22.8% (*S2*), respectively, which is much higher than for the representative low-land station Dresden. Concerning *SD*, 8162 (*S1*) and 8042 (*S2*) generated hourly values were reduced to the maximum value of 60.0 min. This corresponds to correction rates of

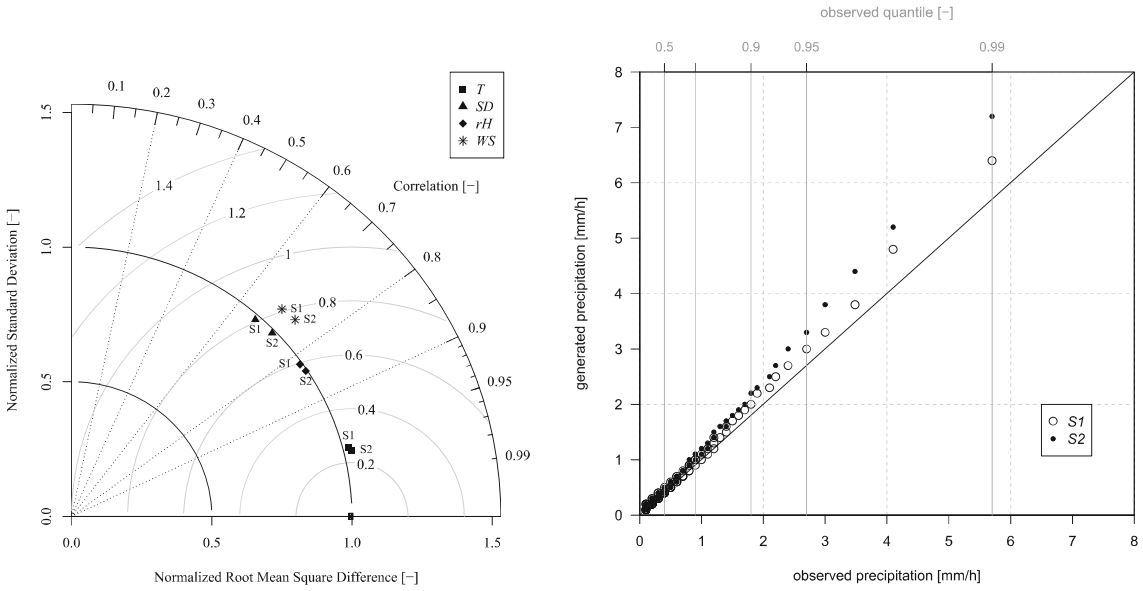

Fig. 5 (left) Normalized root mean square difference [-], normalized standard deviation [-], and correlation [-] of the generated data of *T*, *SD*, *rH*, and *WS* for Selection 1 (*S1*) and Selection 2 (*S2*); (right) the quantiles of the observed and generated precipitation [mm/h] for climate station Fichtelberg based on five stations

16.1% (*S1*) and 15.8% (*S2*). The corrected values affect 1771 (42.9%) and 1615 (39.2%) disaggregated days, respectively.

The correction to exclude co-occurrence of rain events and clear-sky conditions according to Section 3.1.4 applies to 800 (*S1*) and 496 (*S2*) generated hourly *SD* values, respectively. This correction affects 460 (11.2%) and 292 (7.1%) days, respectively. As a result of these two corrections, the calculated daily sums differ from the observed daily values. The maximum differences amount to − 6.6 h (*S1*) and − 7.0 h (*S2*), but 77.1% (*S1*) and 83.7% (*S2*) of the affected days show only small differences in the range of $-1\ \mathrm{h} < SD \leq 0.0$ h, i.e., of less than 1 h.

As for the lowland station Dresden, the inclusion of the *OWP* improves the results slightly.

Concerning the quantiles of the generated precipitation data (Fig. 5 (right))), both selection approaches tend to overestimate, and the *OWP* inclusion leads to even higher overestimations. This is a clear indication of significant mesoscale variability in the study region that segregates the climate conditions at the Fichtelberg station from those of the other five stations. In addition, EDM tends to prefer days with convective precipitation events to reproduce the higher daily precipitations at station Fichtelberg, but this leads to an overestimation of the hourly values. For the quantiles ≥ 93%, the overestimations increase to maxima of 0.7 mm/h (*S1*) and 1.5 mm/h (*S2*), and the overestimation amounts increase to 12% (*S1*) and 26% (*S2*). For potential reasons for the overestimation, compare to the analysis in Section 4.1.1.

4.2 Summer and winter half-years

The generated data of the stations Dresden and Fichtelberg are analyzed separately for the summer and winter half-years based on five climate stations (cf. Section 4.1). The summer half-year covers the 6 months from April to September, and the winter half-year covers the months between October and March. These both half-years are analyzed since they differ in their climatic characteristics. Due to higher global radiation and temperatures, the summer half-year is characterized by more convective and unstable weather patterns while the winter half-year is predominated by more stable weather patterns. This causes different diurnal cycles of the climate elements, especially of precipitation. While convective (heavy) precipitation events tend to short durations of one or only a few hours, stratiform (heavy) precipitation events tend to longer durations of up to a few days.

The results for the climate elements *T*, *SD*, *rH*, and *WG* reveal essentially the same basic characteristics for both, the half-years and the whole year (cf. Section 4.1) for both stations (see Fig. 11 (left) and Fig. 12 (left) and Tables 8, 9, 10, and 11 in the Appendix). The temperature data were found to fit best the wind speed and sunshine data fit worst and those of the relative humidity are in between. The inclusion of the *OWP* leads to small improvements for these five climate elements of both half-years.

The climate elements with homogenous diurnal cycles (*T*, *rH*) are well reproduced for the summer as well as for the winter half-years. In contrast, the climate elements with higher hourly variations (*SD*, *WS*) are less well reproduced in general but perform slightly better for the winter months. This result suggests that the basic assumptions of the disaggregation procedure (e.g., the exclusion of coincidental sunshine and precipitation) are better fulfilled in the wintertime with less scatter in the data caused by convective clouds, turbulence, and unstable weather conditions.

Concerning precipitation, the results differ between Dresden and Fichtelberg. For Dresden, the improved reproductions for the winter half-year also apply to the precipitation data (Fig. 11 (right) in the Appendix), explainable by the lower rain intensities and lower frequency of convective rainfall events during these months. For Fichtelberg, the generated data show overestimations for both half-years, especially for the quantiles ≥ 95% (Fig. 12 (right) in the Appendix). This overestimation is distinct higher for the winter months. For the high daily precipitation sums at station Fichtelberg, the EDM tends to prefer days with convective weather conditions and hence higher precipitation rates per hour. Further potential reasons for the overestimation are given in Section 4.1.1.

The inclusion of the *OWP* leads to small improvements for both half-years at the station Dresden. But at the station Fichtelberg, it worsens the performance of the quantiles of both half-years. This is supposed to be a consequence of the neglect of the meso-climatic variability in the setup of the pool of basic data. While the *OWP* conditions might apply to all included stations, orographic effects might cause differences in the statistical precipitation response from one station to another. As the climate station Fichtelberg, the only mountain station in the pool, was excluded in this analysis from the pool of basis data, the EDM could only select a “most similar event” of a lowland station.

4.3 Data generation based on the full dataset

In this section, it is examined how the results change if the data of all six Saxon basic stations are used, i.e., the stations Dresden and Fichtelberg were included as basic stations, too.

In comparison to the results discussed in Section 4.1.1, the results for station Dresden are at least identical for all five climate elements (see Fig. 13 (top) in the Appendix). This suggests that the basic stations Görlitz, Chemnitz, Leipzig, and Dresden belong more or less to the same mesoclimatetope. Hence, the inclusion of station Dresden as an additional basic station does not lead to a substantial gain in physical information and to an improvement of the overall EDM performance. For all elements, the results of *S2* performs better than those of *S1*, though the differences are small.

In contrast, the inclusion of the station Fichtelberg as a basic station leads to small improvements for the relative humidity, the sunshine duration, and the wind speed for Selection *S1* (Fig. 13 (bottom, left) in the Appendix). The precipitation quantiles of *S2* are overestimated to the same amount as for *S2* as discussed in Section 4.1.2. However, for *S1*, the overestimation increases by 0.2–0.3 mm/h for the quantiles ≥ 90% (Fig. 13 (bottom, right) in the Appendix). Furthermore, the inclusion of the *OWP* leads again to higher overestimations of the quantiles although the station Fichtelberg is included (cf. Section 4.1.2).

4.4 Sensitivity of the distance metrics against the number of considered climate elements

To examine the influence of the climate elements used for the calculation of the *ED*, the disaggregation for the stations Dresden and Fichtelberg was performed by using only the mean temperature and the precipitation amount to calculate the *ED*. These two climate elements were selected as they are the most frequently available observed elements. The statistical results are shown in Fig. 6. Since the relative humidity, the sunshine duration, and the wind speed were not used for

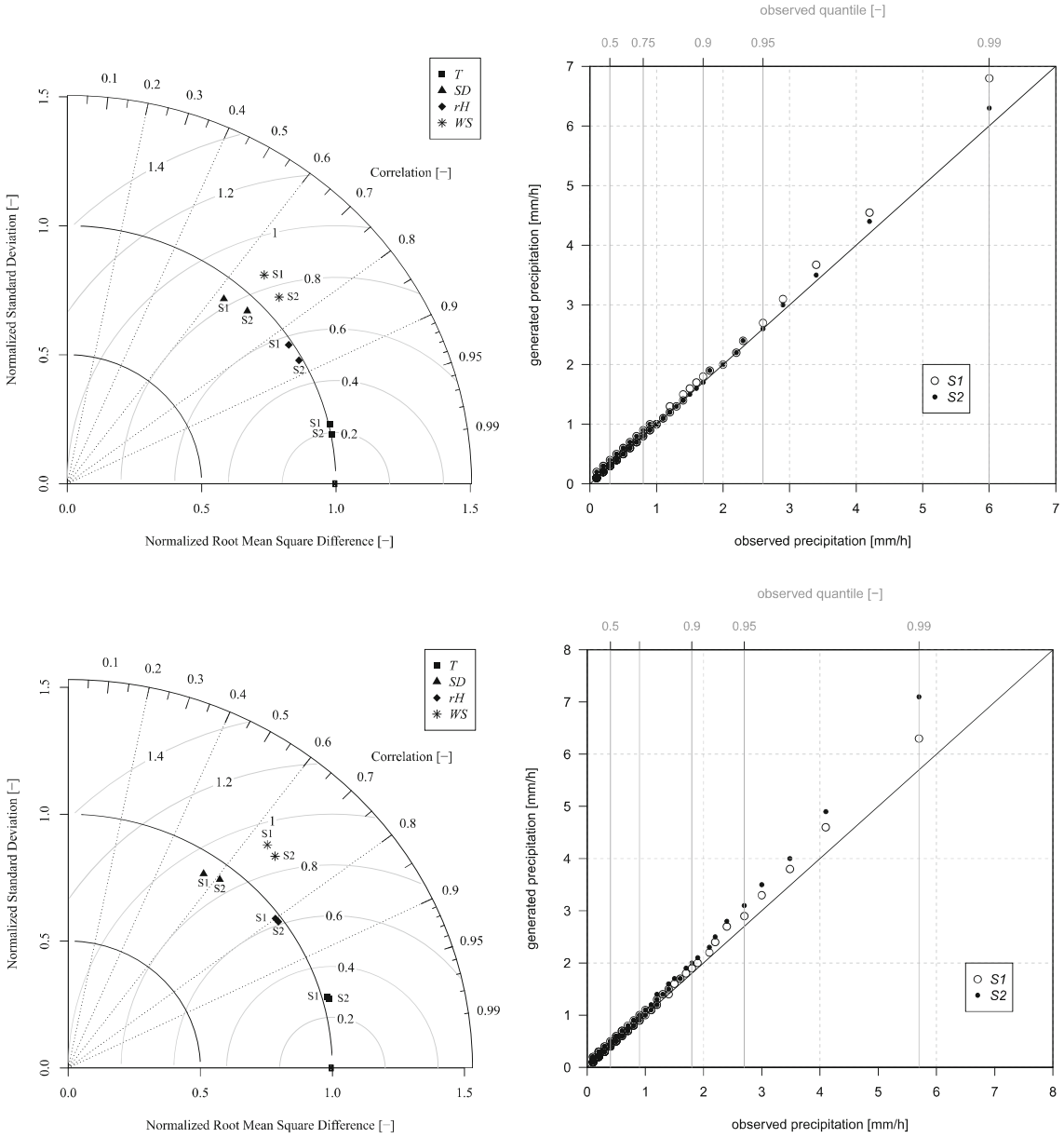

Fig. 6 (left) Normalized root mean square difference [-], normalized standard deviation [-], and correlation [-] of the generated data of *T*, *SD*, *rH*, and *WS* for Selection 1 (*S1*) and Selection 2 (*S2*); (right) the quantiles of the observed and generated precipitation [mm/h] at climate stations Dresden (top) and Fichtelberg (bottom) based on six stations and the calculation of *ED* using only *T* and *P*

the *ED* calculation, their statistics show obviously worse results for both stations and both selection approaches (Fig. 6 (left)). The temperature data fit also slightly worse because the minimum and maximum temperature were not included in the *ED* calculation. However, the quantiles of the precipitation data show better results for both stations and both selection approaches (Fig. 6 (right)). For station Dresden, the quantiles show almost perfect agreements with the observed quantiles. This is caused by the selection of the most similar day based on the two climate elements. Hence, the impact of precipitation in an ensemble of only 2 climate elements corresponds to a weight of 1/2, and in an ensemble of 7 elements (Sections 4.1–4.3) to a weight of only 1/7.

For climate station Fichtelberg, the inclusion of the OWP leads to equal or even worse results, e.g., of the precipitation quantiles. Again, this is caused by the fact that for the same *OWP*, the climate characteristics at station Fichtelberg differ from those of the other five stations.

4.5 Mean diurnal cycles

The mean diurnal cycles are analyzed to examine whether the mean daily statistics and variations are preserved by EDM. The diurnal cycles were determined for the temperature, the sunshine duration, the relative humidity, and the wind speed by calculating the daily means or sums based on the observed and generated hourly data of the years 1995–2014. Afterwards, the mean values were calculated for each hour of the day.

Figure 7 shows the mean diurnal cycles of the four climate elements at climate station Dresden. For the temperature, the sunshine duration, and the relative humidity, the mean diurnal cycles based on the generated data agree with those based on the observed data. Only for the wind speed, the diurnal cycles of the generated data show an underestimation during the night and an overestimation during the day. However, these are both very small and negligible, with maximum differences of − 0.2 m/s and 0.2 m/s, respectively. The strong results are caused by the similar climate conditions of the used basic climate stations (cf. Table 1). Furthermore, it becomes apparent that the two corrections of the sunshine duration and the correction of the relative humidity have no influence on the mean diurnal cycle.

The mean diurnal cycles of the four climate elements at climate station Fichtelberg are shown in Fig. 8. In contrast to station Dresden, the mean diurnal cycles of station Fichtelberg have a worse agreement for all elements and both selection approaches. The mean temperature is overestimated for each hour, while the highest differences occur in the early afternoon. Concerning the sunshine duration, the mean diurnal cycles of the generated data give a slight overestimation for the daytime hours. During the nighttime hours, there are no differences because these hours are automatically set to 0.0 min. A distinct underestimation occurs in the relative humidity data of both selections. The highest differences occur for the afternoon hours and amount to − 10%.

The diurnal cycle of the wind speed at the climate station Fichtelberg is characterized by a maximum during nighttime and a minimum during the afternoon, which is in line with empirical findings on the wind behavior at mountaintops (cf. Blüthgen and Weischet 1980; Stull 2000).

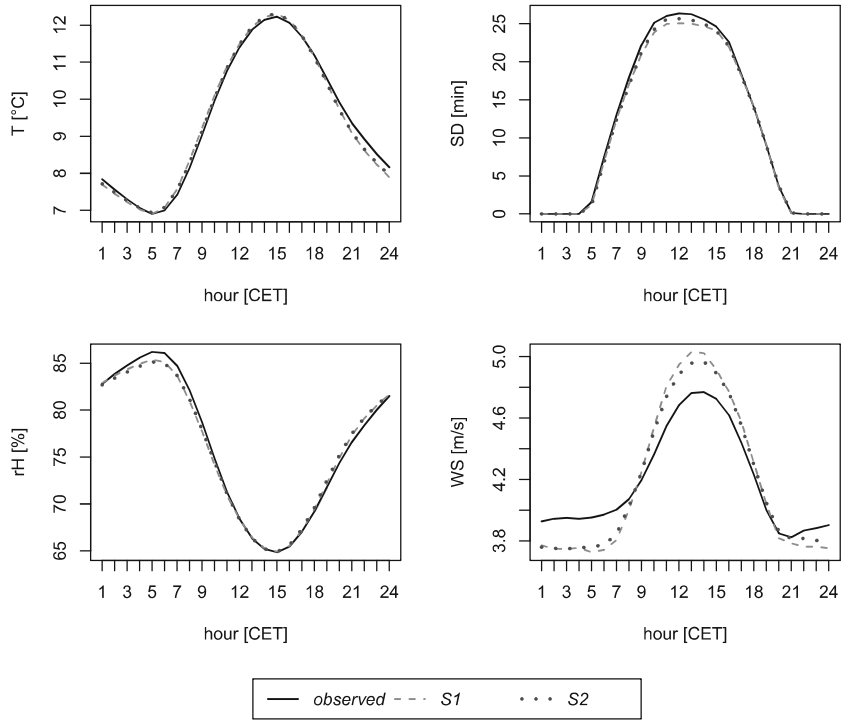

Fig. 7 Mean diurnal cycle of *T* [°C], *SD* [min], *rH* [%], and *WS* [m/s] of the observed data and the generated data of Selection 1(*S1*) and Selection 2 (*S2*) at climate station Dresden based on five stations

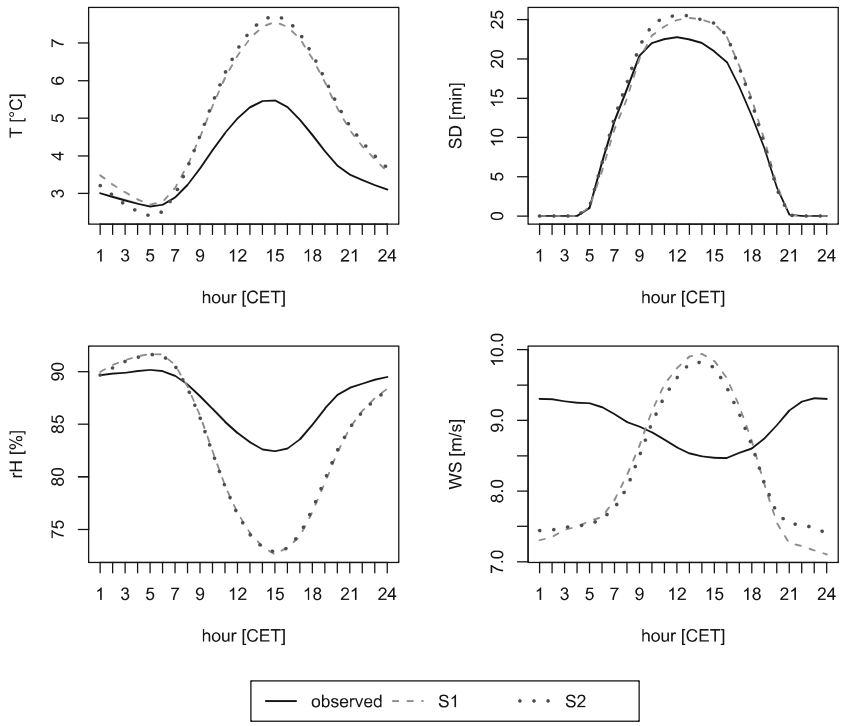

Fig. 8 Mean diurnal cycle of *T* [°C], *SD* [min], *rH* [%], and *WS* [m/s] of the observed data and the generated data of Selection 1 (*S1*) and Selection 2 (*S2*) at climate station Fichtelberg based on five stations

However, for wind speed, both EDM selection approaches deliver diurnal cycles which are inverse to the observed one, with an overestimation in the afternoon and an underestimation at nighttime. The underestimation is greater but still small, with deviations from the observed values up to − 2.2 m/s (*S1*), and the overestimation amounts to only 1.4 m/s (*S1*). The inversion of the diurnal cycle is caused by the differences in the climate characteristic between the station Fichtelberg and the other five climate stations. An analysis of the disaggregation of the dataset of Fichtelberg by using only Fichtelberg itself as basic station showed that the inverse diurnal cycle is then reproduced by the EDM.

Hence, the EDM in its current stage of development is not yet able to reproduce such an inverse cycle when the basic stations are not characterized by similar climate conditions. These differences in the climate conditions of the basic stations are also the reason for the over- and underestimations of the other three climate elements. The diurnal cycle of the

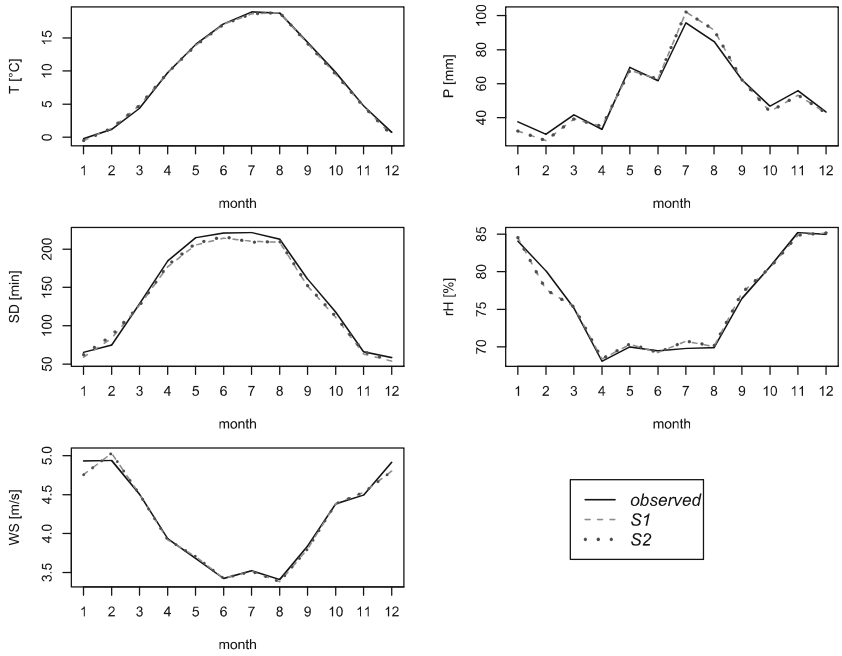

Fig. 9 Mean annual cycle of *T* [°C], *P* [mm] *SD* [min], *rH* [%], and *WS* [m/s] of the observed data and the generated data of Selection 1 (*S1*) and Selection 2 (*S2*) based on aggregated mean monthly values at climate station Dresden based on five stations

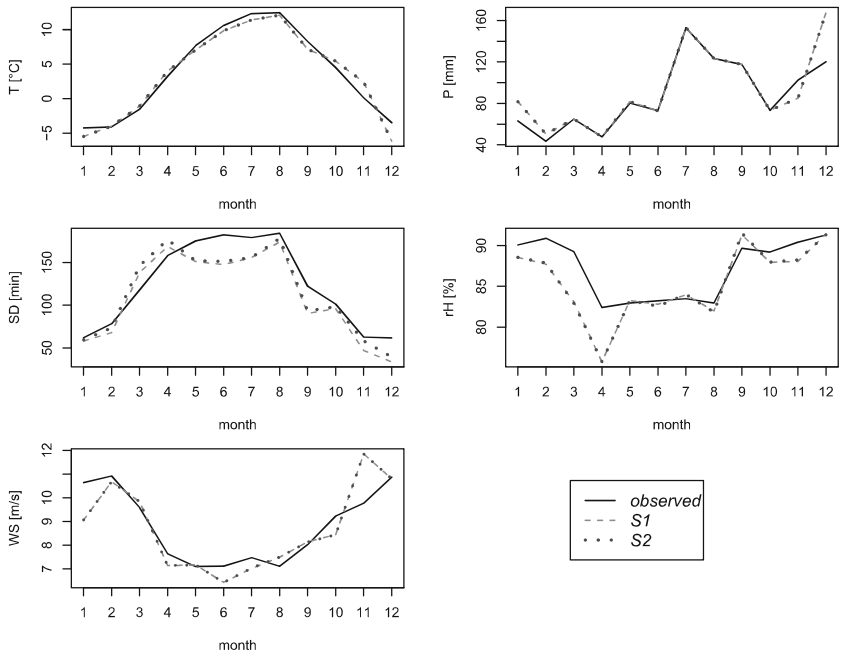

Fig. 10 Mean annual cycle of *T* [°C], *P* [mm] *SD* [min], *rH* [%], and *WS* [m/s] of the observed data and the generated data of Selection 1 (*S1*) and Selection 2 (*S1*) based on aggregated mean monthly values at climate station Fichtelberg based on five stations

observed basic values should fit the diurnal cycle of the disaggregated station. Therefore, the model application is restricted to basic data representing similar climatic conditions.

4.6 Mean annual cycles based on mean monthly values

Comparable to Section 4.5, in this section, the mean annual cycles of all climate elements, including precipitation, are analyzed. The mean monthly data were calculated based on the observed and generated daily data.

The generated mean annual cycles are almost identical to the observed cycles for all climate elements at station Dresden (Fig. 9). This is caused by the preservation of the daily sums or means of the climate elements, which is a basic function of EDM. The small differences of the sunshine duration and the relative humidity result from the corrections implemented in EDM (cf. Section 3.1).

In general, these findings also apply to the annual cycles at climate station Fichtelberg (Fig. 10), but the underestimations of the mean monthly sunshine duration and relative humidity are greater since more days are affected by the corrections (cf. Section 4.1.2). Furthermore, there are greater differences for all elements due to the different climate characteristics of the basic stations.

4.7 Functionality and performance of the EDM in comparison to *MELODIST*

To further assess the performance of the EDM and the quality of the generated datasets, a comparison with the MEteoroLOgical observation time series DISaggregation Tool (*MELODIST*) developed by Förster et al. (2016) is made in this section. *MELODIST* is a robust, reliable, and transferable tool to disaggregate daily time series of the climate elements *T*, *rH*, *WS*, *P*, and shortwave radiation. Physical consistency among the climate elements is not

Table 4 Statistics of the observed and generated data of *T* [°C] for the stations De Bilt and Dresden

Climate station	Dataset	$\tilde{x}$	σ	*RMSE*	*r*
De Bilt	Observed	10.42	6.88		
	MELODIST	10.30	6.94	1.74	0.97
	EDM De Bilt *S1*	10.43	6.85	1.93	0.96
	EDM Sax *S1*	10.43	6.84	2.05	0.96
Dresden	observed	9.44	8.42		
	EDM Dresden *S1*	9.43	8.41	1.82	0.98
	EDM Sax *S1*	9.44	8.44	1.56	0.98

Table 5 Statistics of the observed and generated data of *rH* [%] for the stations De Bilt and Dresden

Climate station	Dataset	$\tilde{x}$	σ	*RMSE*	*r*
De Bilt	Observed	81.82	15.12		
	MELODIST	81.63	15.48	12.67	0.66
	EDM De Bilt *S1*	81.65	14.83	8.60	0.84
	EDM Sax *S1*	81.64	14.94	9.34	0.81
Dresden	observed	76.17	17.19		
	EDM Dresden *S1*	76.02	17.01	9.30	0.85
	EDM Sax *S1*	76.11	16.83	8.26	0.88

inherent in the methodology of *MELODIST* as it disaggregates each element independently. Most of the climate elements are disaggregated by using parsimonious methods with basic levels of complexity. The daily values of *T* are disaggregated using a cosine function with T_{min} at the time of sunset and T_{max} 2 h after sun noon. For disaggregating *rH*, the model generates hourly values of dew point temperature. Similar to the disaggregation of *T*, the values of *WS* are disaggregated by means of a cosine function. And for the disaggregation of *P*, the multiplicative cascade model after Olsson (1998) was applied.

For this comparison, the daily data of the climate station De Bilt were disaggregated two times for the validation period, January 1991–December 2014 (Förster et al. 2016), firstly, by using De Bilt as sole basic station (dataset "*EDM* De Bilt"), and secondly, by using the six Saxon stations as basic stations (dataset "*EDM* Sax"). As De Bilt was disaggregated with itself as basic station, the same procedure was done for Dresden (dataset "*EDM* Dresden") and the results are compared to those in Section 4.1.1 (dataset "*EDM* Sax").

Following the analyses of Förster et al. (2016), the statistical values $\tilde{x}$, σ, *RMSE*, and *r* were calculated for *T*, *rH*, and *WS* (Tables 4, 5, 6), and for *P*, five major characteristics of hourly precipitation features of the observed and generated data were calculated (Table 7).

It can be seen, that EDM and *MELODIST* perform equal for the disaggregation of *T* for station De Bilt. The statistics show only small differences for *RMSE* with slightly worse results for the two data sets generated by the EDM (Table 4). Concerning station Dresden, the EDM performs also very well due to the very homogeneous diurnal cycle of *T* (cf. Section 4.1). Hence, for the disaggregation of *T*, also, a parsimonious method is sufficient (*MELODIST*).

Concerning the disaggregation of *rH* for De Bilt, EDM performs better than *MELODIST*, with distinct higher correlations and smaller *RMSE*, and also smaller standard deviations (Table 5). For station Dresden, the results are similar for both disaggregations with slightly smaller *RMSE*, smaller standard deviation, and slightly higher correlation for the data set "*EDM* Sax S1."

The correlations of the disaggregated *WS* for De Bilt are distinctly higher for the EDM datasets; although, the *RMSE* are higher (Table 6). For station Dresden, the correlation is slightly higher for the dataset "*EDM* Sax S1".

For station De Bilt, the results for *P* show that *MELODIST* overestimates the mean duration of precipitation events and underestimates the number of precipitation events per year. In contrast, EDM generates shorter durations of precipitation events, less numbers of precipitation events per year (data set "*EDM* Sax S1"), and less numbers of hours with $P > 0.0$ mm/h per day while the mean precipitation sum of events is conserved. The results for Dresden reveal that EDM tends to underestimate the duration and numbers of precipitation events as already assumed in Section 4.1.

Table 6 Statistics of the observed and generated data of *WS* [m/s] for the stations De Bilt and Dresden

Climate station	Dataset	$\tilde{x}$	σ	*RMSE*	*r*
De Bilt	Observed	3.49	1.89		
	MELODIST	3.49	1.59	1.05	0.38
	EDM De Bilt *S1*	3.48	1.94	1.44	0.72
	EDM Sax *S1*	3.49	1.97	1.56	0.68
Dresden	Observed	4.18	2.15		
	EDM Dresden *S1*	4.18	2.17	1.70	0.69
	EDM Sax *S1*	4.18	2.30	1.65	0.73

Table 7 Major characteristics of hourly precipitation features of the observed and generated data for the stations De Bilt and Dresden

Climate station	Dataset	Mean duration of events [h]	Mean precipitation sum of events [mm]	Mean duration of dry spells [h]	Number of events per year	Number of hours with $P > 0.0$ mm/h per day
De Bilt	Observed	2.99	2.45	22.02	351	2.9
	MELODIST	3.91	2.52	21.76	342	-
	EDM De Bilt *S1*	2.53	2.41	22.04	357	2.5
	EDM Sax *S1*	2.59	2.50	23.03	342	2.4
Dresden	Observed	2.83	2.11	25.45	290	2.4
	EDM Dresden *S1*	2.31	2.18	26.90	275	1.8
	EDM Sax *S1*	2.54	2.11	25.70	285	2.1

It can be summarized that both disaggregation tools perform comparable for each climate element while both show some limitations. But the high benefit of the generated datasets of EDM is the physical consistency over all climate elements.

5 Summary and conclusions

In this paper, the structure and results of a newly developed multivariate non-parametric resampling model, the Euclidean Distance Model (EDM), for the hourly disaggregation of daily climate data are presented. As a case study, six climate stations located in the Free State of Saxony (Germany) were selected. The daily climate data of stations Dresden and Fichtelberg were exemplarily disaggregated for the years 1995–2014 and compared to the observed hourly data.

The generated datasets that were disaggregated by using alternatively either five or six basic stations show very similar results and strong agreements for all the studied climate elements. The inclusion of the disaggregated station itself into the pool of basic stations leads to some improvements of the model performance. These improvements are greater when the other basic stations are characterized by different climate conditions, as is the case for the mountain station Fichtelberg. It is shown that the results always fit better for such climate elements, which are characterized by a homogenous diurnal cycle that is well reproduced by EDM. Hence, each generated dataset shows the best results for temperature and the worst for wind speed and sunshine duration.

Concerning precipitation, EDM tends to overestimate the quantiles of the hourly data, especially for heavy and extreme values (quantiles $\geq 90\%$). There are various potential reasons for this. (i) The EDM tends to generate less and shorter precipitation events. This might be due to rounding small intensities to 0.0 mm/h and a preferred selection of basic day with less or shorter precipitation events. (ii) The rounding of the disaggregated hourly intensities itself. (iii) The equal-weighted impact of precipitation in the calculation of the *ED*. (iiii) The pool of heavy and extreme precipitation events is significantly smaller. (iiiii) There are supposed to be unintended influences of other variables used in the EDM resampling.

An exemplarily investigation of the magnitude of overestimation in terms of a confidence interval of an extreme value statistic as used for engineering design and flood simulation showed that the differences of the quantiles lay within the confidence interval of the fitted extreme value distribution for design rainfall. Hence, the uncertainty of the estimation of design rainfall is much higher, than the uncertainty of the EDM model. However, the differences should be investigated and validated in each case of an EDM application.

The overestimation might be an advantage in the field of hydroengineering. Since an increase in the hourly intensity of heavy precipitation events is already observed and is expected to continue in the future, such overestimation anticipates this trend. But of course, the higher costs of hydroengineering by using these higher intensities have to be weighed against the benefits, e.g., the benefits of higher flood protection. However, with regard to error propagation and unwanted biasing of post-calculated cost functions in optimal decision strategies, the underlying models such as EDM should advantageously be free of any bias.

Furthermore, it is shown that, for all datasets, the inclusion of the *OWP* in the selection of the most similar day leads to small improvements for all climate elements besides the precipitation quantiles for station Fichtelberg. Here, the *OWP* causes even a worsening of the results, which is caused by the disregard of the meso-climatic variations within the investigated territory and their impact on the setup of the basis data pool. Furthermore, the worsening results from smaller data pool for events with heavy precipitation. Therefore, the *OWP* are not mandatory to obtain accurate hourly data. It remains to be investigated whether a more sophisticated *OWP* approach based on a refined similarity metrics on the base of further meteorological field observations can enhance the EDM skill. It is expected to improve the performance of the EDM by taking the mean flow directions into account as they have a high impact on the humidity and temperature of an

airmass. Hence, they are an important indicator for the (expected) weather situation, e.g., they impact the precipitation events due to possible luv-lee effects.

The analyses for the summer and winter half-years reveal that EDM delivers better results for the winter half-year. This applies to both analyzed stations and all climate elements besides the precipitation for station Fichtelberg due to different climate characteristics at this mountain station. For the summer half-year, slightly worse results are shown for both analyzed stations due to the increased turbulence and unstable weather conditions during these months.

The results for the disaggregation using only the temperature and precipitation for the calculation of *ED* reveal that the generated data fit better if the climate element is involved in the calculation of the *ED*. In addition, the fewer elements used, the better the fit of the results of the used elements as their influences on the selection of the most similar day are increased.

Due to the functionality of EDM, the daily sums or means of the climate elements are conserved. This leads to an exact reproduction of the mean diurnal cycle if the used basic stations show similar climate characteristics. If this is not the case, as shown for station Fichtelberg, there are some over- and underestimations of all elements and even an inversion of the diurnal cycle of the wind speed.

Concerning the mean annual cycles based on the mean monthly values, EDM delivers an accurate reproduction for each climate element. For the mean annual cycles, the different climate characteristics of the used stations have lower effects.

An additional comparison of the functionality and performance of the EDM to the tool *MELODIST*, showed that the EDM delivers comparable results for all disaggregated climate elements. Both tools have their limitations, but the physical consistency over all disaggregated climate elements is a high benefit of EDM. Therefore, these generated datasets might be more suitable as input data for hydrological or ecological modeling.

EDM is a very robust and flexible model that can be applied to any climate station if hourly data are available within the same climate region. This method works with several climate elements as well as with only one climate element. EDM delivers data with strong correlation to the observed data, maintaining their statistical characteristics, and the delivered hourly data set is physical consistent over the disaggregated climate elements. Additionally, a technical advantage of EDM is its efficient computing performance and that there is no time-consuming calibration needed.

However, there are also some restrictions in the application of this model. (i) The basic climate stations should have similar climate conditions to those of the target station. (ii) EDM also requires a sufficient data base of (continuously) recorded hourly data.

The climate stations used for this study were selected as they belong to the same macro- and meso-climatic zone and as they are close to each other. It is recommended to preferably pool only stations of only one region of similar climate, e.g., as classified by Kronenberg et al. (2015), but usually this means a significant reduction of available climate data, especially concerning hourly recorded data. Although the selected climate stations spread over four climate regions, the climate characteristics of the stations were similar enough to achieve high correspondence of the observed and generated hourly data besides some restriction for the mountain station Fichtelberg.

How many basic data are sufficient cannot be clearly defined. The EDM works independently of the amount of basic data. The disaggregation with only one basic station was tested for the comparison with the tool *MELODIST*, and the results showed no distinct worsening. However, for analyses with climatological context, a data base covering 30 continuous years (climatological period) would be required. But regarding the real spatio-temporal data availability, at least 10 years of continuously recorded data are required. Of course, the more basic data are available the better the disaggregated data correspond and the more the generated diurnal cycles vary.

Finally, but importantly, since EDM is a resampling model and uses the observed diurnal cycles of the past, the generated hourly data are more or less a copy of the past. The applied offset or boost factors for new "records" in the target time-series, however, allow the generation of data which have not yet been observed. Therefore, the model is capable of taking future trends (like climate change) into account; it can disaggregate daily data from statistical downscaling (as, e.g., *WETTREG*, Enke et al. 2005; Kreienkamp et al. 2010) of climate projections. Such a model chain allows impact modeling with hourly input requirements and might allow the analysis of future extremes by changing the occurrences of the observed extremes. Including generated future *OWP* would improve the results of the disaggregation of future climate data because changes of the frequencies of the weather patterns are expected due to climate changes. But their generation is extremely complex and time-consuming. Future *OWP* time series exist for Germany and Saxony after the classification of Enke et al. (2005). For Germany, they are generated by the model *WETTREG* and for Saxony, they are generated by the model *WEREX*. These *OWP* are weather patterns of the atmospheric condition concerning temperature and humidity. They do not comprise information of synoptic flow patterns and the mean flow direction. But such information would be required especially for the disaggregation of future precipitation time series. As far as I am aware, there is still no free available dataset of *OWP*s as used for the present study. The generation of such future *OWP* datasets is still a complex field of research.

Funding Open Access funding enabled and organized by Projekt DEAL.

Appendix

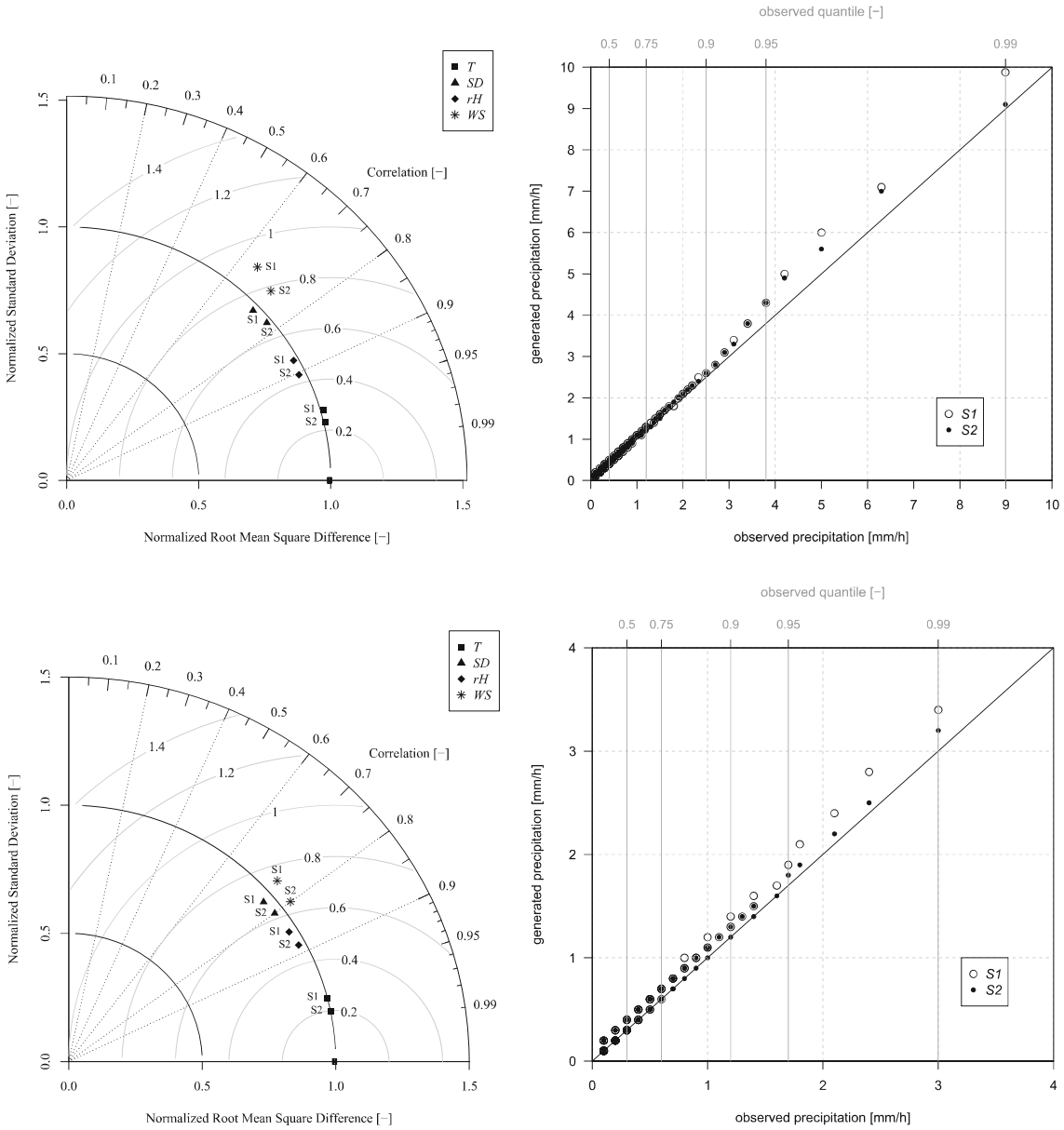

Fig. 11 (left) Normalized root mean square difference [-], normalized standard deviation [-], and correlation [-] of the generated data of *T*, *SD*, *rH*, and *WS* for Selection 1 (*S1*) and Selection 2 (*S2*); (right) the quantiles of the observed and generated precipitation [mm/h] for the summer half-year (top) and the winter half-year (bottom) at climate station Dresden based on five stations

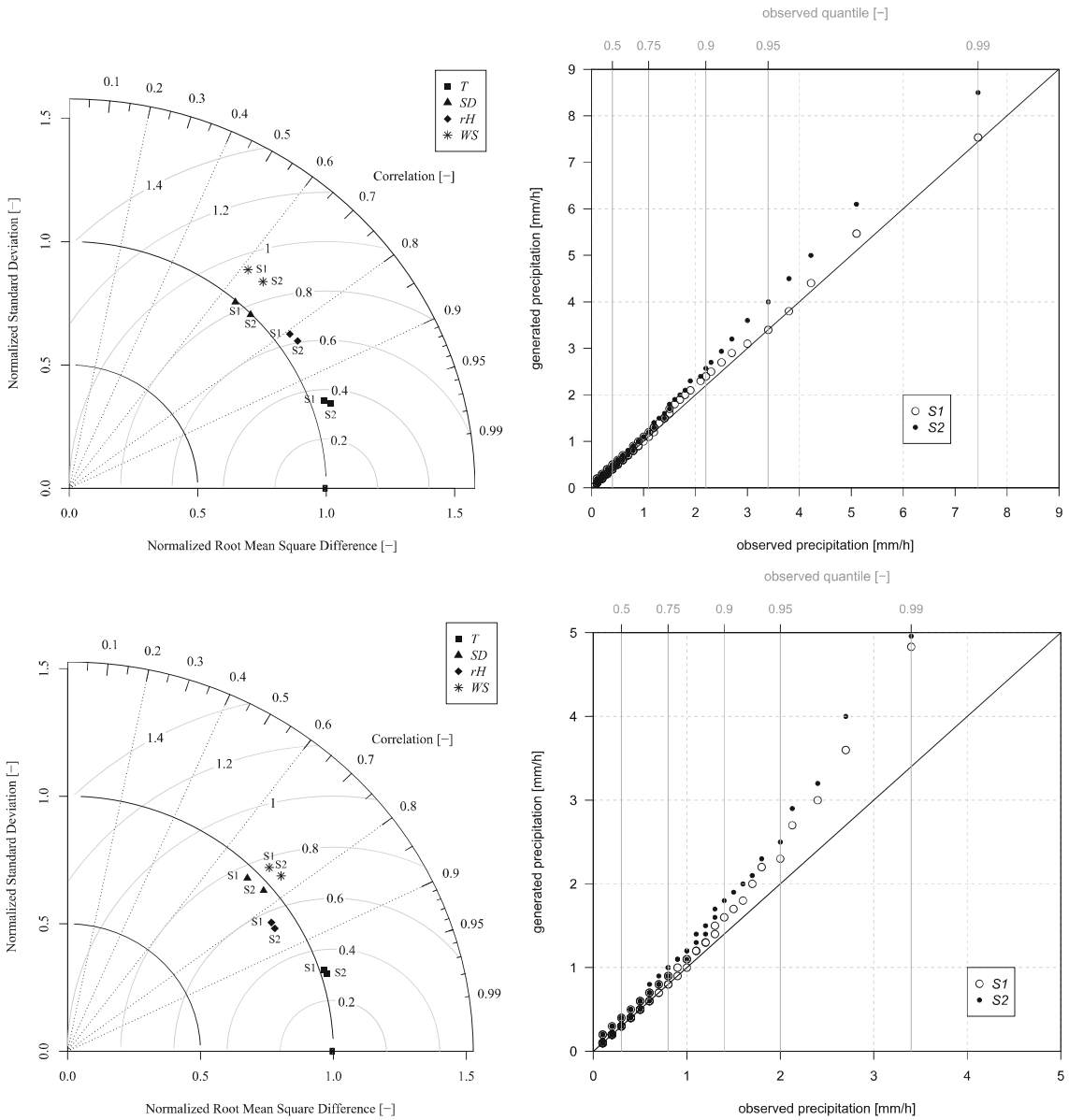

Fig. 12 (left) Normalized root mean square difference [-], normalized standard deviation [-], and correlation [-] of the generated data of *T*, *SD*, *rH*, and *WS* for Selection 1 (*S1*) and Selection 2 (*S2*); (right) the quantiles of the observed and generated precipitation [mm/h] for the summer half-year (top) and the winter half-year (bottom) at climate station Fichtelberg based on five stations

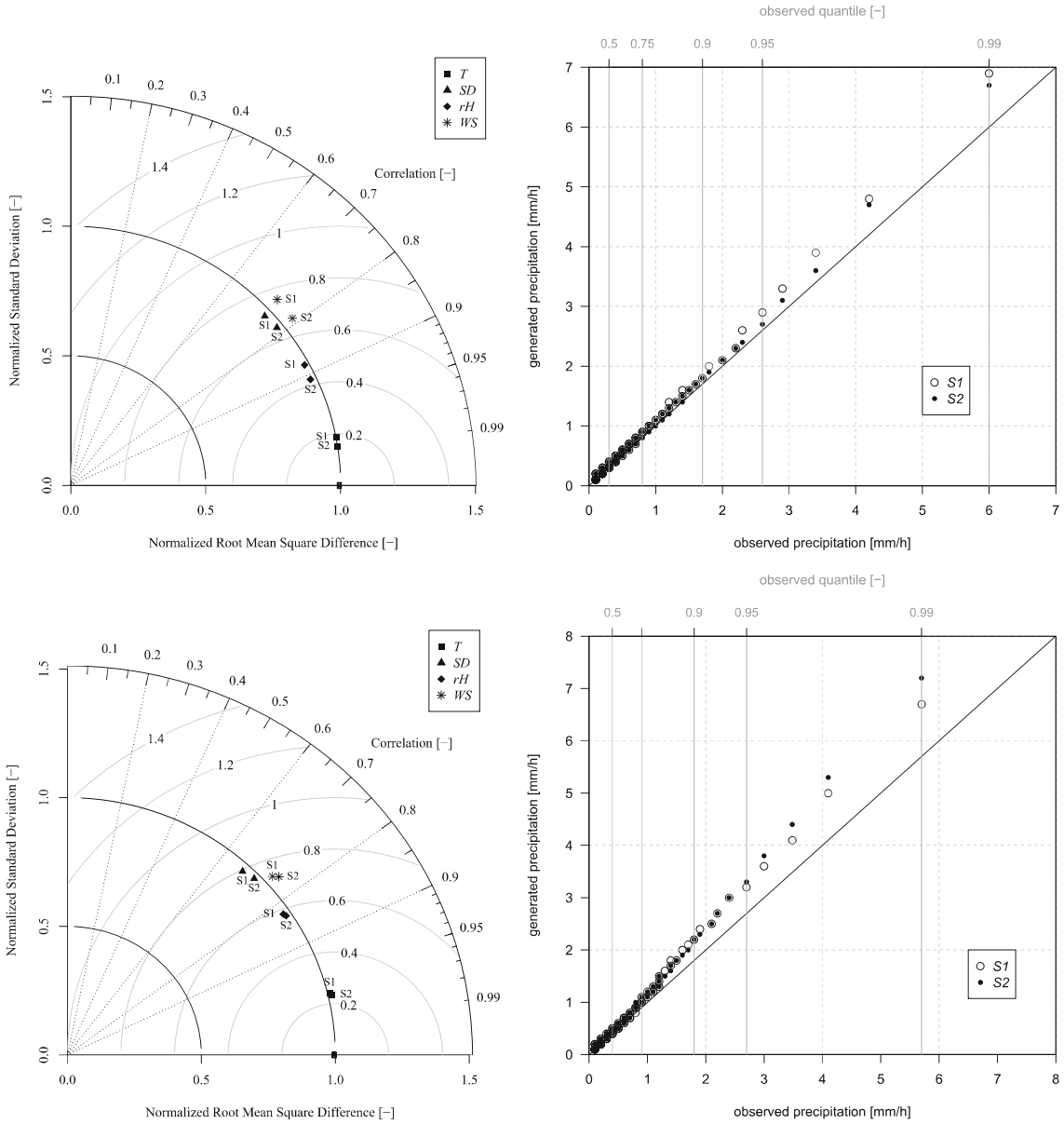

Fig. 13 (left) Normalized root mean square difference [-], normalized standard deviation [-], and correlation [-] of the generated data of *T*, *SD*, *rH*, and *WS* for Selection 1 (*S1*) and Selection 2 (*S2*); (right) the quantiles of the observed and generated precipitation [mm/h] at climate stations Dresden (top) and Fichtelberg (bottom) based on six stations

Table 8 Statistics of the observed and generated data of the summer half-year for station Dresden based on five stations

Climate element	Sample size	Dataset	x_{min}	x_{max}	$\tilde{x}$	x_{med}	$x_{95\%}$	σ	σ_n	r	$RMSD_n$
T [°C]	81,192	Observed	−5.7	36.7	15.42	15.3	29.3	5.90	-	-	-
		S1	−8.0	37.7	15.42	15.3	29.5	5.96	1.01	0.96	0.28
		S2	−7.2	36.9	15.42	15.3	29.5	5.92	1.01	0.97	0.23
SD [min] *	52,849	Observed	0.0	60.0	25.67	19.0	60.0	25.0	-	-	-
		S1	0.0	60.0	24.85	17.8	60.0	24.41	0.97	0.73	0.73
		S2	0.0	60.0	25.00	18.0	60.0	24.59	0.97	0.77	0.67
rH [%]	81,192	Observed	14.0	100.0	70.67	73.0	100.0	18.94	-	-	-
		S1	2.8	100.0	70.59	72.8	100.0	18.58	0.98	0.88	0.50
		S2	14.3	100.0	70.63	72.8	100.0	18.44	0.98	0.90	0.43
WS [m/s]	81,192	Observed	0.0	14.1	3.63	3.4	8.6	1.71	-	-	-
		S1	0.0	17.3	3.63	3.3	9.1	1.89	1.11	0.65	0.89
		S2	0.0	16.5	3.63	3.3	8.9	1.84	1.11	0.72	0.78
P [mm] **	6907	Observed	0.1	36.6	1.05	0.4	3.8	1.89	-	-	-
	6322	*S1*	0.1	48.6	1.15	0.5	4.3	2.20	1.16	-	-
	6502	*S2*	0.1	48.6	1.12	0.5	4.3	1.95	1.03	-	-

* Excluding night time values and days with $SD = 0.0$ min

** Based on hourly values > 0.0 mm

Table 9 Statistics of the observed and generated data of the winter half-year for station Dresden based on five stations

Climate element	Sample size	Dataset	x_{min}	x_{max}	$\tilde{x}$	x_{med}	$x_{95\%}$	σ	σ_n	r	$RMSD_n$
T [°C]	81,000	Observed	−20.7	26.0	3.44	3.4	17.1	5.93	-	-	-
		S1	−22.7	26.3	3.44	3.4	16.9	5.91	1.00	0.97	0.25
		S2	−20.6	25.8	3.44	3.4	17.1	5.93	1.00	0.98	0.20
SD [min] *	27,378	Observed	0.0	60.0	20.75	5.0	60.0	24.89	-	-	-
		S1	0.0	60.0	19.40	3.4	60.0	23.88	0.96	0.76	0.68
		S2	0.0	60.0	19.81	4.0	60.0	24.00	0.96	0.80	0.62
rH [%]	81,000	Observed	5.0	100.0	81.69	84.0	100.0	13.09	-	-	-
		S1	11.2	100.0	81.63	83.7	100.0	12.67	0.97	0.85	0.54
		S2	14.4	100.0	81.65	83.8	100.0	12.75	0.97	0.88	0.48
WS [m/s]	81,000	Observed	0.0	20.4	4.74	4.4	11.4	2.40	-	-	-
		S1	0.0	20.5	4.74	4.4	12.1	2.52	1.05	0.74	0.74
		S2	0.0	21.3	4.74	4.4	11.9	2.49	1.05	0.80	0.65
P [mm] **	9204	Observed	0.1	11.4	0.52	0.3	1.7	0.64	-	-	-
	8171	*S1*	0.1	12.5	0.58	0.3	1.9	0.73	1.14	-	-
	8589	*S2*	0.1	12.0	0.55	0.3	1.8	0.69	1.08	-	-

* Excluding night time values and days with $SD = 0.0$ min

** Based on hourly values > 0.0 mm

Table 10 Statistics of the observed and generated data of the summer half-year for station Fichtelberg based on five stations

Climate element	Sample size	Dataset	x_{min}	x_{max}	$\tilde{x}$	x_{med}	$x_{95\%}$	σ	σ_n	r	$RMSD_n$
T [°C]	55,505	Observed	−10.8	28.6	9.35	9.4	21.8	5.49	-	-	-
		S1	−15.3	30.0	9.35	9.3	23.0	5.78	1.05	0.94	0.35
		S2	−11.6	30.0	9.35	9.2	23.1	5.89	1.05	0.95	0.34
SD [min] *	35,614	Observed	0.0	60.0	24.07	15.0	60.0	24.52	-	-	-
		S1	0.0	60.0	22.03	9.5	60.0	22.03	0.99	0.65	0.83
		S2	0.0	60.0	22.61	11.0	60.0	22.61	0.99	0.71	0.76
rH [%]	55,505	Observed	12.0	100.0	82.60	86.0	100.0	17.08	-	-	-
		S1	16.6	100.0	81.42	86.2	100.0	18.14	1.06	0.81	0.64
		S2	13.6	100.0	81.36	86.3	100.0	18.30	1.06	0.83	0.61
WS [m/s]	55,505	Observed	0.0	25.6	7.33	6.9	17.2	3.60	-	-	-
		S1	0.0	59.0	7.33	6.7	19.3	4.05	1.13	0.62	0.94
		S2	0.0	45.7	7.33	6.7	19.1	4.05	1.13	0.67	0.87
P [mm] **	5960	Observed	0.1	32.9	0.94	0.4	3.4	1.74	-	-	-
	5666	*S1*	0.1	33.1	0.99	0.5	3.4	1.73	0.99	-	-
	5284	*S2*	0.1	26.6	1.07	0.5	4.0	1.84	1.06	-	-

* Excluding night time values and days with $SD = 0.0$ min

** Based on hourly values > 0.0 mm

Table 11 Statistics of the observed and generated data of the winter half-year for station Fichtelberg based on five stations

Climate element	Sample size	Dataset	x_{min}	x_{max}	$\tilde{x}$	x_{med}	$x_{95\%}$	σ	σ_n	r	$RMSD_n$
T [°C]	43,464	Observed	−21.9	20.1	−0.71	−0.5	12.8	6.08	-	-	-
		S1	−23.7	22.2	−0.71	−0.6	13.4	6.18	1.02	0.95	0.32
		S2	−25.4	23.2	−0.71	−0.6	13.3	6.20	1.02	0.95	0.31
SD [min] *	15,194	Observed	0.0	60.0	25.32	13.0	60.0	26.22	-	-	-
		S1	0.0	60.0	21.69	5.9	60.0	25.13	0.96	0.71	0.75
		S2	0.0	60.0	22.51	7.1	60.0	25.44	0.96	0.76	0.68
rH [%]	43,464	Observed	5.0	100.0	87.17	97.0	100.0	19.89	-	-	-
		S1	6.9	100.0	86.08	93.8	100.0	18.26	0.92	0.84	0.56
		S2	6.1	100.0	86.04	93.7	100.0	18.23	0.92	0.85	0.53
WS [m/s]	43,464	Observed	0.0	32.0	9.57	9.2	22.0	4.86	-	-	-
		S1	0.0	38.8	9.57	8.9	23.9	5.08	1.05	0.73	0.76
		S2	0.0	37.2	9.57	8.9	23.8	5.14	1.05	0.76	0.72
P [mm] **	5144	Observed	0.1	10.0	0.60	0.3	2.0	0.73	-	-	-
	4468	*S1*	0.1	13.1	0.69	0.4	2.3	0.97	1.28	-	-
	4042	*S2*	0.1	21.9	0.76	0.4	2.5	1.14	1.56	-	-

* Excluding night time values and days with $SD = 0.0$ min

** Based on hourly values > 0.0 mm

References

Bárdossy A (1998) Generating precipitation time series using simulated annealing. Water Resour Res 34:1737–1744

Beck F, Bárdossy A (2013) Indirect downscaling of hourly precipitation based on atmospheric circulation and temperature. Hydrol Earth Syst Sci 17:4851–4863

Bergström S (1992) The HBV model: its structure and applications. Swedish Meteorological and Hydrological Institute (SMHI), Hydrology, Norrköping

Bissolli P, Dittmann E (2003) The objective weather type classification of the German Weather Service and its possibilities of application to environmental and meteorological investigations. Meteorol Z 10: 253–260

Blüthgen J, Weischet W (1980) Lehrbuch der Allgemeinen Geographie, Band 2, Allgemeine Klimageographie. 3, Auflage Walter de Gruyter, Berlin

Burek P, Rademacher S (2007) Operationelle Hochwasservorhersage für die Elbe mit dem Wasserstandsvorhersagesystem WAVOS. In: Fünf Jahre nach der Flut. Hochwasserschutzkonzepte - Planung, Berechnung, Realisierung. Dresdner Wasserbau-kolloquium 2007. Dresdner Wasserbauliche Mitteilungen Heft 35, Technische Universität Dresden, Dresden, pp. 25–34

Debele B, Srinivasan R, Parlange JY (2007) Accuracy evaluation of weather data generation and disaggregation methods at finer time-scales. Adv Water Resour 30:1286–1300

Enke W, Schneider F, Deutschlaender T (2005) A novel scheme to derive optimized circulation pattern classifications for downscaling and forecast purposes. Theor Appl Climatol 82:51–63. https://doi.org/10.1007/s00704-004-0116-x

Förster C, Hanzer F, Winter B, Marke T, Strasser U (2016) An open-source MEteoroLOgical observation time series DISaggregation tool (MELODIST v01.1.1). Geosci Model Dev 9:2315–2333

Glasbey CA, Cooper G, McGechan MB (1995) Disaggregation of daily rainfall by conditional simulation from a point-process model. J Hydrol 165:1–9

Güntner A, Olsson J, Calver A, Gannon B (2001) Cascade-based disaggregation of continuous rainfall time series: the influence of climate. Hydrol Earth Syst Sci 5:145–164

Kim Y, Rajagopalan B, Lee GW (2016) Temporal statistical downscaling of precipitation and temperature forecasts using a stochastic weather generator. Adv Atmos Sci 33:175–183

Kreienkamp F, Spekat A, Enke W (2010) Weiterentwicklung von WETTREG bezüglich neuartiger Wetterlagen. Bericht, CEC Potsdam im Auftrag eines Konsortiums aus Landesumweltämtern und dem UBA

Kronenberg R, Franke J, Bernhofer C, Körner P (2015) Detection of potential areas of changing climatic conditions at a regional scale until 2100 for Saxony, Germany. Meteorol Hydrol Water Manage 3(2):17–26

Lee T, Jeong C (2014) Nonparametric statistical temporal downscaling of daily precipitation to hourly precipitation and implications for climate change scenarios. J Hydrol 510:182–196

Lisniak D, Franke J, Bernhofer C (2013) Circulation pattern based parameterization of a multiplicative random cascade for disaggregation of observed and projected daily rainfall time series. Hydrol Earth Syst Sci 17:2487–2500. https://doi.org/10.5194/hess-17-2487-2013

Lu Y, Qin XS, Mandapaka PV (2015) A combined weather generator and K-nearest-neighbour approach for assessing climate change impact on regional rainfall extremes. Int J Climatol 35:4493–4508

McCullagh P, Nelder JA (1989) Generalized linear models, 2nd edn. Chapman and Hall, London

Mezghani A, Hingray B (2009) A combined downscaling-disaggregation weather generator for stochastic generation of multisite hourly weather variables over complex terrain: development and multi-scale validation for the Upper Rhone River basin. J Hydrol 377: 245–260

Olsson J (1998) Evaluation of a scaling cascade model for temporal rainfall disaggregation. Hydrol Earth Syst Sci 2:19–30. https://doi.org/10.5194/hess-2-19-1998

Pfützner B, Klöcking B, Becker A (2007) ArcEGMO GIS-gestützte hydrologische Modellierung. BAH – Büro für Angewandte Hydrologie (ed), Berlin und Potsdam

Schulla J, Jasper K (2007) Model description WaSiM-ETH (water balance simulation model ETH). Internal report. Institute for Atmospheric and Climate Science, ETH, Zürich

Schumann A (ed) (2009) Entwicklung integrativer Lösungen für das operationelle Hochwassermanagement am Beispiel der Mulde - Abschlussbericht Verbundvorhaben. Schriftenreihe Hydrologie/ Wasserwirtschaft der Ruhr-Universität Bochum, H 23, ISSN 0949-5975

Sharif M, Burn DH, Hofbauer KM (2013) Generation of daily and hourly weather variables for use in climate change vulnerability assessment. Wat Res Man 27:1533–1550

SMUL (ed) (2005) Klimawandel in Sachsen – Sachstand und Ausblick. Sächsisches Staatsministerium für Umwelt und Landwirtschaft. Eigenverlag. SMUL, Dresden

SMUL (ed) (2008) Sachsen im Klimawandel – Eine Analyse. Sächsisches Staatsministerium für Umwelt und Landwirtschaft, Eigenverlag. SMUL, Dresden

Stull RB (2000) Meteorology for scientists and engineers, Second edn. Brooks/Cole, Pacific Grove

Taylor KE (2001) Summarizing multiple aspects of model performance in a single diagram. J Geophys Res 106:7183–7192

Appendix D

Additional publication 1

Climate changes in extreme precipitation events in the Elbe catchment of Saxony

C. Görner, J. Franke & C. Bernhofer
Technische Universität Dresden, Institute of Hydrology and Meteorology, D-01062 Dresden, Germany
O. Hellmuth
Leibniz Institute for Tropospheric Research, D-04318 Leipzig, Germany

ABSTRACT: To mitigate negative consequences of flooding, flood risk management is necessary which have to be well adapted to the current climate conditions and its changes in the future, especially concerning heavy precipitation events. Therefore, regionalized climate change scenarios are required. Two climate scenarios are analyzed for Saxony and the Upper Mulde river basin as part of the Elbe catchment of Saxony. Furthermore, the projected climate changes for Saxony are presented exemplarily with focus on precipitation. It is examined which changes in the amount, frequency, intensity and return period are projected, especially of heavy rainfall events. With the assumption of a runoff coefficient close to one the occurrence of heavy rainfall will be similar to the occurrence of heavy floods. Therefore, based on these analyses a first guess on the occurrence of future floods and there damage potential is possible.

1 INTRODUCTION

Global climate change is one of the major challenges for mankind and its impact is already noticeable today. Extreme weather situations are increasingly becoming a drastic threat to millions of people and they cause damage of unprecedented dimensions to buildings and infrastructures. More heavy precipitation events in western Germany, more hot and dry summers as well as more severe storms have done high economical damages in Germany during the last decades (UBA & MPI-M 2006; Munich Re Group 2005).

As global climate models predict a clear increase in temperature and weather extremes (IPCC 2001) due to increase in the atmospheric concentration of green house gases it is obvious to relate the reported increase in flood risk to climate change (Bernhofer et al. 2006). Floods, especially flash floods, as a result of heavy rainfall events are widely distributed and have increased significantly in the past decades. To minimize the flooding of populated areas like during the Elbe flood in 2002, flood protection concepts are necessary which have to be well adapted to the current climate conditions and its future changes, especially concerning heavy precipitation events. Speed and degree of climate change influence how and how fast we have to adapt. Therefore, the decision makers in policy, economy and administration have to know where and to which degree the climate will change (UBA & MPI-M 2006).

This paper presents the results of the investigation of the future climate changes for the Saxon Elbe river catchment, the changes in the return period of design precipitation and the changes in the maximum possible rainfall amount.

2 DATA

2.1 *Measured data*

The data of the past were measured and provided by the Deutscher Wetterdienst (DWD; German Weather Service). For the reference time series between 1971 and 2003 the data for the elements precipitation and temperature were available in daily resolution for the stations Chemnitz, Fichtelberg, Marienberg, Carlsfeld and Aue.

2.2 *Future climate scenario data*

Two climate scenarios for the ten decades between 2001 and 2100 represented the basic data for the investigation of the future climate changes. The basis for these scenarios was the transient run of the global circulation model ECHAM5/MPI-OM T63L31 of the MPIM (Max-Planck-Institute for Meteorology) at Hamburg for the emission scenarios A2 (regional-economic) and B1 (global-environmental) of the Intergovernmental Panel on Climate Change (IPCC 2001). The regionalized scenarios were calculated by Meteo-Research 2006

within the project ENFORCHANGE. Meteo-Research applied a dynamical statistical downscaling using weather patterns. The scenarios contain daily data for the climate elements precipitation, temperature, relative humidity, air pressure, sunshine duration, cloud cover, and wind force. To assess the possible range of fluctuation of the future climate change, 10 independent simulations have been generated for each decade and each station on the basis of the statistical frequency distribution of the weather patterns of the moisture and temperature regime. Concerning the temperature these 10 simulations show only marginal differences. Therefore, no differentiation between warmer and colder simulations was made. But it was considered reasonable to take the regard annual precipitation sum as a differentiation criterion. On account on this the wettest, driest and most mean simulations were selected and combined to one wet, dry and mean transient realization. (Enke & Kreienkamp 2005)
For all investigations the mean realization for the scenarios A2 and B1 has been chosen while B1 is a more moderate one.

3 CLIMATE CHANGES IN THE SAXON ELBE RIVER CATCHMENT

Precipitation is the most important factor for triggering floods, especially flash floods. And also the temperature plays a decisive role. Hence, both climate elements have been investigated with regard to their changes in the future and the resulting changes in possible flood risk.

3.1 *Investigation area*

Saxony is a federal state in the South-East of Germany. It covers lowlands as well as medium-elevation mountains (Fig. 1).
The mountainous region is part of the Ore Mountains up to a height of around 1200 m. Saxony also covers the Mulde and a part of the Elbe river basin which are the topic of research within Task 21.

3.2 *Analysis of the scenario data*

The analysis of the scenario data was restricted to the precipitation and temperature data which are the most important elements that are mainly examined when climate changes are investigated.

At first the scenario decade 2041-2050 was selected for the investigation of future flood risk. Since this decade shows very little changes in precipitation (frequency, amount) and temperature for the Upper Mulde and Saxon Elbe river catchment, the decade 2091-2100 was chosen instead.

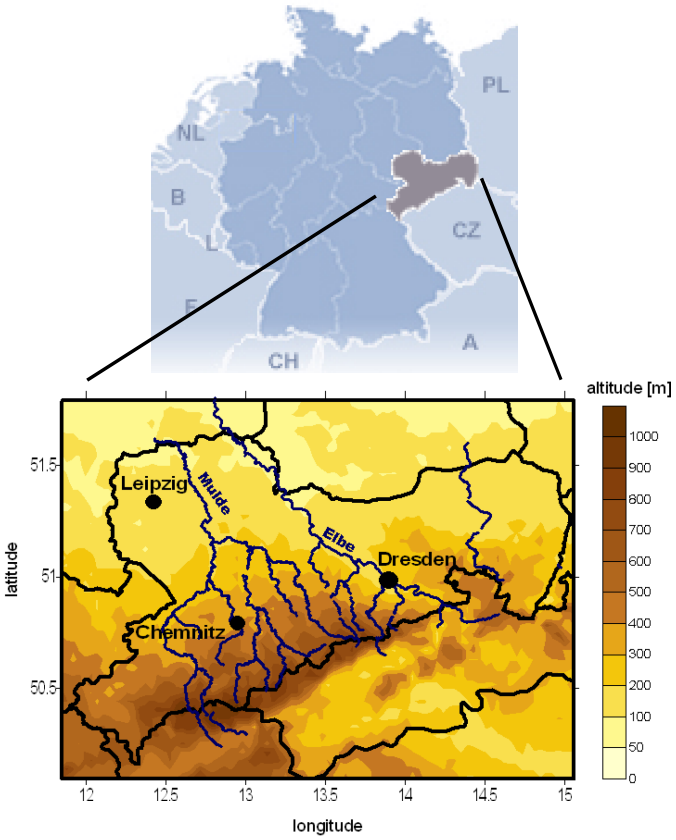

Figure 1: Location of Saxony within Germany (top) and the orography of Saxony (down)

3.2.1 *Changes in summer precipitation*

The meteorological summer (JJA) was selected because this season is characterized by convective precipitation events. And only this kind of rain events has the potential to be such heavy events which are able to trigger flash floods.

There are low changes in precipitation in the decade 2041-2050, especially in the Upper Mulde catchment area. Almost whole Saxony is characterized by a mean decrease in precipitation of 14 % (scenario B1). The area of the Upper Mulde shows a reduction of 5-15 %. The lowlands, especially the north-eastern and central Saxony, show a higher reduction up to 25 %.

For the decade 2091-2100 the decrease in precipitation is more distinct with a mean value of 21 %. But in the Upper Mulde catchment the increment of the decrease in precipitation is more moderate and ranges between 5 % and 20 %. Again, the highest reductions can be found in the lowlands in central and eastern Saxony. There, the reduction is partly up to 35 % (scenario B1).

The following analysis of changes in summer precipitation refers to the station Chemnitz which is situated at the foot of the Ore Mountains (cp. Fig. 1).

In Figure 2 it can be seen that there is an increase in the frequency of days without precipitation for both scenarios. This increase has an amount up to 20 % (from 1971-2000 to 2091-2100 A2). Furthermore, the scenarios show a decrease in days with

less precipitation but an increase in the precipitation class from >20 mm to <50 mm, up to a doubling. These tendencies are already distinguishable by comparing the two past time series.

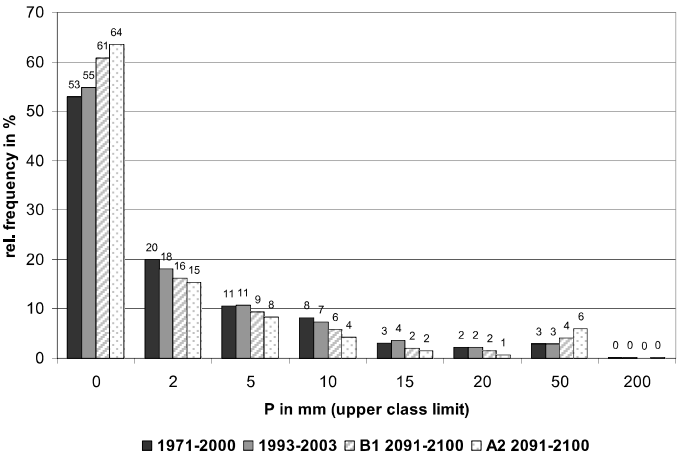

Figure 2. Relative frequency [%] of summer precipitation (JJA) at Chemnitz for the past (1971-200/1993-2003) and the future (2091-2100)

The reason that there is no increase in the class from >50 mm to <200 mm is based on the fact that the used statistical method for simulation is not able to generate precipitation values higher than in the past. It is only possible to simulate the past extreme precipitation events more frequent. Extreme precipitation like 2002 is not covered by the statistical climate projections but change in the probability density functions is possible.

Table 1 contains the mean annual and summer precipitation sums for the past and the two future scenarios. In general, there is a reduction in both scenarios especially for the summer precipitation.

Table 1. Mean annual and summer (JJA) precipitation sums [mm] in the past and future for the station Chemnitz

Time series	mean precipitation sum	
	year	summer
	mm	mm
1971-2000	705	258
1993-2003	735	262
2091-2100 A2	721	227
2091-2100 B1	665	245

3.2.2 *Changes in summer temperature*

Besides precipitation, temperature is the most important element by analyzing the future climate change. The two maps of Saxony in figure 4 show the mean temperature trend in Kelvin for the summer season of the decades 2041-2050 and 2091-2100. It can be seen that there is an increase in temperature for the whole Saxon region for both scenarios. This increase is more distinct in the north-western lowlands (both decades) and the Elbe River basin (2091-2100).

For the decade 2041-2050 (B1), the summer temperature increase ranges between 0.8° C and about 1.4° C and has a mean of 1.2° C for the entire area. Concerning the Upper Mulde catchment, the temperature shows an increment of about 1.0° -1.2° C. The decade 2091-2100 (B1) is denoted by a further temperature increase up to a mean of 2.2° C and a range from 2.0° C to 2.4° C while the area of the Upper Mulde is again a region with relatively low increase (2.0°-2.2° C). In the Saxon lowlands of the Elbe River basin, the highest values of about 2.4° C can be found.

Also for the temperature analysis the station Chemnitz has been selected as an example. The relative frequencies of the daily mean summer (JJA) temperature are shown in figure 3 for two past time series and for the decade 2091-2100 of the scenarios A2 and B1.

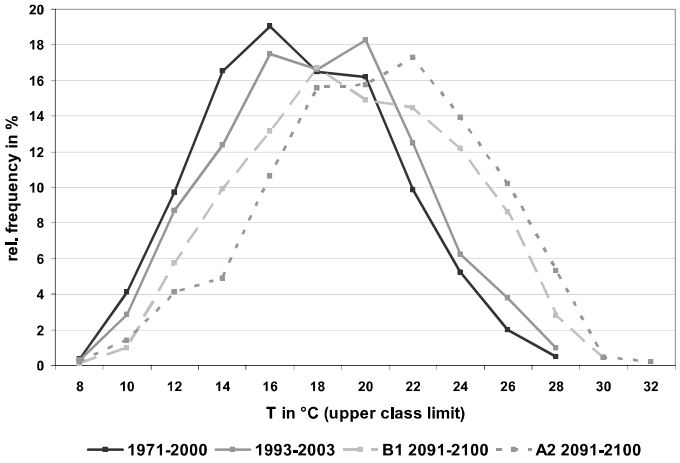

Figure 3. Relative frequency [%] of the mean summer (JJA) temperature at the station Chemnitz

In evidence, there is a clear tendency to higher temperatures. While the maximum temperature for the past time series are 27.4 °C and 27.7 °C, respectively, the maximum temperature for scenario A2 is 30.8 °C and 29.2 °C for scenario B1. This is an increase of around 12 %. The temperature with the highest relative frequency is shifted from the class 14-16 °C (1971-2000) to the class 18-20 °C (B1) and 20-22 °C (A2) respectively. Furthermore, it can also be seen that the number of warm days with a mean temperature > 20 °C will increase. In spite of these three facts, in future, there will still be cold days like in the past where the minimum mean temperatures were 6.8 °C and 7.0 °C respectively. The minimum temperatures for the scenarios are 7.9 °C and 7.0 °C. But the number of days colder than 18 °C will be reducing in the future.

These trends are already observable by comparing the two past time series 1971-2000 and 1993-2003.

4 CHANGES IN THE RETURN PERIOD OF PRECIPITATION EVENTS

4.1 *Methodic basics*

For the estimation of a possible future spatio-temporal development of statistical heavy precipitation using the statistic of extremes a multiple regression model based on weather patterns has been built up. Generally, projected time series of precipitation were not used because until now they are associated with high uncertainties. The model is based on a statistical relation between the parameters of the distribution function of extreme values (Gumbel distribution) and variable frequency distribution of regional classes of weather patterns. The time series of the weather patterns were generated using an objectified classification method on the basis of meteorological predictor fields [NCAR/ NCEP-Reanalysis (Kalny et al. 1996), ECHAM5 / MPI-OM T63L31-Simulations (A2 and B1)]. Changes in the distribution of the weather patterns were utilized to design changes of the distribution parameters of future time slices compared to a reference period (1951-2000).

Equation 1 shows the Gumbel-Distribution transformed as a linear equation. To calculate the future return period for a statistical heavy precipitation this equation has to be solved for T (Eq. 2).

$$SHP(D,T,t) = u(D,t) + w(D,t) * \left(-\ln\ln\frac{T}{T-1} \right) \qquad (1)$$

with T > 1a;

where SHP = statistical, heavy precipitation [mm]; D = duration; T = current return period [a]; t = time slice (reference period); u, w = parameters of the Gumbel-Distribution

$$T'(D,t') = \left(1 - \left(\exp\exp\frac{u'(D,t') - SHP(D,T,t)}{w'(D,t')} \right)^{-1} \right)^{-1} \qquad (2)$$

where T' = future return period [a]; t' = future time slice (reference period); u', w' = parameters of the Gumbel-Distribution of the scenarios.

The comparison of calculations on the basis of measurements versus the control run (Fig. 4) shows that the characteristic of heavy precipitation is strong correlated with circulation pattern.

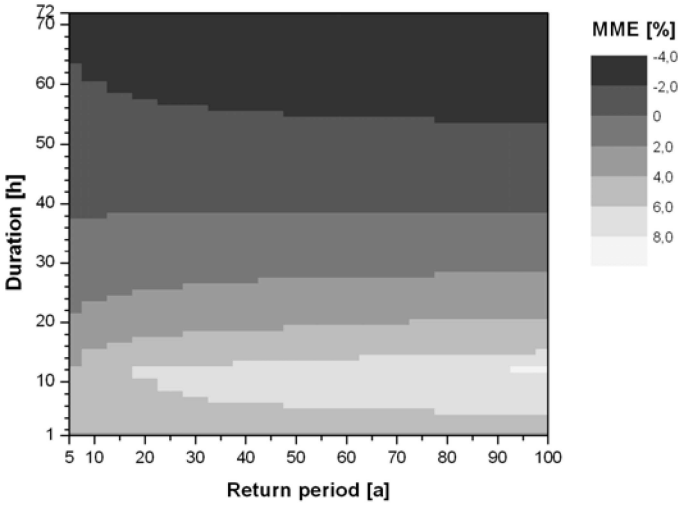

Figure 4. Mean Model Error [%] concerning return periods of 5-100 yrs and durations of 1 h to 3 d

4.2 *Return period changes of the SHP(24h,100a,1951-2000)*

In this section, the changes of the return period are investigated exemplarily for the current precipitation event SHP(24h,100a,1951-2000).

To calculate the changes, the mean return period was computed for the central year of a 30 years running period (decade wise) between 2011 and 2100 (Fig. 5). There, the considered time period is the vegetation period from May to September.

Figure 5 clarifies a decrease in the return period. For scenario B1 the mean decrease is from about 75yrs (2025) to about 68 yrs (2085). For the A2 scenario it decreases from around 76 yrs to 65 yrs. Concerning both scenarios, this means that such an event with a current return period of 100 yrs and a duration of 24 h occurs more and more often in the future.

This reducing return period is probably also a result of the increasing occurrence of rainfall events with a short duration, e.g. convective events with a duration of few hours (cf. Section 4.2.1).

The distinctive leap of about 25 yrs between the current value (100 yrs) and the first value of the scenarios (75 / 76 yrs) results from several possible reasons:

- The current return period was calculated for 50 years (1951 – 2000).
- The ten years between 2001 and 2010 are missing
- The trends concerning the changes in summer temperature (warming) and precipitation (increase in heavy precipitation) are already observable in the comparison of the two past time series (cf. Fig. 2 and 3).
- The model has a mean error of 2.0-4.0 % for an event with a duration of 24 h and a return period of 100 years (cf. Fig. 4).

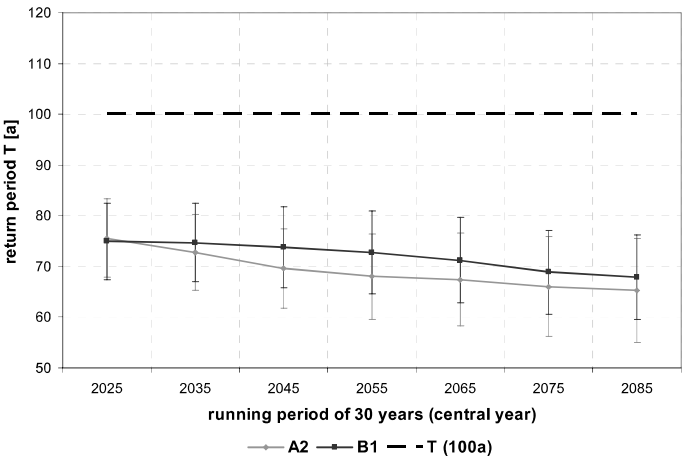

Figure 5: Changed return period of SHP(24h,100a) for 1951-2000, vegetation period (may-sep), catchment area "Zwickauer Mulde" and "Freiberger Mulde"

5 CHANGES IN THE MAXIMUM POSSIBLE PRECIPITATION AMOUNT IN SAXONY

A comprehensive multiscale simulation approach is beyond the scope of this section. Nevertheless, to gain at least some tentative statements about the impact of climate change on extreme weather events, an epignostic sensitivity study of the century flood of the river Elbe in August 2002 is performed.
The simulations were performed using the model COSMO-DE Version 4.2 (the former Lokal-Modell), which is the NWP model the Deutscher Wetterdienst (DWD) (Schättler & Doms 2002). The model domain covers the northern part of Central Europe with an area of approximately 565 x 565 km² and a horizontal grid resolution of $\Delta x \approx 2.8$ km (number of horizontal grid points: 201 x 201, number of vertical layers: 45, grid resolution in geographical coordinates: 0.025°). The options for the physical parameterizations were the same as the one used in operative model runs. To initialize and force the COSMO-DE simulations special reanalysis data, generated by the DWD for this flood event (model LMQ), were used. The model was initialized at August 12, 00 UTC. Model integration time was 30 hours. The predicted 24 h-rain sum was evaluated in the time interval from 00+06 UTC until 00+30 UTC. Within the framework of a sensitivity study several model runs with modified initial and boundary conditions were performed (respective constant offset of temperature and water vapor mixing ratio to the LMQ reanalysis data).

The preliminary results can be summarized as follows (cf. Tab. 2):

- The observed rainfall pattern, especially the location of the maximum is well reproduced by the reference case simulation. However, the observed total maximum was underestimated by ca. 70 - 100 mm.
- An alteration of the thermo-humid initial and boundary conditions is accompanied by a change of the flow conditions. This may result in a change of the location and intensity of hydro-thermodynamic structures such as fronts, air mass internal convergence zones, convective updrafts etc.
- A temperature increase leads to a decrease of the total rain sum due to an enhanced storage capacity for atmospheric water vapor, ensuring longer lasting sub-saturated conditions (case ID02).
- Owing to the character of the underlying physical equations, the model system does not respond linearly to a change of the initial and boundary conditions. In dependence of the corresponding change of the storage capacity for atmospheric water vapor, constants offsets of temperature and humidity can decrease or enhance the resulting rain amount. In one case this results in a superposition, in another case in a displacement or splitting of dynamic and orographic lifting zones, the latter leading to the weakening of rain maxima and the appearance of new maxima.
- The present simulations insinuate a tendency of an overall enhancement of the rain sum for an increase of the water vapor mixing ratio above a certain threshold. Thus, the relative humidity must exceed the value of the reference run.
- The total rain integrated over all grid points of the model domain reveals the following features:
  - Keeping the water vapor mixing ratio constant, the total amount of precipitation decreases for a higher temperature (ID02). This case corresponds to an effective decrease of the relative humidity.
  - The cases with nearly constant relative humidity provide nearly the same (ID03) or small decreasing (ID07) amount of overall precipitation, respectively. The increased amount of atmospheric water vapor leads to higher conversion into precipitation in the model domain. Thus, with respect to the total rain sum, the local decrease of rain sum over the Ore Mountains due to the displacement between hydro-thermodynamic and orographic lifting zones is overcompensated by a higher availability of atmospheric water vapor. As expected, a further increase of the water vapor mixing ratio at the same temperature leads to a higher overall precipitation. This case corresponds to an effective increase of the relative humidity.

Table 2. Maximum local 24h-rain sums in the whole model domain and in the Ore Mountains region in dependence of constant offset of temperature and water vapor mixing ratio

Run ID	T offset	Mixing ratio offset	Max. local 24h-rain	Max. local 24h-rain OM*	Change in integr. rain sum
	K	%	mm	mm	%
01	0	0	230-240 (OM)	230-240	-
02	+ 2	0	180-190 (OM)	180-190	- 23.6
03	+ 2	+ 10	190-200 (OM)	190-200	- 4.4
04	+ 2	+ 15	190-200 (OM)	190-200	+ 4.3
05	+ 2	+ 20	240-250 (BB*)	190-200	+ 11.7
06	+ 2	+ 40	>450 (BB)	190-200	+ 28.4
07	+ 4	+ 20	210-220 (BF*)	170-180	- 11.4
08	+ 4	+ 30	230-240 (BB)	160-170	+ 5.6
09	+ 4	+ 40	330-350 (BB)	200-210	+ 17.6

* OM = Ore Mountains; BB = Brandenburg; BF = Bohemian Forest

The bold printed run ID 01 represents the "undisturbed" reference case and ID 03 and 07 correspond to nearly constant relative humidity.

Thereby, it is important to consider that under these changed climate conditions a quite different dynamic is developing and such a weather pattern like in August 2002 would maybe not occur. Furthermore, the results have to be interpreted with regard to the fact that this changing of the climate and boundary conditions is a rigorous interference in the model physic and hence does not mandatory produce realistic conditions and results.

6 CONCLUSIONS

The aim of the work presented was to analyze the future climate change in Saxony, its impact on return period and on the maximum possible rainfall amount over Saxony.

The analysis of the climate change for the summer period in Saxony shows a general trend of decreasing precipitation and increasing temperature. For the decade 2091-2100 of the SRES scenario B1 this results in a mean precipitation decrease of 21 % and a mean temperature increase of 2.2 °C. These trends are not equal over the whole region. For the Upper Mulde catchment they are less distinct and in the Saxon lowlands they show the highest values.

As an example the station Chemnitz was analyzed more detailed. It was shown that the relative frequency of days without precipitation as well as for days with high precipitation increases. Concerning the changes in temperature, the relative frequency shows a trend to higher temperatures and more warm days while the number of cold days decreases. But there are still cold days. The class with the highest relative frequency is shifted to warmer temperatures.

It is pointed out that these precipitation and temperature trends are already observable by comparing the two past time series 1993-2003 and 1971-2000.

From these climate change analysis result an increasing future occurrence probability of summer rainfall events with high intensities, e.g. convective cells, what causes a higher risk concerning flash floods. Furthermore, the climate change will lead to an increased occurrence probability of warm, hot and dry days as well as droughts.

In Section 5 the changes in the return period of a precipitation event with a duration of 24h and a current return period of 100 yrs was investigated. The results show a decrease in the return period of up to 32 yrs for scenario B1 and 35 yrs for scenario A2. Concerning both scenarios, this means that such an event will occur more often in the future what is probably partly a result of the increasing occurrence of short duration rainfall events like convective cells.

Additional work investigated the impact of climate changes on the maximum possible rainfall amount. This was realized by using the model COSMO-DE Version 4.2. Within the framework of a sensitivity study several model runs for the 2002 Elbe flood event were performed with modified initial and boundary conditions concerning a constant offset of temperature and water vapor mixing ratio. Thereby, it was shown that these offsets have a high influence on the model dynamic as well as on the resulting rain field structure and amount. It was figured out that a temperature increase leads to a decrease of the total rain sum due to an enhanced storage capacity for atmospheric water vapor. In dependence of that, constant temperature and humidity offsets can decrease or enhance the resulting rain amount. This results in a superposition, in a displacement or splitting of dynamic or orographic lifting zones what leads to the weakening of rain maxima and appearance of new maxima.

By keeping the water vapor mixing ratio constant, the total rain amount decreases for higher temperatures. The runs with nearly constant relative humidity provide nearly the same rainfall amount.

These results have to be always considered under the aspect that it is uncertain whether such a weather pattern like 2002 would occur under these changed climate conditions.

Acknowledgements

The study presented in this paper was funded by the Integrated Project FLOOD*site* (EC, Contract-No. GOCE-CT-2004-505420).
Furthermore, the measured data were provided by the Deutscher Wetterdienst (German Weather Service).

References

Bartels, H., Dietzer, B., Malitz, G., Albrecht, F.M. & Guttenberg, J. 2005. *Kostra-DWD-2000: Starkniederschlagshöhen für Deutschland (1951-2000)*. Deutscher Wetterdienst, Offenbach.

Bernhofer, C., Franke, J., Goldberg, V., Seegert, J., & Küchler, W. 2006. Regional climate change – To be included in Future Flood Risk Analysis? In: Schanze, J., Zeman, E. & Marsalek, J. 2006. *Flood Risk Management: Hazards, Vulnerability and Mitigation Measures*. 91-100, Springer 2006

Doms, G. & Schättler 2002. A Description of the Nonhydrostatic Regional Model LM – Part I: Dynamics and Numerics. http://www.cosmo-model.org

Enke, W. & Kreienkamp, F. 2005. *Abschlußbericht: Bereitstellung regionaler Klimaszenarien für die regionale Klimadiagnose und Prognose im Teilprojekt*. Meteo-Research, Stahndorf

Enke, W., Schneider, F. & Deutschländer, T. 2005. A novel scheme to derive optimized circulation pattern classifications for downscaling and forecast purposes. *Theor. Appl. Climatol.* 82: 51-63.

IPCC (Intergovernmental Panel on Climate Change) 2001. *Climate Change 2001 – The Scientific Basis – Contribution of Working Group I to the Third Assessment Report of the Intergovernmental Panel on Climate Change (IPCC)*. Cambridge.

Kalny, E., Kanamitsu, M., Kistler, R., Collins, W., Deaven, D., Gandin, L., Iredell, M., Saha, S., Whitea, G., Woolen, J., Zhu, Y., Chelliah, M., Ebisuzaki, W., Higgins, W., Janowiak, J., Mo, K., Ropelewski, C., Wang, J., Leetmaa, A., Raynolds, R., Jenne, R. & Joseph, D. 1996. The NCEP/ NCAR 40-year Reanalysis Project. *Bull. Am. Met. Soc.* 77: 437-471.

Kreienkamp, F. & Spekat, A. 2007. IDP2006 – Ein Werkzeug zur exploativen Datenanalyse, Bedienungsanleitung. CEC Potsdam GmbH

Munich Re Group 2005. Weather catastrophes and climate change. Is there still hope for us? Münchener Rückversicherung-Gesellschaft, München, Germany

UBA (Umweltbundesamt) & MPI-M (Max-Planck-Institut für Meteorologie) 2006 Künftige Klimaänderungen in Deutschland – Regionale Projektionen für das 21. Jahrhundert. Hintergrundpapier. ww.umweltbundesamt.de/uba-info-presse/hintergrund/Klimaaenderungsworkshop.pdf

Appendix E

Additional publication 2

Satellite observation of storm rainfall for flash-flood forecasting in small and medium-size basins

C. Görner, N. Jatho & C. Bernhofer
Technische Universität Dresden, Institute of Hydrology and Meteorology, D-01062 Dresden, Germany

M. Borga
Department of Land and Agroforest Environments (MB), Agripolis, University of Padova, 35020 Legnaro, Italy

ABSTRACT: The satellite meteorology team of the TU Dresden developed a "Structured Algorithm System" (SAS) for quantitative precipitation estimation (QPE) based on the highly resolved geostationary satellite data of Meteosat-6 and Meteosat-8. The SAS is used for detecting extreme storm rainfall at the spatial and temporal scales of interest for flash-flood analysis and prediction. Within this algorithm, several techniques for estimating rain rates are applied. The satellite derived rain rates are corrected concerning orographic situation, the wind and moisture conditions and the cloud growth rate by using additional data like MPEF products and radiosondes. Furthermore, they are compared and analyzed statistically in relation to radar data. The results are presented for an example of a flash-flood in the Trentino Alto Adige region in the Italian Alps which occurred in July 2005.

1 INTRODUCTION

Flooding – including flash floods – as a result of heavy or long-lasting precipitation is the most widely distributed of all natural hazards across Europe, causing distress and damage wherever it happens. Hence, there is a high need of realtime detection of rain fields and determination of the rain rates to be able to forecast the possible flood risk.
Concerning ground based historical rainfall observations with rain gauges, only radar measurements are able to observe heavy rainfall events temporal and spatial highly resolved. Despite the increasing density of radar networks covering Europe, radar measurements will ever be limited (e.g. in mountain regions, ocean...). Thus satellite data are more and more used to improve rainfall estimations (Grassotti et al. 1998, Lakshmanan et al. 2006). The problem comparing radar and satellite measurements is based on the satellite platform itself as well as on the technical features of instruments. But as a result of the increasing technical progress in last decades the space borne rainfall measurements were improved (Petty 1995, Levizzani et al. 2002, Lang et al. 2003, Ebert et al. 2007) and applied to several events (Vicente et al. 1998, Bendix et al. 2001).
The aim of the work presented was to develop a Structured Algorithm System (SAS) for Quantitative Precipitation Estimation (QPE) for detecting extreme storm rainfall by using highly resolved geostationary satellite data. This has been realized by building up a twofolded SAS, one part based on Meteosat-6 Rapid Scan data (M6/RS-SAS) and the second part based on Meteosat-8 data (MSG-SAS). Both parts include several rainfall estimation techniques. The satellite derived rain rates are corrected concerning the orography, the wind and moisture conditions and the cloud growth by using additional data like MPEF products and radiosondes. And furthermore, they were compared and analyzed statistically in relation to radar data.

2 DATA

2.1 *Meteosat-6*

Meteosat-6 is the sixth satellite of the first generation of the meteorological geostationary satellites operated by the European Organisation of the Exploitation of Meteorological Satellites (EUMETSAT).

Meteosat-6 carries the MVIRI (Meteosat Visible and Infrared Imager) which is able to detect the emissions of three spectral wavebands (Tab. 1).

The data are recorded every 30 minutes for the full earth scan (Full Disk) and every 10 minutes for Europe (Rapid Scan data, available since 01/2002). The Sub-Satellite-Point (SSP) resolution adds up to 5 x 5 km² (WV, IR) and 2.5 x 2.5 km² (VIS) (EUMETSAT 2003). Since 4th April 2003 all Rapid Scan imagery are rectified to 10° East and all previously imagery were rectified to 0°, because of the changed position of Meteosat-6 to 10° East. The im-

ages are adjusted by EUMETSAT and provided by the EUMETCAST service. The calibration of the Meteosat-6 IR, WV and VIS channel is done by EUMETSAT.

Table 1. Spectral wavebands of Meteosat-6 (EUMETSAT 2000)

Channel	Measuring range µm	Main gaseous absorber or window
VIS	0.45 – 1.0	Window
IR	10.5 – 12.5	Window
WV	3.7 – 7.1	Water vapor

2.2 *Meteosat-8*

Meteosat-8 is the first satellite of Meteosat Second Generation (MSG) and is therefore also called MSG-1. It was launched in 2002, has a nominal position at 0° and is sending data operationally since January 2004. It carries the Spinning Enhanced Visible and Infrared Imager (SEVIRI) which observes the full disk of the earth with a repeat cycle of 15 minutes in 12 spectral channels (Tab. 2). The channels 1-11 have a spatial resolution of 3 x 3 km² at the Sub-Satellite Point (SSP) and channel 12 (High Resolution Visible, HRV) has a spatial resolution of 1 x 1 km² (SSP). The calibration of the Meteosat-8 channels is done by EUMETSAT, too (EUMETSAT 2006b).

Table 2. Spectral channel characteristics of Meteosat-8 (Schmetz et al. 2002)

Channel		Measuring range µm	Main gaseous absorber or window
1	VIS 0.6	0.56 – 0.71	Window
2	VIS 0.8	0.74 – 0.88	Window
3	NIR 1.6	1.50 – 1.78	Window
4	IR 3.9	3.48 – 4.36	Window
5	WV 6.2	5.35 – 7.15	Water vapor
6	WV 7.3	6.85 – 7.85	Water vapor
7	IR 8.7	8.30 – 9.10	Window
8	IR 9.7	9.38 – 9.94	Ozone
9	IR 10.8	9.80 – 11.8	Window
10	IR 12.0	11.0 – 13.0	Window
11	IR 13.4	12.4 – 14.4	Carbon dioxide
12	HRV	about 0.4 – 1.1	Window / water vapor

2.3 *Radar*

The used radar data of the Italian investigation area were delivered by the co-operation partner University of Padova. This area is located in the Trentino-Alto Adige region in the north-eastern Italian Alps (Fig. 1). The data used were collected by the C-band radar station Monte Macaion. The region covered by radar ranges the areas from 200 m a.s.l to 3900 m a.s.l. (Tonelli et al. 2003). The radar data used from the Monte Macaion station have a temporal resolution of 5 minutes and a spatial resolution of 1 x 1 km².

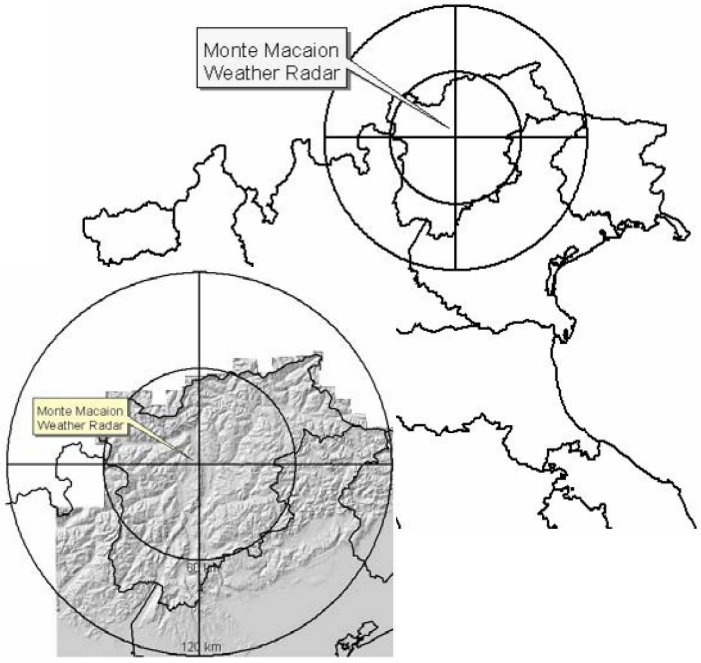

Figure 1. Position of Monte Macaion weather radar (right) and its surrounding topography (left) (Tonelli et al. 2003)

2.4 *Additional data and rain rate correction*

2.4.1 *M6/RS-SAS*

At regular intervals many meteorological products (e.g. Meteorological Products Extraction Facility - MPEF) are generated from the Meteosat image data (EUMETSAT 1996). The spatial resolution of MPEF products depends on the distribution per segments. One segment consists of 32 x 32 infrared pixels and a matrix of 80 x 80 segments covers the complete field of view. The MPEF-products Cloud Analysis (CLA), Cloud Motion Winds (CMW) and Upper Tropospheric Humidity (UTH) are integrated in the M6/RS-SAS.

Some satellite based rainfall estimation techniques include a moisture correction factor (PWRH) as a product of precipitable water (PW) for entire sounding and relative humidity (RH) as the UTH value. (Vicente et al. 1998, Ba & Gruber 2001). Further used radiosonde values are Convective Available Potential Energy (CAPE), level of free convection (LFC) as well as the temperature and pressure of the lifted condensation level.

For taking into account the effects of the 3D structure of the terrain (e.g. windward-lee-effects) a rainfall multiplier is applied. It increases or reduces the derived rain rates depending on the orographic information and the wind conditions.

2.4.2 *MSG-SAS*

For two of the four applied methods the moisture correction factor PWRH using radiosonde data and a cloud growth rate correction factor have been integrated in the MSG-SAS. The cloud growth correction is realized by comparing pixel wise the IR-temperatures of two consecutive images based on two assumptions: 1) a decrease in temperature denoting the growing of the cloud and increasing rain rates; 2) an increase in temperature denoting the decaying of the cloud and decreasing rain rates.

From the image data various MPEF and SAF (Satellite Application Facility) products are generated which could be useful for the correction and validation of the estimated rain rates

The MPEF products (e.g. Atmospheric Motion Vectors, Tropospheric Humidity) are regularly produced, archived and distributed by EUMETSAT. They have a spatial resolution of 1° x 1° and different temporal resolutions (e.g. 15 min, 1 h, 3 h).

The SAF products (e.g. Precipitating Cloud, Convective Rainfall rate) are mainly distributed to users on demand, either as finalized products or as product extraction algorithm software packages for which a license is needed. The SAF have a spatial and temporal resolution equivalent to the MSG data resolution.

Both product types are encoded in the very complex and compressed BUFR (Binary Universal Form for the Representation of meteorological data) and GRIB II (GRIdded Binary II) data format. To use them special decoder are needed which do not work under Windows. MPEF as well as SAF could not be included in the MSG-SAS within the FLOOD*site* project because of problems with the required license and the data formats.

3 IMPLEMENTED METHODS

3.1 *M6/RS-SAS*

To simplify matters first analyses were made by using Rapid Scan data because of their reduced spectral information of three channels in comparison to Meteosat-8 data and its spectral information of 12 channels. To derive rain rates from the satellite data the following methods are included:

- Griffith-Woodley Technique (Negri et al. 1984, Negri & Adler1993)
- Auto-Estimator Technique (AE) (Vicente et al. 1998)
- GOES Multispectral Rainfall Algorithm (GMSRA) (Ba & Gruber 2001)
- Technique after Grose (Grose et al. 2002)
- Enhanced Convective Stratiform Technique (ECST) (Reudenbach 2003, Bendix et al.2001)
- Combined Method after Jatho

3.2 *MSG-SAS*

The following four algorithms for rainfall estimations are implemented in the MSG-SAS:

- Enhanced Convective Stratiform Technique
- Auto-Estimator Technique
- GOES Mutlispectral Rainfall Algorithm
- Method after Kurino (Kurino 1997a, 1997b)

4 CASE STUDY

4.1 *Research area and event characteristic*

As already mentioned in section 2.3 the exemplarily investigation area is located in the Trentino-Alto Adige region in the north-eastern Italian Alps (Fig. 1). The relief heights of the radar covered region range between 200 m a.s.l to 3900 m a.s.l., corresponding to the highest mountains in north-eastern Italy (Tonelli et al. 2003). The region is classifiable as an Alpine high-mountainous area (Delrieu 2006). The examined event was a convective precipitation event in the Val Pusteria. It occurred in the afternoon of 18th July 2005, implicated some heavy thunderstorms, had a duration of about four hours, and had a direction of tension from west to east.

The event was analyzed between the period from 14:30 UTC to 15:30 UTC and for the time step of 14:30 UTC concerning the quality and quantity of satellite derived rain rates comparing to radar measurements. Figure 2 shows exemplarily the radar measurement for the selected time step.

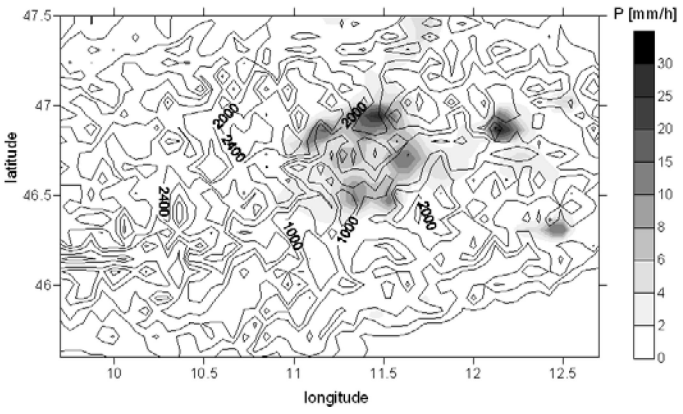

Figure 2. Radar derived rain rates, Val Pusteria, 18th July 2005, 14:30 UTC

The radiosonde data of Udine at 12.00 UTC delivered the required additional data relative humidity and precipitable water for the PWRH correction. At that point of time the relative humidity between surface and the 500 hPa level was 61.85 %. The precipitable water for the entire sounding was 1.44 inches. That results in a PWRH factor of 0.89 what leads to a reduction of the estimated rain rates.

4.2 *M6/RS-SAS*

The tested satellite techniques are the Auto-Estimator as a simple way to derive rain from cloud top temperature, the ECST developed for Europe (Fig. 3), the modified ECST as well as the new developed Combined Method (Fig. 4).

A first comparison between the radar measured rain and Auto-Estimator, ECST and Combined Method derived rain rates (without any additional rainfall correction) is done. For the comparisons, the radar data are used as reference. Concerning Baumgartner & Liebscher (1996) the threshold to define heavy rainfall is about 10 mm/h. This value is used to differentiate between radar measured rain considered as flash flood relevant or not.

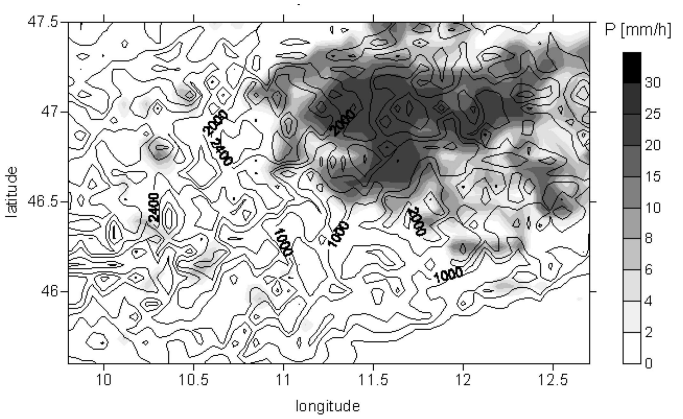

Figure 3. ECST derived rain rates without rainfall correction, Meteosat-6, Val Pusteria, 18th July 2005, 14:30 UTC

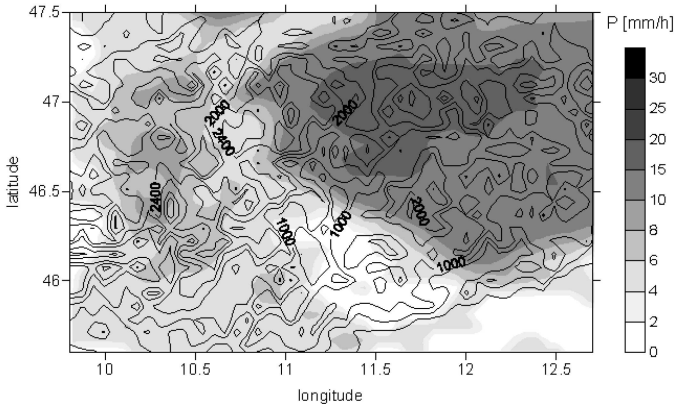

Figure 4. Combined Method derived rain rates without correction, Meteosat-6, Val Pusteria, 18th July 2005, 14:30 UTC

On consideration of the extension of rain areas and their rain rates, large differences between radar and satellite data are shown. Particularly in the north-east part of the investigated area the satellite data yield more precipitation. There, the area of radar measured rain is limited by the range of radar station itself.

A further comparison of radar and satellite data shows a spatial offset. The offset maybe caused by a relocation of rainfall derived via satellite at the cloud top and measured at surface.

Comparing the several satellite derived rain, differences between the techniques become apparent. Concerning the marginal information used as input for the Auto-Estimator the rain rate are lower than for the complex method ECST. The Combined Method combines the features of several techniques. Thus the method is able to derive higher rain values following an area of maximized extension.

The impact of orography as well as current wind situation of satellite derived rain rates using a rain multiplier is done exemplarily for the ECST (FIG. 5) and the Combined Method (Fig 6). It is shown that the rain multiplier increases and reduces the satellite derived rain rates in regions of distinct orography. The intensification of rain rates using the multiplier is caused by the high wind speed of 10.1 to 11.0m/s. The spatial outline of satellite derived rain depends on the small range of tested surrounding pixels (3 x 3 environment) used for determination of the rain multiplier. Thus the orographic attributes are considered well and the areas of increased or reduced satellite rain are very local.

A comparison of the satellite techniques with and without rain correction in account with radar measured rain represents still an underestimation for the simple Auto-Estimator. In contrast, the ECST, the modified ECST as well as the Combined Method overestimate the radar measurements.

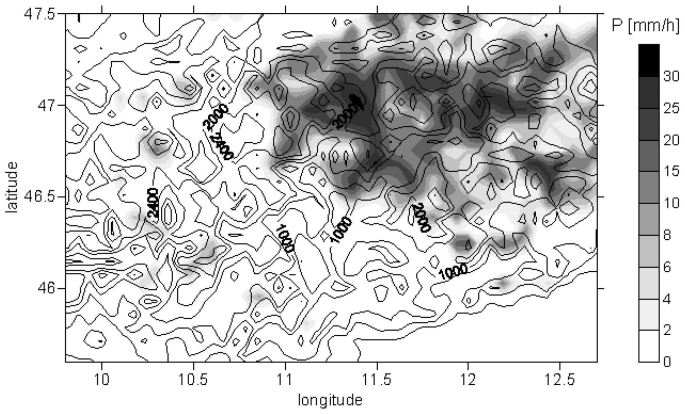

Figure 5. ECST derived rain rates with rainfall correction, Meteosat-6, Val Pusteria, 18th July 2005, 14:30 UTC

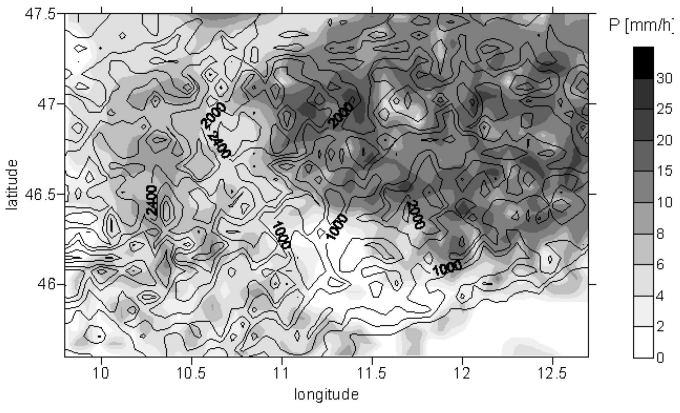

Figure 6. Combined Method derived rain rates with rainfall correction, Meteosat-6, Val Pusteria, 18th July 2005, 14:30 UTC

Exemplary for the period 14:30-15:30 UTC the statistic, represented by the minimum (Min), maximum (Max), mean (Mean), standard deviation (SD) and standard error (SE) of differences, is given in Table 3.

Table 3. Statistic for the comparison of Meteosat-6 and radar derived rain rates of 18th July 2005, 14:30-15:30 UTC

Statistical	simple AE		ECST			Comb. Meth.	
value	nc*	c*	nc	c	m*	nc	c
Min [mm/h]	-17.8	-17.8	-17.9	-17.8	-17.9	-17.4	-17.5
Max [mm/h]	-1.7	-1.1	5.3	6.7	24.3	4.9	6.1
Mean [mm/h]	-7.8	-7.7	-5.7	-5.3	2.2	-1.6	-1.6
Mean [%]	-55.3	-54.9	-39.4	-36.4	21.8	-7.7	-7.9
SD [mm/h]	3.9	4.0	5.1	5.6	10.0	5.4	5.6
SE [mm/h]	0.8	0.8	1.0	1.1	1.9	1.0	1.1

* nc = not corrected, c = corrected, m = modified

Comparing the mean values for the time period 14:30-15:30 UTC an underestimation of satellite derived rain as to radar is assigned except for the modified ECST. This is caused by an occurrence of a spatial offset between satellite and radar detected areas. This offset results probably from a relocation of satellite derived rainfall at the cloud top and ground measured rain. Hence it is possible that the satellite derived rain rates at the cloud top differ in spatial allocation to the radar measured rain.

A further factor for spatial offset between the satellite and radar rain field is based on the limitation of radar measurements depending on the range of the radar station. Therefore, in contrast to the satellite the field of view of radar is limited. Thus a comparison between flash flood relevant radar rain rates (>= 10mm/h) and satellite derived rain shows an underestimation for the satellite.

4.3 *MSG-SAS*

For statistical analysis the radar data >= 10 mm/h were again selected. Then the differences of them and the corresponding satellite data were calculated.

For the comparisons of the results this satellite scan was chosen who was temporal the closest to the radar time. In contrast to Meteosat-6 the time stamp of a Meteosat-8 picture denotes the start of the scan of this picture (EUMETSAT 2006a). The scan always starts in the south-east (South Pole) and takes about 13 minutes till its end in the north-west (North Pole). So after about 9 and 10 minutes north Italy is scanned.

For the methods Auto-Estimator and GMSRA the moisture correction factor PWRH (0.89) and the cloud growth rate correction are applied.

Figure 7 gives an impression of the satellite derived rain rates using the ECST for 14:30 UTC. Further, the Figures 8 shows the corresponding rain rates for the Auto-Estimator without any correction. The effect of the moisture and growth correction is given in Figure 9 for the Auto-Estimator.

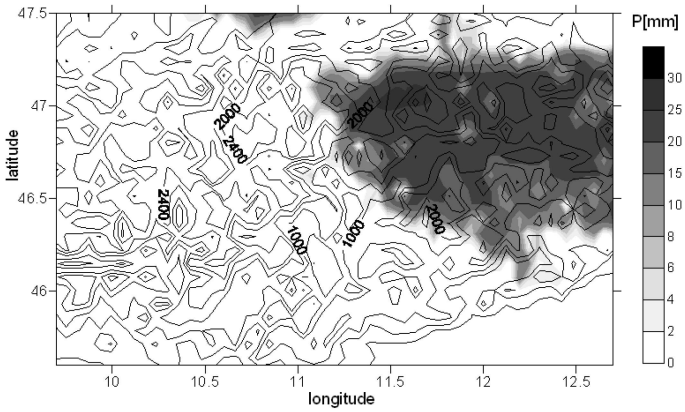

Figure 7. ECST derived rain rates, Meteosat-8, Val Pusteria, 18th July 2005, 14:30 UTC

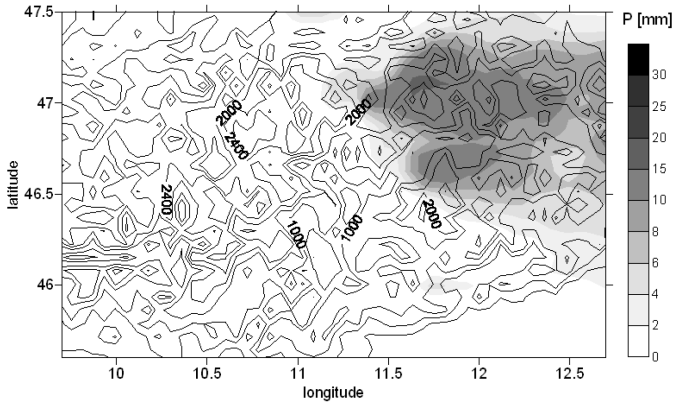

Figure 8. Auto-Estimator derived rain rates without correction, Meteosat-8, Val Pusteria, 18th July 2005, 14:30 UTC

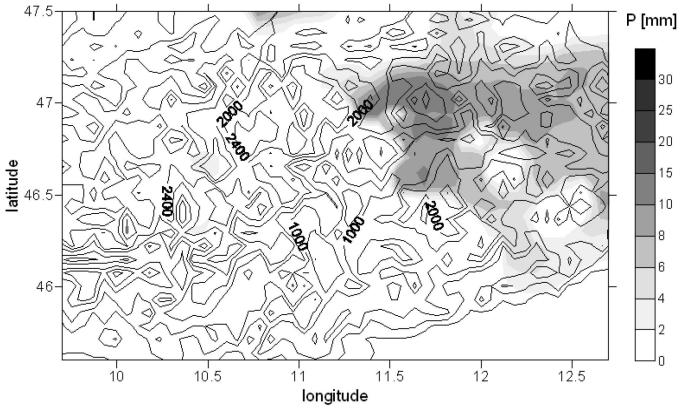

Figure 9. Auto-Estimator derived rain rates with moisture and growth correction, Meteosat-8, Val Pusteria, 18th July 2005, 14:30 UTC

It can be seen that there are big differences between the radar and satellite derived rain rates and also between the four satellite estimation techniques and their modifications. These differences concern the range of the rain rates as well as the size and location of the rain field area. The rain field area de-

rived by radar is only partly covered by the satellite derived rain rates but the satellite rain field is much bigger and relocated in the north-east of the researched area. However, the areas with the highest rain rates are situated near the highest radar rain rates. Thus a spatial offset is distinguishable. For the four algorithms the maximum rain rate varies from 7.6 mm/h (Kurino) to 32.3 mm/h (GMSRA) while the maximum of radar rain rates is 31.5 mm/h. There is a tendency of the satellite estimation techniques to underestimate the radar rain rates of these grid cells having rates >= 10 mm/h. This results in negative values for the means (Tab. 4) of the differences between radar and satellite rain rate. Beside of the absolute and relative mean, Table 4 contains the statistical parameters minimum (Min), maximum (Max), standard deviation (SD) and the standard error of the mean (SE).

Table 4. Statistic for the comparison of Meteosat-8 and radar derived rain rates of 18th July 2005, 14:30-15:30 UTC

Statistical value	AE		ECST	GMSRA		Kurino
	s*	c*		s	c	
Min [mm/h]	-14.0	-15.4	-12.3	-8.6	-19.6	-15.3
Max [mm/h]	30.0	-2.6	13.1	14.3	2.3	-4.5
Mean [mm/h]	-5.0	-9.0	3.2	0.4	-7.9	-9.1
Mean [%]	-39.6	-65.9	23.4	2.6	-57.6	-67.0
SD [mm/h]	7.5	3.3	6.1	5.1	5.0	2.8
SE [mm/h]	1.4	0.6	1.1	1.0	0.9	0.5

* s = simple, c = corrected

The tendency to underestimate is most distinct for the corrected Auto-Estimator and GMSRA what results from the PWRH correction (PWRH < 1.0). For the areas with little or no radar derived rain the satellite techniques tend to an overestimation, especially the simple GMSRA and the ECST. Both tendencies are partly a consequence of the relocation of the satellite rain field. This relocation may results of the different angle of view of the two systems radar and satellite and the different points in time of scanning.

4.4 *Comparison of Meteosat-6 and Meteosat-8*

Further analyses are done comparing Meteosat-6 and Meteosat-8 with regard to the advantages using more spectral information provided by Meteosat-8. The comparison is done for the methods Auto-Estimator and ECST for the 18th July 2005 for the hour 14:30-15:30 UTC and the time step 14:30 UTC.

The rain fields for the time step 14:30 UTC demonstrate similar extensions but differences in the quantity of the rain rates. As already mentioned, a spatial offset between the satellite and radar measurements exists. The offset is not fully explainable and maybe caused by features of the measurement instruments itself. Furthermore, a spatial offset between the two satellite data is noticeable which is maybe caused by the differences in scanning time as a result of the different duration of the repeat cycles.

Concerning the ECST, the analysis demonstrates fewer differences in the detected rain area but high differences in the quantity of rain rates. The Meteosat-8 data represents higher rain rates followed by increased extensions.

Using the rain multiplier for Metosat-6 data increased the quantity of derived rain rates. A comparison clarifies higher rain values for the improved Meteosat-6 data as derived for Meteosat-8.

As well as for the Auto-Estimator, the results of both satellite data for the ECST differ in spatial and quantitative assignment. Using the rain multiplier effects higher rain values for Meteoast-6 data in comparison to Meteosat-8.

Table 5 contains the statistic values of the derived rain rates concerning the radar rain rates >=10mm/h the results of Auto-Estimator and ECST for the time step 14:30 UTC.

Table 5. Statistic for the comparison of Meteosat-6, Meteosat-8 and radar derived rain rates of 18th July 2005, 14:30 UTC

Statistical value	simple AE			ECST		
	M6*		M8*	M6		M8
	nc	c		nc	c	
Min [mm/h]	-17.3	-21.8	-21.8	-12.8	-16.2	-25.4
Max [mm/h]	-0.8	-0.5	-1.0	11.0	13.0	11.2
Mean [mm/h]	-6.6	-6.5	-10.8	1.6	1.1	-7.7
Mean [%]	-44.2	-43.9	-68.1	10.7	7.4	-48.7
SD [mm/h]	4.9	5.2	5.5	8.4	9.7	9.9
SE [mm/h]	1.1	1.2	1.2	1.9	2.2	2.1

* M6 = Meteosat-6, M8 = Meteosat-8

As shown in Table 5 the results for the Auto-Estimator and the ECST for both satellites differ. The Auto-Estimator derived rain rates underestimate the radar measurements. Comparing the results of both satellites, Meteosat-8 tends to underestimate the highest radar rates more than Meteosat-6. For the ECST it can be seen that the Meteosat-6 tends to overestimate radar and Meteosat-8 tends to underestimate again. Possible reasons are the differences in scanning time, the spatial offset between radar and satellite and the filter functions of the input channels.

The statistical values for the analysis of the time span 14:30-15:30 UTC are summarized in Table 6. Considering the Mean values the application of the rain multiplier effects less improvement to derived Meteosat-6 rain rates. The rain multiplier is not able to reach the Mean values of Meteosat-8. This may be due to the feature of Meteosat-6 Rapid Scan data to underestimate the derived rain rates in comparison to Meteosat-8 based on the marginal spectral information of Meteosat-6.

Table 6. Statistic for the comparison of Meteosat-6, Meteosat-8 and radar derived rain of 18th July 2005, 14:30-15:30 UTC

Statistical value	simple AE			ECST		
	M6*		M8*	M6		M8
	nc	c		nc	c	
Min [mm/h]	-17.8	-17.8	-14.0	-17.9	-17.8	-12.3
Max [mm/h]	-1.7	-1.1	30.0	5.3	6.7	13.1
Mean [mm/h]	-7.8	-7.7	-5.0	-5.7	-5.3	3.2
Mean [%]	-55.3	-54.9	-39.6	-39.2	-36.4	-23.4
SD [mm/h]	3.9	4.0	7.5	5.1	5.6	6.1
SE [mm/h]	0.7	0.8	1.4	0.9	1.0	1.1

A comparison of Mean values for both satellites represents an underestimation for the Auto-Estimator which is more distinct for Meteosat-6.

The results of the ECST show a tendency of underestimation for Meteosat-6 and overestimation for Meteosat-8. This overestimation is explainable with the higher extension of the detected heavy rainfall area. Furthermore the application of the ECST to the Meteosat-8 data is not completely clarified until now (Reudenbach 2005). And the effect of this is difficult to discuss.

As a conclusion it can be noted that the results depends on the applied satellite based estimation technique as well as on the used satellite input data (Meteosat-6, Meteosat-8). At least Meteosat-8 offers partly improved rainfall estimations because of its better spatial resolution and the increased spectral information but the estimation techniques have to be adapted to that.

5 CONCLUSIONS

The aim of TU Dresden within Task 15 of the FLOOD*site* project was to develop a satellite based Algorithm System (SAS). The M6/RS-SAS integrates six different satellite rainfall estimation techniques. To improve the results additional data like MPEF products and radiosonde data are implemented. Thus the current wind and the atmospheric condition can be considered.

To consider the influence of orography and current wind situation the investigation area is tested concerning the windward and lee situation. By defining a rain multiplier the satellite derived rain can be increased or reduced.

Based on the integrated satellite methods Auto-Estimator, GMSRA, Grose and ECST a new method called Combined Method was developed and integrated in the M6/RS-SAS.

To validate the satellite derived rain rates radar data from the co-operation partner are integrated. To compare the data for one grid cell the radar data are scaled to satellite resolution.

Both SAS were tested for a case study characterized by very local heavy rainfall.

For the QPE with Meteosat-8 four algorithms have been implemented in the MSG-SAS. For improving the estimated rain rates, radiosonde data are taking into account.

It could be seen that there are big differences between the rain rates derived by radar and satellite. These differences concern the size and location of the rain field area as well as the amount of the estimated rain rates. However, the structure of the radar rain field is partly distinguishable in the satellite estimated rain fields.

All of the used algorithms show a tendency to underestimate the rain rates measured by radar for the grid cells having rain rates >= 10 mm/h. For the areas with less or no radar derived rain a tendency of overestimation is evident for all techniques.

Both tendencies are partly a consequence of the relocation of the satellite rain field. This relocation may result from the different scanning angle of the two systems radar and satellite, the different points in scanning time and processes and influences (wind, moisture,…) between the cloud top and the earth surface.

There are various problems and sources of error causing the discrepancies between the radar and satellite derived rain rates. First of all there is the basic problem that the satellite can only scan the top of clouds and it is unable to see which processes go on inside and below a cloud. Therefore, the rain rates have to be estimated from the temperature and reflectance of the cloud tops.

Another problem is that all of the implemented algorithms were developed for other satellites and/or regions. So they are not applicable to Meteosat-6/-8 without adjustments to their different spectral responses and spatial and temporal resolution.

Differences between the radar and satellite rain rates also result from the different spatial resolution as well as from the different points in time of the measurement and scan.

It can be said that the satellite based estimation of rain rates already shows good approaches but for improving the accuracy in space and intensity it is necessary to adjust the algorithms to the used satellite and region. And there is a need of including additional data like orography, MPEF, SAF, wind data, atmospheric profiles, cloud life cycles and cloud models how it has already been partly done for the M6/RS-SAS.

Further analyses were done comparing the satellite results with regard to the advantages using more spectral information provided by Meteosat-8 data. The comparison was done for the methods AUTO-ESTIMATOR and ECST.

Problems result from the different scanning points in time and the duration of the repeat cycle of

Meteosat-6 Meteosat. This could take effect to the spatial assignment of rain.

Following Negri & Adler (1993), Scofield & Kuligowski (2003) as well as the results of the satellite team of TU Dresden it can not explicitly be said whether satellite estimation techniques under- or overestimate radar measurements. It depends on various conditions (atmospheric conditions, orography, technical features, estimation method,…).

As a conclusion it can be noted that the results depends on the applied estimation technique as well as on the used satellite input data. At least Meteosat-8 is able to offer improved rainfall estimations because of its better spatial resolution and the increased spectral information but the estimation techniques have to be adapted to that.

The project work of TU Dresden pointed out that the satellite based rainfall estimation still includes several uncertainties and require reference data (ground measurements). Nevertheless the satellite derived rain rates provide helpful additional information of researched rainfall areas, particularly in regions low or not covered by ground measurements.

Acknowledgement

The study presented in this paper was funded by the Integrated Project FLOOD*site* (EC, Contract-No. GOCE-CT-2004-505420).

References

Ba, M.B. & Gruber, A. 2001. GOES Multispectral Rainfall Algorithm (GMSRA). *Journal of Applied Meteorology* 40: 1500-1514.

Baumgartner, A. & Liebscher, H.J. 1996. *Allgemeine Hydrologie - Quantitative Hydrologie.* Gebrüder Bornträger, Berlin-Stuttgart.

Bendix, J., Reudenbach. C., Taschner, S., Ludwig, R. & Mauser, W. 2001. Retrieval konvektiver Niederschläge in Mitteleuropa mit Fernerkundungsdaten und Modellen. *DLR Mitteilungen 2001-02*: 69-78.

Delrieu, G. 2006. Requirements for Flash Flood Hydrometeorological Monitoring. *FLOODsite Project Report*, T23-06-01.

Ebert, E., Janowiak, J.E. & Kidd, C. 2007. Comparison of Near-Real-Time Precipitation Estimates from Satellite Observations and Numerical Models. *Bulletin of American Society* 88 (1): 47-64.

EUMETSAT 1996. *Meteosat Transition Programme – Meteorological Products Extraction Facility (MPEF)*. Algorithms Specification Document, Appendix A, Detailed Algorithm Descriptions, Doc. No. MTP.SPE.030, Issue 2.0.

EUMETSAT 2000. The Meteosat System, EUM TD 05.

EUMETSAT 2003. *Meteosat Transition Programme – Rapid Scanning Service*, Technical Description, EUM TD 13.

EUMETSAT 2006a. *MSG Ground Segment LRIT/HRIT Mission - Specific Implementation.* Doc. No. EUM/MSG/SPE//057, Issue 6.

EUMETSAT 2006b. *Pre-Launch MSG-1 SEVIRI Instrument Level 1.0 Data*. Doc. No. EUM/OPS-MSG/TEN/05/0625, Issue v1.

Grassotti, C., Iskenderian, H. & Hoffmann, R.N. 1999. Fusion of Surface Radar and Satellite Rainfall Data using Feature Calibration and Alignment. *Journal of Applied Meteorology* 38: 677-694.

Grose, A.M.E., Smith, E.A., Chung, H.-S., Ou, M.-L., Sohn, B.-J. & Turk, F.J. 2002. Possibilities and limitations for quantitative precipitation forecasts using nowcasting methods with infrared geosynchronous satellite imagery. *American Meteorological Society* 41: 763-784.

Kurino, T. 1997a: A Rainfall Estimation with the GMS-5 Infrared Split-Window and Water Vapour Measurements. *Meteorological Satellite Centre*, Technical Note No. 33: 91-101.

Kurino, T. 1997b. A Satellite Infrared Technique for Estimating „Deep/Shallow" Convective and Stratiform Precipitation. *Adv. Space Res.* 19: 511-514.

Lakshmanan, V., Fritz, A., Smith, T., Hondl, K. & Stumpf, G. 2006. An Automated Technique to Quality Control Radar Reflectivity Data. *Journal of Applied Meteorology* 46: 288-305.

Lang, S. Tao, W.-K., Simpson, J. & Ferrier, B. 2003. Modelling of Convective-Stratiform Precipitation Processes: Sensitivity to Partitioning Methods. *Journal of Applied Meteorology* 42: 505-527.

Levizzani, V., Amorati, R. & Meneguzzo, F. 2002. *A Review of Satellite-Based Rainfall Estimation Methods.* European Comission Project MUSIC Report (EVK1-CT-2000-00058).

Negri, A.J. & Adler, R.F. 1993. An Intercomparison of Three Satellite Infrared Rainfall Techniques over Japan and Sourrounding Waters. *Journal of Applied Meteorology* 32: 357-373.

Negri, A.J., Adler, R.F. & Wetzel, P.J. 1984. Rain Estimation from Satellites: An Examination of the Griffith-Woodley-Technique. *Journal of Climate and Applied Meteorology* 23: 102-116.

Petty, G.W. 1995. The Status of Satellite-Based Rainfall Estimation over Land. *Remote Sensing Environment* 51: 127-137.

Reudenbach, C. 2003. *Konvektive Sommerniederschläge in Mitteleuropa.* Bonner Geographische Abhandlungen, Heft 109, Asgard-Verlag Sankt Augustin.

Reudenbach, C. 2005. Personal note.

Schmetz, J., Pili, P., Tjemkes, S.A., Just, D., Kerkmann, J., Rota, S. & Ratier, A. 2002. An Introduction to Meteosat Second Generation (MSG). *American Meteorological Society*, Boston.

Scofield, R.A. & R.J. Kuligowski 2003. Status and Outlook of Operational Satellite Precipitation Algorithms for Extreme-Precipitation Events. *Weather and Forecasting* 18: 1037-1051.

Tonelli, F., Borga, M., Tollardo, M. & Pendesini, M. 2003. Radar rainfall estimation assessment for heavy rainfall events. *ACTIF 1st Workshop, Combination of data from remote sensing technologies for flood forecasting – New techniques for improving remote sensing measurements of rain.* Bologna, 24-25th November 2003.

Vicente, G.A., Scofield, R.A. & Menzel, W.P. 1998. The Operational GOES Infrared Estimation Technique. *Bull. Amer. Meteor.* 79 (9): 1883-1998.

Erklärung

Hiermit versichere ich, dass ich die vorliegende Arbeit ohne unzulässige Hilfe Dritter und ohne Benutzung anderer als der angegebenen Hilfsmittel angefertigt habe; die aus fremden Quellen direkt oder indirekt übernommenen Gedanken sind als solche kenntlich gemacht.

Bei der Auswahl und Auswertung des Materials sowie bei der Herstellung der Manuskripte habe ich Unterstützungsleistungen von folgenden Personen erhalten:

- Prof. Dr. Christian Bernhofer, TU Dresden, Professur für Meteorologie
- Dr. Johannes Franke, Sächsisches Landesamt für Umwelt, Landwirtschaft und Geologie
- Dr. Rico Kronenberg, TU Dresden, Professur für Meteorologie
- Dipl.-Hydrol. Nadine Jatho, Landestalsperrenverwaltung des Freistaates Sachsen
- Dr. Olaf Hellmuth, Leibniz-Institut für Troposphärenforschung e.V., Leipzig
- Dr. Valeri Goldberg, TU Dresden, Professur für Meteorologie
- Dipl.-Hydrol. Philipp Körner, TU Dresden, Professur für Meteorologie
- Dipl.-Hydrol. Dmitri Lisnjak, ehem. TU Dresden, Professur für Meteorologie
- Dipl.-Hydrol. Uwe Büttner, Sächsisches Landesamt für Umwelt, Landwirtschaft und Geologie

Weitere Personen waren an der geistigen Herstellung der vorliegenden Arbeit nicht beteiligt. Insbesondere habe ich nicht die Hilfe eines kommerziellen Promotionsberaters in Anspruch genommen. Dritte haben von mir weder unmittelbar noch mittelbar geldwerte Leistungen für Arbeiten erhalten, die im Zusammenhang mit dem Inhalt der vorgelegten Dissertation stehen.

Die Arbeit wurde bisher weder im Inland noch im Ausland in gleicher oder ähnlicher Form einer anderen Prüfungsbehörde vorgelegt und ist – sofern es sich nicht um eine kumulative Dissertation handelt – auch noch nicht veröffentlicht worden.

Ich versichere die Einhaltung der in § 10 Abs. 2 der Promotionsordnung der Fakultät Umweltwissenschaften der Technischen Universität Dresden genannten Bedingungen für kumulative Dissertationen.

Ich bestätige, dass ich die Promotionsordnung der Fakultät Umweltwissenschaften der Technischen Universität Dresden anerkenne.

Dresden, 20. Juli 2021

Christina Görner